Anchoring Cu(II)-based Low-Dimensional S=1/2 Spin Lattices onto Functionalized Graphene

A Thesis

Submitted in Partial Fulfillment of the Requirements

for the Degree of

Doctor of Philosophy

by

Kriti Gupta

ID: 20142012

INDIAN INSTITUTE OF SCIENCE EDUCATION AND RESEARCH, PUNE

2020

Dedicated to

My Parents

भारतीय विज्ञान शिक्षा एवं अनुसंधान संस्थान, पुणे
INDIAN INSTITUTE OF SCIENCE EDUCATION AND RESEARCH (IISER), PUNE
(An Autonomous Institution, Ministry of Human Resource Development, Govt. of India)

Dr. NIRMALYA BALLAV
Associate Professor (Chemistry)
E-mail: nballav@iiserpune.ac.in
Web: http://www.iiserpune.ac.in/~nballav/

Dr. Homi Bhabha Road, Pashan
Pune 411 008, INDIA
Tel: +91 20 2590 8215
Fax: +91 20 2586 5315

Date: 20-July-2020

CERTIFICATE

Certified that the work incorporated in the thesis entitled ***"Anchoring Cu(II)-based Low-Dimensional S=1/2 Spin Lattices onto Functionalized Graphene"*** submitted by ***Ms. Kriti Gupta*** was carried out by the candidate, under my supervision. The work presented here or any part of it has not been included in any other thesis submitted previously for the award of any degree or diploma from any other university or institution.

Dr. Nirmalya Ballav
(Research Supervisor)

भारतीय विज्ञान शिक्षा एवं अनुसंधान संस्थान, पुणे
INDIAN INSTITUTE OF SCIENCE EDUCATION AND RESEARCH (IISER), PUNE
(An Autonomous Institution, Ministry of Human Resource Development, Govt. of India)

Date: 20-July-2020

Declaration

I ***Ms. Kriti Gupta*** declare that, this written submission represents my ideas in my own words and where others' ideas have been included; I have adequately cited and referenced the original sources. I also declare that I have adhered to all principles of academic honesty and integrity and have not misrepresented or fabricated or falsified any idea/data/fact/source in my submission. I understand that violation of the above will be the cause for disciplinary action by the Institute and can also evoke penal action from the sources which have thus not been properly cited or from whom proper permission has not been taken when needed.

The work reported in this thesis is the original work done by me under the guidance of ***Dr. Nirmalya Ballav.***

Ms. Kriti Gupta
(ID: 20142012)

nballav@iiserpune.ac.in Tel: +91 (020) 2590 8215 www.iiserpune.ac.in

Acknowledgment

I would like to start by conveying my deepest gratitude to my academic supervisor Dr. Nirmalya Ballav for his guidance and encouragement in my PhD tenure and providing me the freedom of taking my projects in the directions which fostered my academic understanding. I believe my PhD was a learning process where I have not only gained the scientific knowledge but also practiced to recognize and communicate a scientific storyline, supervised by Sir, it came with an unexpected level of independence as a PhD student. I joined in the group as fifth PhD student at a time when my seniors were yet to cultivate the finest fruits from there immense hard work and visualizing the process from a relatively new lab was all the motivation required and formed the basis of my efforts afterward. I acknowledge Indian Institute of Science Education and Research (IISER), Pune and its former and present directors Prof. K. N. Ganesh and Prof. J. B. Udgaonkar for providing an excellent research environment.

I am grateful to my Research Advisory Committee (RAC) members, Prof. V. G. Anand (IISER Pune) and Prof. Avinash S. Kumbhar (SPPU, Pune) for their time and invaluable suggestions during the annual RAC meetings that helped improving my work. I would like to thank Dr. Pattayil A. Joy (NCL, Pune) and his student Dr. Arun Dadwal for an extraordinary collaboration and providing all the dc magnetic susceptibility data which constitutes the primary part of my thesis. I am thankful to Dr. Surjeet Singh (IISER Pune) for opening up the facility of highly occupied PPMS in his lab for carrying out some critical measurements. I would thank Dr. Anil Jain (BARC, Mumbai) for ac susceptibility measurements in some sections of the thesis. I acknowledge the support from Dr. Anil K. Debnath (BARC, Mumbai) in the form of XPS measurements and Dr. Purushottam Jha in the form of Raman measurements in specific sections. I would extend my thanks to former and present Chair Chemistry Prof. M. Jayakannan and Prof. H. N. Gopi and all the faculty members of IISER Pune.

I thank Mr. Mayuresh Kulkarni, Mr. Prabhakar Anagare, Mr. Tushar Kurulkar, Mr. Mahesh Jadhav, Mr. Anil Prathamshetti, Mr. Yathish, Mr. Sudhir, Mr. Nilesh Dumbre, Mrs. Megha Paygude, Mr. Parveen Nasa, Mr. Ganesh Dimber, Mr. Sandip Kanade, Mr. Sanjay Meena, Mr. Prabhas for technical and administrative support. I am thankful to Dr. Umeshareddy Kacherki and Ms. Anuradha for library support and Mr. Sachin Behra, and Mr. Shailesh Patil for IT support.

I am very grateful to my amazing bunch of seniors and current alumni of "Interfacial Materials Chemistry" team, namely, Dr. Ranguwar Rajendra, Dr. Barun Dhara, Dr. Plawan K. Jha, and Dr. Shammi Rana. They have inspired me a lot right from the start of my PhD and it continues even today, I acknowledge their combined efforts for teaching me not only to operate instruments but also how to conduct quality research and how to handle numerous situations to continue PhD without any unnecessary stress. I enjoyed working with other alumni as well (Vikash, Anupam, Ashwini, Dr. Syed, Sakshi, Aswani, Jai, to name a few) and the current members of IMC team (Debashree, Pranay, Sujit, Pooja, Nahid, Umashis, Vijay, Ishan, Gopi, Manish, Shreeganesh, Atharva, to name a few), specially mentioning Pranay, Debashree, and Vikash, there were numerous ups and downs in this journey but these people made it worthy. A shout-out to Dr. Plawan and Dr. Shammi to help me kick start the ride of my PhD.

This acknowledgement will be incomplete without mentioning my school teachers Poonam ma'am and Jyoti ma'am (for keeping my interest up in science, particularly chemistry); my graduation teacher Shilpa ma'am for always being the inspiration to pursue PhD and motivation in difficult academic times.

I take the opportunity to thank ma'am (Dr. Tanushree Bhattacharjee) and Tani for their encouragement and moral support.

I am thankful to my other colleagues cum friends at IISER, Manna Da, Soumya Da, Aamod bhaiya, Shivani Di, Sumanta, and more… they play an important role in setting up my research attitude. I thank my friends, Girish, Om, Prashant, Deepak (X2), Arunabha, Dipti, Mayur, Shalini, Saurabh, Kingshuk, Ankita, and Punita, for making life at the campus interesting. I am thankful to another bunch (Shikha, Nilam, Akanksha, and Priyanka), they were always there to pat my back, through all the tough times, success and failures.

Now, I want to thank the people who were always there by my side and available irrespective of the circumstances, however unfortunately they were distanced far from me. My parents, sister (Shubhi), brother-in-law (Kapil), Aksh and Kiaan. Their unconditional and unmeasurable love, support and trust has encouraged me a lot to work harder with every passing day, without their support I would have not been able to accomplish whatever steps I have taken towards my personal and academic betterment.

I would also like to thank American Chemical Society (ACS), Elsevier, and John Wiley & Sons (Wiley-VCH) for publishing a number of my research articles produced during my PhD tenure at IISER Pune.

I am thankful to IISER Pune, DST-Nano Mission, and DST-SERB for the financial support.

Kriti Gupta

Table of Contents

A. Publications Included to Thesis

1. Embedding S = 1/2 Kagome-Like Lattice in Reduced Graphene Oxide

   K. Gupta, P. K. Jha, A. Dadwal, A. K. Debnath, I. Jaiswal, S. Rana, P. A. Joy, N. Ballav

   J. Phys. Chem. Lett. **2019**, *10*, 2663

2. Exploring Magnetic *XY* Behavior in a Quasi-2D Anisotropic Triangular Lattice of Cu(II) by Functionalized Graphene

   K. Gupta, A. Dadwal, P. Jha, A. Jain, S. M. Yusuf, P. A. Joy, N. Ballav

   Inorg. Chem. **2020**, *59*, 6214

3. Integrating Structurally Perfect S=1/2 Kagome-Lattice with Reduced Graphene Oxide

   K. Gupta, A. Dadwal, P. Ninawe, P. A. Joy, N. Ballav

   J. Phys. Chem. C **2020**, *124*, 19753

4. S=1/2 Kagome Antiferromagnet Barlowite: Facile Synthesis and Anchoring onto Graphene

   K. Gupta, A. Dadwal, A. Jain, P. Ninawe, S. M. Yusuf, P. A. Joy, N. Ballav

   Manuscript submitted 2020

B. Other Publications

1. Imparting Multifunctionality by Utilizing Biporosity in a Zirconium-based Metal-Organic Framework

   A. Jadhav,[#] **K. Gupta**,[#] P. Ninawe, N. Ballav ([#]Equal contribution)

   Angew. Chem. Int. Ed. **2020**, *59*, 2215

2. Magnetism in Bimetallic Ni^{II} -Co^{II} Coordination Polymer

   K. Gupta, A. Dadwal, P. A. Joy, N. Ballav

   AIP Conference Proceedings **2020**, *2265*, 030585

3. In Situ Generated Mn_3O_4-Reduced Graphene Oxide Nanocomposite for Oxygen Reduction Reaction and Isolated Reduced Graphene Oxide for Supercapacitor Applications

   P. K. Jha, V. Kashyap, **K. Gupta**, V. Kumar, A. K. Debnath, D. Roy, S. Rana, S. Kurungot, N. Ballav

   Carbon **2019**, *154*, 285

4. 3D Mesoporous Reduced Graphene Oxide with Remarkable Supercapacitive Performance

   P. K. Jha, **K. Gupta**, A. K. Debnath, S. Rana, R. K. Sharma, N. Ballav

   Carbon **2019**, *148*, 354

5. Metamagnetism in Nanosheets of Co^{II} -MOF with T_N at 26 K and a Giant Hysteretic Effect at 5 K

   K. Gupta, A. Dadwal, S. Rana, P. K. Jha, A. Jain, S. M. Yusuf, P. A. Joy, N. Ballav

   Inorg. Chem. **2018**, *57*, 15044

6. Giant Enhancement of Carrier Mobility in Bimetallic Coordination Polymers

   B. Dhara, V. Kumar, **K. Gupta**, P. K. Jha, and N. Ballav

   ACS Omega **2017**, *2*, 4488

7. Diamagnetic Molecules Exhibiting Room-Temperature Ferromagnetism in Supramolecular Aggregates

   B. Dhara, P. K. Jha, **K. Gupta**, V. K. Bind, and N. Ballav

   J. Phys. Chem. C **2017**, *121*, 12159

M	Magnetization
H	External magnetic field
M_S	Saturation magnetization
M_R	Remanent magnetization
H_C	Coercive field
χ	Magnetic susceptibility
C	Curie constant
T	Temperature (Kelvin)
θ or θ_{CW}	Weiss temperature
T_N	Néel transition temperature
f	Frustration factor
S=1/2	Spin = 1/2
FC	Field-cooled
ZFC	Zero-field-cooled
Oe	Oersted
μ_{eff}	Effective magnetic moment
μ_B	Bohr magneton
μSR	Muon Spin Resonance
T_{Cr}	Critical temperature
T	Tesla
C_p	Specific heat capacity
χ'_{ac}	Real part of ac magnetic susceptibility
J	Nearest-neighbor exchange interaction
J-T effect	Jahn-Teller effect
Bo	Botallackite
H	Herbertsmithite
P	Paratacamite
QSLs	Quantum Spin Liquids
GKA rules	Goodenough-Kanamori-Anderson rules
RVB	Resonating Valence Bond
BKT	Berezinskii–Kosterlitz–Thouless

1D	One Dimensional
2D	Two Dimensional
3D	Three Dimensional
GO	Graphene Oxide
rGO	Reduced Graphene Oxide
Gr	Graphite
MQ	Millipore Water
MeOH	Methanol
SQUID	Superconducting Quantum Interference Device
VSM	Vibrating Sample Magnetometer
XPS	X-ray Photoelectron spectroscopy
PPMS	Physical Property Measurement System
EDXS	Energy-Dispersive X-ray spectroscopy
UV-vis	Ultraviolet-Visible spectroscopy
FESEM	Field Emission Scanning Electron Microscopy
TEM	Transmission Electron Microscopy
HRTEM	High-Resolution Transmission Electron Microscopy
PXRD	Powder X-Ray diffraction
SAED	Selected Area Electron Diffraction
RT	Room Temperature
I-V	Current-Voltage
ac	Alternative current
dc	Direct current
Ω	Ohm
R	Resistance
ρ	Resistivity
σ	Conductivity
E_a	Activation energy
A	Ampere (current)
V	Voltage
S	Seebeck coefficient

P	Power factor
D	Defect band
G	Graphitic band
wt%	Weight percentage
g	Gram
mg	Milligram
mL	Millilitre
h	Hour
mmol	Millimole
°C	Degree Celsius
K	Kelvin
Å	Angstrom

Chapter 1

Introduction to Low-Dimensional Spin Lattices and Reduced Graphene Oxide

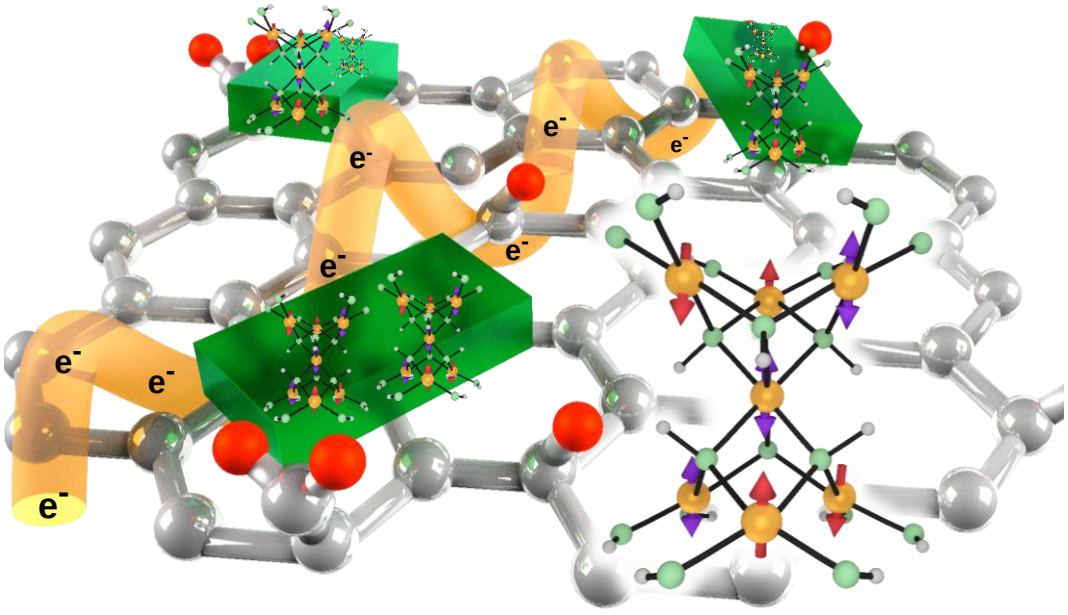

1.1 Introduction

This thesis presents information on chemical synthesis, characterization, and magnetic response of various frustrated S = 1/2 triangular spin lattices and further anchoring onto a functionalized graphene matrix, with Cu(II) as the only spin bearing species. The focus has majorly centered on exploring the corner shared triangular spin lattices, particularly S=1/2 kagome planes. In every chapter, the motivation is twofold: (1) facile synthesis of phase pure Cu(II)-based frustrated spin lattices at near ambient reaction conditions starting from a Cu(I) precursor, and (2) employing the oxidation process of Cu(I) to Cu(II) for in situ anchoring of the spin lattices onto functionalized graphene, generating a fundamentally new class of magnetic semiconductors, followed by the investigation of the effect of semiconducting and diamagnetic functionalized graphene onto the anchored spin lattices. Following is the outline of this chapter:

1.2 Spin Interactions and Spin Frustration

Figure 1.1 depicts the possible and majorly observed spin interactions in a system to attain long range magnetic order.[1, 2] These spin interactions form the basis of understanding various spin lattices and, in turn, spin frustration which suppresses any long range magnetic order.[3] The

characteristic M-H (magnetization versus external magnetic field) plots are shown in Figure 1.1.[1, 2] In ferromagnetic order, all the spins align themselves in the same direction approaching maximum magnetization possible in the system, also known as saturation magnetization (M_S). A ferromagnet stays in the magnetized state even when the externally applied field is removed (H = 0) giving a significant value for remanent magnetization ($M_R >> 0$) and an externally applied magnetic field in the opposite direction is required to bring the magnetization of the material back to zero i.e., coercive field (H_C). In the case of antiferromagnetic order, adjacent spins have antiparallel arrangement, as a result there is no net magnetization once the externally applied magnetic field is removed ($H_C = 0$). Adjacent antiparallel spins with unequal magnitudes of moment give rise to ferrimagnetic order exhibiting a significant non-zero value of remanent magnetization (M_R), similar to ferromagnetic ordering. Apart from these linear arrangements of spins, a non-collinear arrangement is also possible and known as canted antiferromagnet or weak ferromagnet where the spins are inclined at an angle (neither ferromagnetic nor antiferromagnetic arrangement). As a result, the value of magnetization keeps on increasing as a function of externally applied magnetic field and is not saturated even at highest applied magnetic field (Figure 1.1). This non-collinear arrangement of spins with competing nearest neighbor exchange interactions introduces frustration in the lattice.[4]

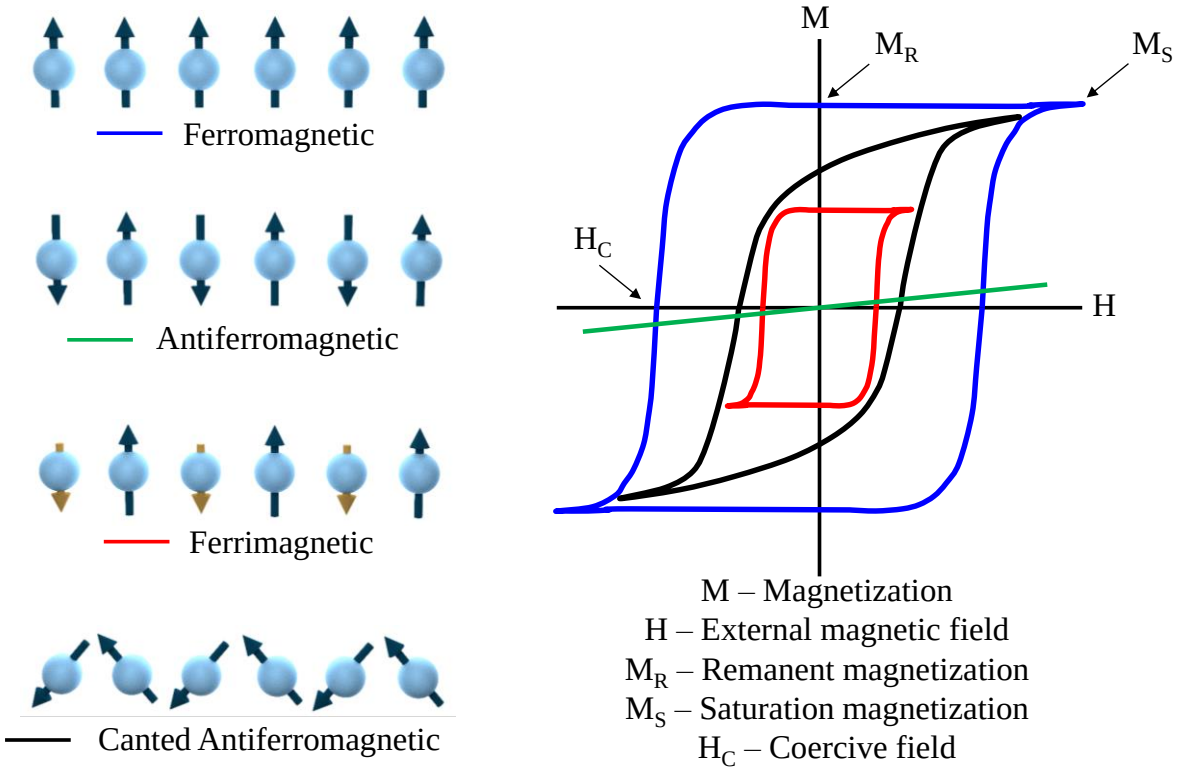

Figure 1.1. *Types of magnetic coupling (left panel), ferromagnetic, antiferromagnetic, ferrimagnetic, and canted antiferromagnetic along with their characteristic M-H curves (right panel).*

Let us understand the frustrated spin interactions with the help of a simple example of a cuprate which also happens to be one of the early experimental observation of relation between frustrated spins and superconductivity. The cuprate under study was La_2CuO_4 with a square Cu(II)-based spin lattice, and the addition of chemical dopants generated a high-T_C cuprate, $La_{2-x}(Ba,Sr)_xCuO_{4-y}$, which at sufficient doping levels and low temperatures, possess superconductivity.[5-7] Such a doping, resulted in the generation of local ferromagnetic coupling within Cu(II) ions, thus disrupting the three-dimensional (3D) antiferromagnetic coupling, as observed in undoped La_2CuO_4 (Figure 1.2a). Competitive interactions such as in doped La_2CuO_4 frustrates a particular spin in the system, and is typically realized by chemical doping or site disorder – known as a spin glass – with disordered arrangement of spins. Such frustrated spins suppress conventional long range magnetic ordering within the lattice and as a result, system dwells between numerous available degenerate ground states.

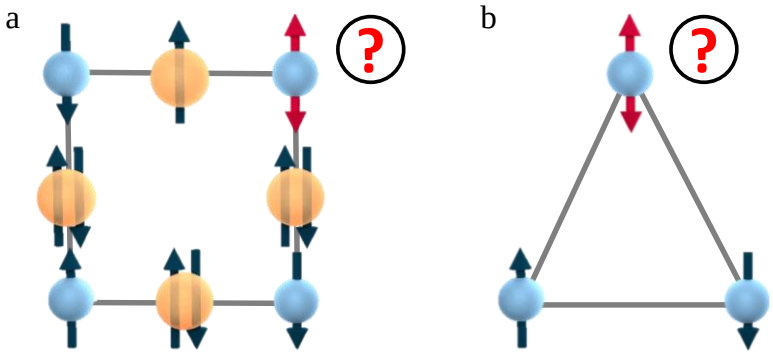

Figure 1.2. *(a) Spin glass behavior (doped spin lattice of La_2CuO_4), and (b) an equilateral triangular plaquette, exhibiting frustrated spins (red) due to competitive nearest neighbor spin interactions.*

Apart from spin glasses, with disordered spin arrangement causing frustration, there are geometrically frustrated magnets where, as the name suggests, the spin frustration stems solely from the geometry of the spin bearing species in the lattice. For instance, spins sitting on the vertex of an equilateral triangle in Figure 1.2b, and similarly, an odd number of spins in a formula or basic unit of the lattice can result in competitive spin interactions, where if two (or n-1) of the spins align anti-parallelly, then the third (or n^{th}) spin cannot align itself, rendering competing interactions within the lattice, leading to geometric spin frustration. The origin of spin frustration differs in the two classes, geometrically frustrated magnets and spin glasses,

and hence should not be confused as also described by Ramirez in his review (Figure 1.3).[4] In this thesis, work has been focused on geometrically frustrated spin lattices.

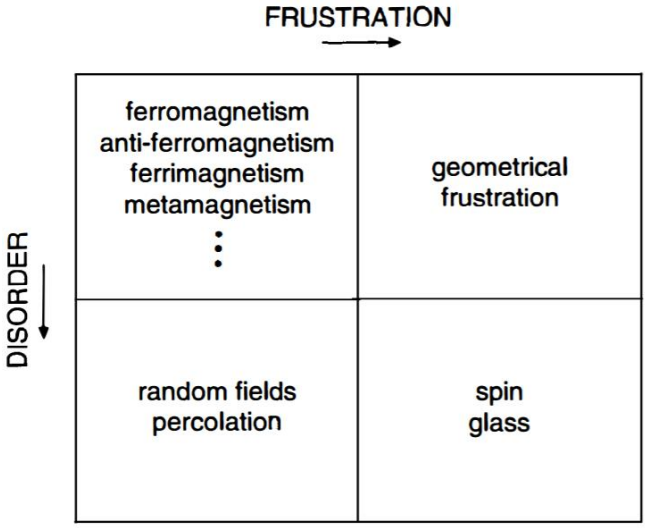

Figure 1.3. *Magnetic ground states with their related disorderness and frustration (adopted from ref. 4 © Annual Reviews).*

1.3 Frustrated Spin Lattices

One of the simplest systems to study spin frustration would be an equilateral triangular plaquette as shown in Figure 1.2b, which can be understood as zero-dimensional material or coordination complex. In such a scenario, it is expected that the single frustrated spin will be occupying all the three vertices of the triangular plaquette with equal probability, in fact, this is the case at high temperature, however, at lower temperatures, the triangular plaquette distorts relieving the spin frustration.[8-12] As an example, Ramsey and co-workers have observed that for a trinuclear Cu(II)-based complex, the unpaired spin density is localized onto a single Cu nucleus rather than equally distributed over three Cu nuclei and this has been ascribed to the Jahn-Teller distortion from an equilateral triangle to an isosceles triangle leading to the generation of two antiferromagnetically coupled spins and a single uncoupled spin instead of a frustrated spin in the ground state.[13] This demands for extended triangular lattices, and in a 2D system with triangular building block, two lattices can be generated, namely triangular lattice with edge-sharing triangles and kagome lattice with corner-sharing triangles (Figure 1.4). While in a 3D system, the building block will be a tetrahedron giving rise to two lattices from edge-sharing and corner-sharing tetrahedrons (pyrochlore lattice) (Figure 1.4). All the above mentioned four lattices, lacks Néel ordering with Ising spins, instead they possess numerous macroscopically degenerate states at low temperatures with *XY* or Heisenberg spins, where the

degree of frustration varies with the geometry and the nature of spins (Ising, XY or Heisenberg).[4]

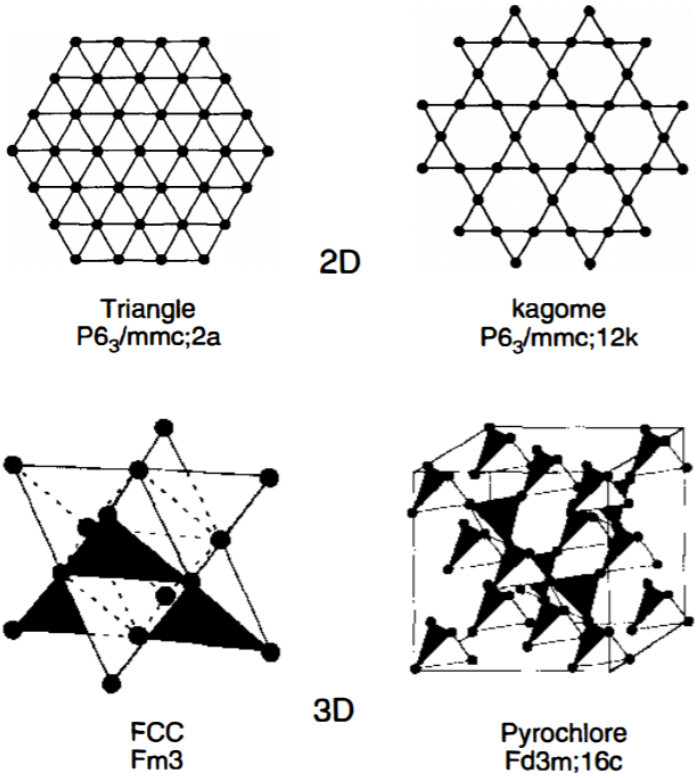

Figure 1.4. *Top: extended 2D frustrated spin lattices, edge-sharing triangular lattice and kagome lattice; Bottom: 3D frustrated spin lattices, edge-sharing and corner-sharing (pyrochlore lattice) tetrahedrons (note: dots represent the spin active centers) (adopted from ref. 4 © Annual Reviews).*

One of the probable ground states in a 3D system such as a pyrochlore lattice is 2-in 2-out configuration of spins with zero net moment in each tetrahedra (Figure 1.5a).[4, 14] While the ground state in a 2D frustrated spin lattice consists of spins with a non-collinear conformation where the nearest neighbor is angled at ±120° (Figure 1.5b).[4, 15] Such a configuration results in zero net moment satisfying antiferromagnetism in the lattice and is thus, one of the probable ground states (Figure 1.5b). Experimentally realizing 2D lattices is challenging and often results in quasi-2D lattices, thus various 3D materials possessing 2D spin lattice by incorporating diamagnetic species in between the planes have also been profoundly explored in order to study spin interactions in low dimensions. This thesis explores, (1) 3D pyrochlore spin lattice, (2) weakly coupled kagome spin lattice (quasi-2D spin system), (3) magnetically isolated 2D kagome spin lattice in a three-dimensionally structured framework, and (4) another 2D anisotropic triangular spin lattice.

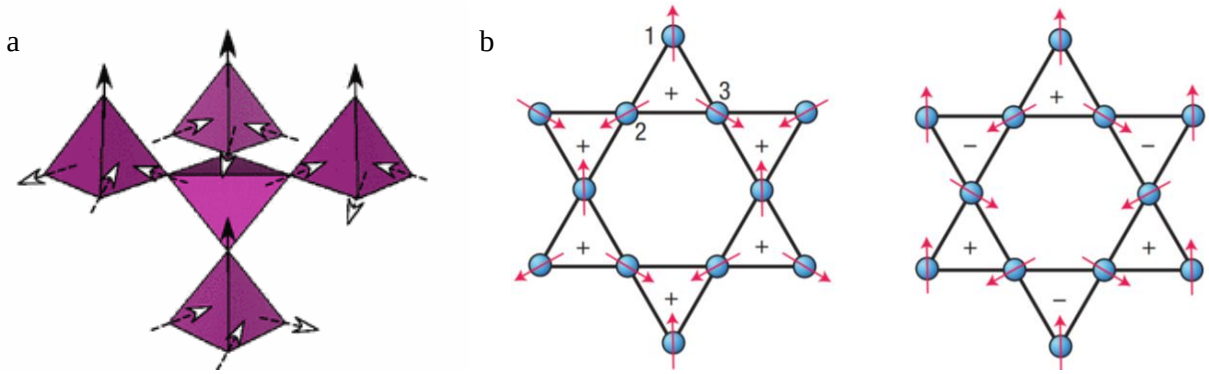

Figure 1.5. *(a) Possible ground states with non-collinear spin conformation in (a) pyrochlore lattice (adopted from ref. 14 © American Physical Society), and (b) kagome lattice (adopted from ref. 15 © Nature Publishing Group).*

1.4 Magnetic Semiconductors

Magnetic semiconductors are of both fundamental and practical interests with effectively combining the semiconducting and magnetic properties into a single material. They are sought after to display intriguing interplay between the magnetic and electronic behavior such as tuning the magnetic response by means of applied electric fields, current-induced domain displacement and more, leading to their various possible applications, for instance, spin injection, and tunnelling anisotropic magnetoresistance.[16] Table 1.1 lists the types of magnetic semiconductors:[17-24]

SN	Description	Reprersentative Example	Schematic
1	Inorganic/metal oxide-based system[17]	Transition metal [such as Co(II) or Mn(II)] doped ZnO	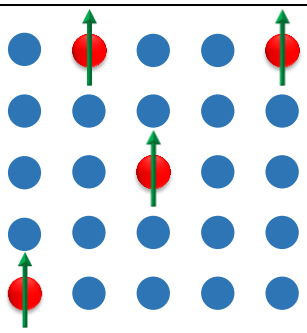

2	Nanoparticles/Nanocrystals-based system[18-19]	Transition metal [Co(II) or Ni(II)] doped In_2O_3 nanoparticles	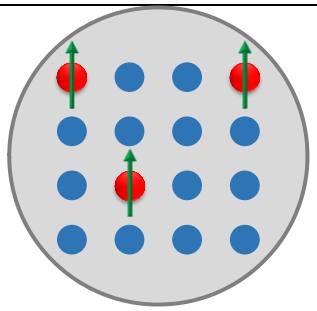
		Mn(II) doped inverted core–shell ZnSe–CdSe nanocrystals	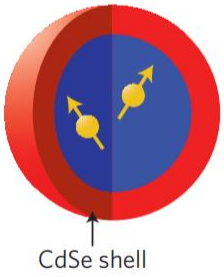 *(adopted from ref. 19 © Nature Publishing Group)*
3	Organic/molecule-based system[20-24]	$[BEDT\text{-}TTF]_3[MnCr(C_2O_4)_3]$; [BEDT-TTF - bis(ethylenedithio)tetrathiafulvalene]	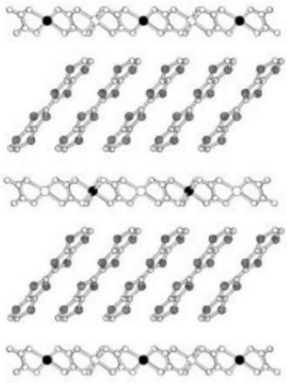 Alternating organic and inorganic layers *(adopted from ref. 20 © Nature Publishing Group)*
		Spin bearing metallo – phthalocyanines and their self-assembled ensembles; NiPc···ZnFPc and FePc···ZnFPc [NiPc - nickel(II) phthalocyanine,	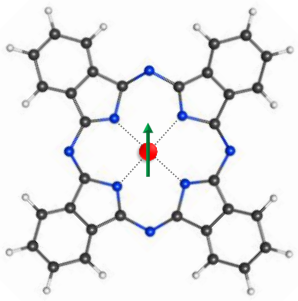

		ZnFPc - zinc(II) hexadecafluorophthalocyanine, FePc - iron(II) phthalocyanine]	
		$V[TCNE]_x$, [TCNE = tetracyanoethylene]; and quinoline complexes, $A^+[Ln(5,7Cl_2q)_4]^-$, Ln = Y^{3+}, Tb^{3+}, Dy^{3+}; $5,7Cl_2q$ = 5,7-dichloro-8-hydroxyquinoline; A^+ = Na^+, NEt_4^+, $K_{0.5}(NEt_4)_{0.5}^+$	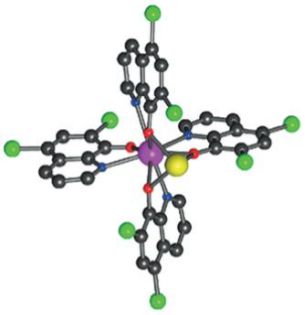 *(adopted from ref. 23 © Nature Publishing Group)*
4	Graphene and Cu(II) hydroxychlorides-based (this thesis)	Atacamite minerals anchored to rGO	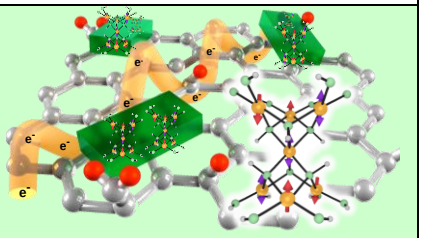

Table 1.1. *Types of magnetic semiconductors (note: this list is certainly not complete, only some representative examples are shown).*

One of the majorly explored class of magnetic semiconductors is dilute magnetic semiconductors (DMSs) where the magnetically active species is doped in a conventional semiconductor, however, DMSs suffer from the disadvantage of heterogeneous distribution of spins in the lattice and additionally, there is a limit to the doping level so as to maintain the electronic structure of the semiconducting host which often results in weaker ferromagnetism generated compared to a conventional ferromagnet.[25]

In this thesis, we have adopted a different methodology to bring semiconducting properties into various copper hydroxy halides, particularly from the atacamite family of minerals [$Cu_{4-x}M_x(OH)_6X_2$] where M=Zn, Cu, Co, Ni and X=Cl, Br, I].[26-28] These copper hydroxy halides can be categorized as Mott insulators with Cu(II) having d^9 configuration, i.e., materials which should be conducting according to the band theory but are electrical insulators due to strong electron – electron repulsion. To incorporate the semiconducting behavior, we conceptualized anchoring them onto graphene – one of the early reported and versatile low dimensional semiconductors.[29] In doing so, the overall moment of the material will not be affected much as

graphene is a low-weight material and the atacamite minerals are densely packed with magnetically active Cu(II) ions. To anchor spin lattices, graphene has to be functionalized to provide the sites for anchoring, however, functionalizing pristine graphene is often a complex process and as an alternative, we adopted the top down process for synthesis of graphene with minimal functional groups i.e., reduced graphene oxide (rGO). Further, the judicial choice of reagents allowed us to produce rGO as well as to in situ synthesize and anchor the spin lattices onto rGO sheets.

1.5 Functionalized Graphene – Reduced Graphene Oxide (rGO)

To chemically produce rGO, cheap and naturally abundant graphite (Gr) is initially exfoliated and oxidized to graphene oxide (GO) by following modified Hummer's method resulting in numerous oxygen containing functional groups onto the sheets (Figure 1.6).[30]

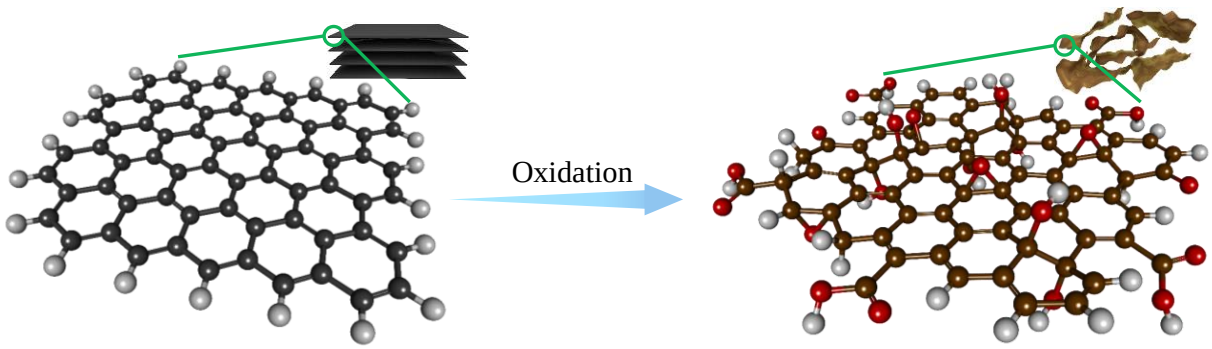

Figure 1.6. *Oxidation of graphite (Gr) to graphene oxide (GO) to functionalize and exfoliate the layers (insets: respective schematics to show the arrangement of layers; color code – black, brown – carbon, red – oxygen, white – hydrogen).*

Graphene oxide (GO) thus generated is a common precursor in all the chapters of this thesis where Cu(I) salt is added as the mild reducing agent for GO,[31,32] resulting in the formation of rGO with simultaneous oxidation of Cu(I) to Cu(II) ions in the reaction mixture (Figure 1.7). Cu(II) ions, thus generated in the course of reaction interacts with the residual functional groups present on rGO sheets and get stabilized in the form of atacamite minerals (Figure 1.7). By modulating the reactions conditions in the reduction step of GO to rGO, we were able to in situ stabilize five distinct Cu(II)-based spin lattices.

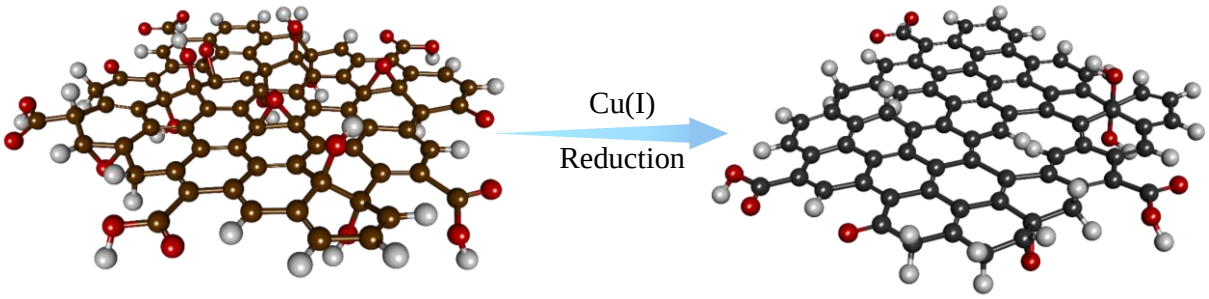

Figure 1.7. *Reduction of graphene oxide (GO) to reduced graphene oxide (rGO) by using Cu(I) as a mild reducing agent. (note: single sheets are shown to emphasize on the reduction in functionalities; color code: brown, black – carbon, red – oxygen, white – hydrogen).*

1.6 Magnetic Properties of Frustrated Spin Lattices – Experiments and Calculations

The magnetic susceptibility ($\chi = M/H$) of a sample can serve the purpose of a parameter to study the magnetic response of a material where inflection at any point recorded as a function of temperature indicates the transition to a magnetically ordered state.[1, 2] Magnetic susceptibility can be understood from Curie-Weiss law:

$$\chi = \frac{C}{T - \theta}$$

where χ is magnetic susceptibility, C is Curie constant, T is temperature in Kelvin, and θ is Weiss temperature in Kelvin. The values of Curie constant and Weiss temperature can be calculated by fitting the inverse susceptibility plots. The sign of θ reveals the average nearest neighbor interactions, where positive θ indicates parallel arrangement while negative θ indicates the antiparallel arrangement of spins within the lattice, and $|\theta|$ indicates the mean strength of magnetic coupling between two adjacent spins. For a conventional antiferromagnet, the Néel transition temperature (T_N) equals $|\theta|$ ($T_N \approx |\theta|$) while in a frustrated spin system, the observed T_N is significantly lower than $|\theta|$ ($T_N << |\theta|$), ascribed to the numerous degenerate ground states available for the system even at temperatures close to $|\theta|$, in turn suppressing the long range magnetic ordering. Frustration factor, f

$$f = \frac{|\theta|}{T_C}$$

where T_C is the transition temperature to a magnetically ordered state, serves as the marker for the level of spin frustration present in a given system where values of $f >> 10$ indicates very

high spin frustration, $1 < f < 10$ – moderate spin frustration and $f < 1$ indicates low spin frustration.[4,33]

1.7 Outline and Scope of Thesis

This thesis entitled "**Anchoring Cu(II)-based Low-Dimensional S=1/2 Spin Lattices onto Functionalized Graphene**" primarily concerns the synthesis, magnetic response, and electrical transport of S=1/2 spin lattices anchored onto diamagnetic and semiconducting reduced graphene oxide (rGO) sheets. Herein, we have explored a rather unconventional precursor, Cu(I) metal salts, to synthesis phase pure Cu(II)-based spin lattices at near-ambient conditions. Additionally, graphene oxide (GO) was taken along with other reactants and the oxidation of Cu(I) to Cu(II) was accompanied by the reduction of GO to rGO which not only led to the anchoring of Cu(II)-based spin lattices onto rGO but also the magnetic exchange interactions were notably modulated by the magnetically silent rGO matrix. Overall, five S=1/2 spin lattices are explored in this thesis, all belonging to the atacamite family of minerals and are known to be antiferromagnetic insulators. We have majorly covered Cu(II)-based kagome planes, strongly coupled in chapter-2 (clinoatacamite), weakly coupled in chapter-3 (barlowite), weakly coupled and magnetically isolated in chapter-4 (paratacamite and herbertsmithite), followed by another two-dimensional (2D) anisotropic triangular lattice in chapter-5 (botallackite). In one of the cases, successful electron doping of the spin lattice is proposed while in another, the crystallites of atacamite have grown with a preferred orientation onto rGO resulting in the observance of *XY* spin anisotropy, otherwise observed only in single crystals. In all the cases, the resultant nanocomposite is found to be a magnetic semiconductor.

Further experimentation with a combination of electrical and magnetic fields is highly desirable on such materials which may give better insights into the local spin interactions and we anticipate such nanocomposites to be serving demands of magnetic semiconductors particularly in the field of spintronics.[2,34]

This thesis further contains following chapters,

Chapter-2 (Clinoatacamite – S=1/2 Kagome-like Lattice onto Reduced Graphene Oxide)

In this chapter, clinoatacamite, a naturally occurring S = 1/2 kagome-like antiferromagnetic insulator,[35] is synthesized in water at ambient pressure for the first time from a cuprous chloride (CuCl) precursor whereby Cu(I) was spontaneously oxidized to Cu(II) in the form of clinoatacamite [$Cu_2(OH)_3Cl$] with a simultaneous reduction of graphene oxide (GO) to reduced

graphene oxide (rGO) in one pot. A stable nanocomposite of phase-pure clinoatacamite nanocrystals embedded in the rGO matrix was isolated. The clinoatacamite−rGO nanocomposite was determined to be magnetically active with a markedly enhanced coercive field of ~2500 Oe at 5 K as well as electronically active with a conductivity value of ~200 $S \cdot m^{-1}$ at 300 K. Our results illustrate an avenue of combining exotic magnetic and electronic lattices without impeding their individual characteristics and synergistically generating a new class of magnetic semiconductors.[36]

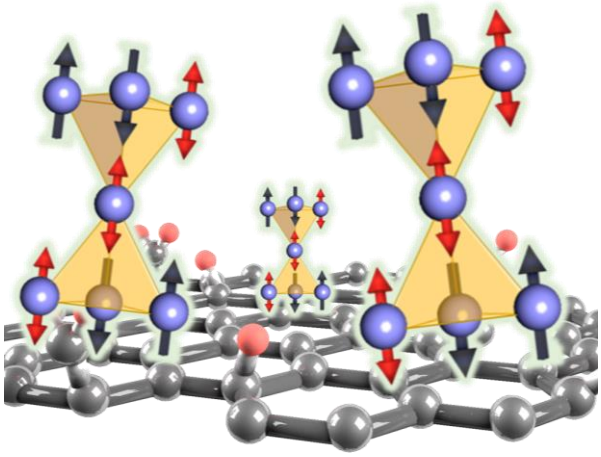

Publication from this chapter:

Embedding S = 1/2 Kagome-Like Lattice in Reduced Graphene Oxide

K. Gupta, P. K. Jha, A. Dadwal, A. K. Debnath, I. Jaiswal, S. Rana, P. A. Joy, N. Ballav

J. Phys. Chem. Lett. **2019**, *10*, 2663 *(Adopted from ref. 36 © American Chemical Society)*

Chapter-3 (Barlowite – S=1/2 Antiferromagnet Possessing Kagome Planes onto Reduced Graphene Oxide)

In this chapter, we have focused on barlowite $[Cu_4(OH)_6FBr]$,[37] another mineral from the atacamite family, exhibiting geometrically perfect S=1/2 kagome motif.[38] Likewise clinoatacamite in chapter 2, the kagome planes in barlowite are connected via Cu(II) ions at the interlayer site, however, the stacking of kagome planes is different from that in clinoatacamite resulting in weaker coupling of kagome planes and easy decoupling in the Zn doped variant of barlowite. Here, we present successful anchoring of phase-pure crystallites of barlowite onto reduced graphene oxide (rGO) starting from Cu(I) precursor. The barlowite-

rGO system was found to be an electrical semiconductor with a conductivity value of ~85 $S \cdot m^{-1}$ at 300 K while barlowite is an electrical insulator. We have attributed such a transformation of electrical transport response to plausible electron doping thereby making charge doping experiments on barlowite propitious for metallicity or high-temperature superconductivity.

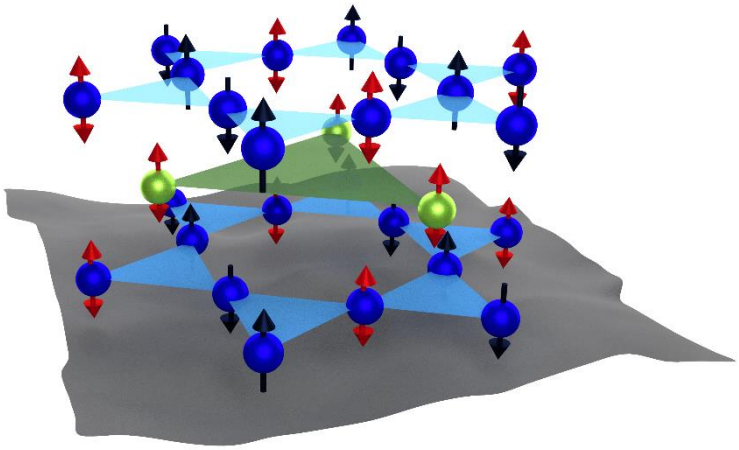

Publication from this chapter:

S=1/2 Kagome Antiferromagnet Barlowite: Facile Synthesis and Anchoring onto Graphene

K. Gupta, A. Dadwal, A. Jain, P. Ninawe, S. M. Yusuf, P. A. Joy, N. Ballav

Manuscript submitted 2020

Chapter-4 (Paratacamite – 2D S=1/2 Spin Kagome Lattice onto Reduced Graphene Oxide)

In this chapter, we have synthesized herbertsmithite (H) $[Cu_3Zn(OH)_6Cl_2]$[39] possessing structurally perfect S=1/2 kagome spin lattice as well as its structural analogue paratacamite (P) $[Zn_xCu_{4-x}(OH)_6Cl_2;\ 0.33 \leq x < 1]$,[40] at ambient reaction conditions. Herbertsmithite can also be understood as Zn-doped clinoatacamite where Zn is situated at the interlayer sites, thereby, resulting in 2D Cu(II)-based S=1/2 kagome spin lattice, while paratacamite possesses a combination of Zn(II) and Cu(II) at the interlayer sites. Taking graphene oxide (GO) as an additional reaction precursor, we could successfully integrate phase-pure crystallites of herbertsmithite and paratacamite with nanosheets of semiconducting and diamagnetic reduced graphene oxide (rGO) by in situ oxidation-reduction reaction. The isolated H-rGO and P-rGO systems were found to be magnetic semiconductors inheriting strong spin frustration from H

and P and semiconductivity from rGO. H-rGO system in particular exhibited negative Seebeck coefficient suggesting the n-type semiconducting nature. We anticipate the simple chemical principles outlined in this study to be useful for synthesizing a variety of complex QSLs and their electron doping which are otherwise inaccessible at ambient conditions.[42]

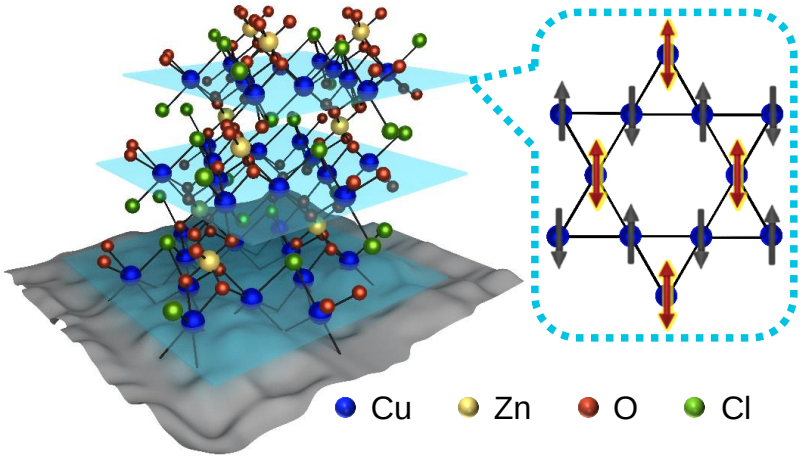

Publication from this chapter:

Integrating Structurally Perfect S=1/2 Kagome-Lattice with Reduced Graphene Oxide

K. Gupta, A. Dadwal, P. Ninawe, P. A. Joy, N. Ballav

J. Phys. Chem. C **2020**, *124*, 19753 *(Adopted from ref. 42 © American Chemical Society)*

Chapter-5 (Botallackite – 2D S=1/2 Anisotropic Triangular Lattice onto Reduced Graphene Oxide)

In this chapter, phase-pure botallackite (Bo) ($Cu_2(OH)_3Br$), a quasi-2D S=1/2 anisotropic triangular spin lattice[41] is stabilized over 2D reduced graphene oxide (rGO) nanosheets via simple oxidation−reduction reaction chemistry. In comparison to polycrystalline Bo, such an anchoring resulted in the oriented growth of Bo crystallites in the Bo-rGO system. The Bo-rGO nanocomposite was found to be magnetically active with a Néel transition at ~8.9 K, crossing over to possible *XY* anisotropy at ~5K – as revealed by complementary dc and ac susceptibility measurements – an unprecedented observation in the field assigned to an interfacial effect. This work demonstrates the potential usage of nonmagnetic 2D functionalized graphene to significantly modulate the magnetic properties of 2D spin lattices.[43]

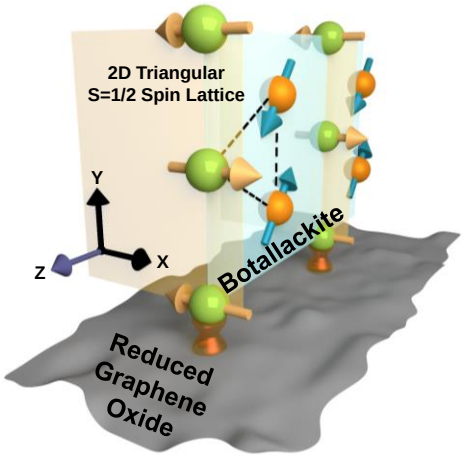

Publication from this chapter:

Exploring Magnetic *XY* Behavior in a Quasi-2D Anisotropic Triangular Lattice of Cu(II) by Functionalized Graphene

K. Gupta, A. Dadwal, P. Jha, A. Jain, S. M. Yusuf, P. A. Joy, N. Ballav

Inorg. Chem. **2020**, *59*, 6214 *(Adopted from ref. 43 © American Chemical Society)*

1.8 References

(1) Spaldin, N. Magnetic Materials, (Cambridge University Press, Cambridge, **2006**).

(2) M. Getzlaff, Fundamentals of Magnetism, (Springer, Berlin, **2008**).

(3) Lacroix, C.; Mendels, P.; Mila, F. Introduction to Frustrated Magnetism: Materials, Experiments, Theory, (Springer, Berlin, **2010**).

(4) Ramirez, A. P. Strongly Geometrically Frustrated Magnets. *Annu. Rev. Mater. Sci.* **1994**, *24*, 453-480.

(5) Bednorz, J. G.; Muller, K. A. Possible HighTc Superconductivity in the Ba−La−Cu−O System. *Z. Phys.***1986**, *B64*, 189-193.

(6) Tranquada, J. M.; Heald, S. M.; Moodenbaugh, A. R. X-Ray-Absorption Near-Edge-Structure Study of $La_{2-x}(Ba,Sr)_xCuO_{4-y}$ Superconductors. *Phys. Rev. B* **1987**, *36*, 5263.

(7) Aharony, A.; Birgeneau, R. J.; Coniglio, A.; Kastner, M. A.; Stanley, H. E. Magnetic Phase Diagram and Magnetic Pairing in Doped La_2CuO_4. *Phys. Rev. Lett.* **1988**, *60*, 1330.

(8) Butcher, R. J.; O'Connor, C. J.; Sinn, E. Synthesis and Relation between Magnetism and Structure of a Trinuclear Copper(II) Hydroxo Complex $[Cu_3OHL_3(ClO_4)]ClO_4$ and a Hexanuclear Copper(II) Oxo Complex $[Cu_3OL'_3(ClO_4)]_2$ (LH = 3- (Phenylimino)butanone 2-

Oxime, L'H = 1,2-Diphenyl-2-(methy1imino)ethanone 1-Oxime). *Inorg. Chem.* **1981**, *20*, 537-545.

(9) Liu, X.; de Miranda Marcelo, P.; McInnes Eric, J. L.; Kilner Colin, A.; Halcrow Malcolm, A. Antisymmetric Exchange in Two Tricopper(II) Complexes containing a $[Cu_3(\mu_3\text{-OMe})]^{5+}$ Core. *Dalton Trans.* **2004**, 59-64.

(10) Yoon, J.; Mirica, L. M.; Stack, T. D. P.; Solomon, E. I. Spectroscopic Demonstration of a Large Antisymmetric Exchange Contribution to the Spin-Frustrated Ground State of a D_3 Symmetric Hydroxy-Bridged Trinuclear Cu(II) Complex: Ground-to-Excited State Superexchange Pathways. *J. Am. Chem. Soc.* **2004**, *126*, 12586-12595.

(11) Stamatatos, T. C.; Vlahopoulou, J. C.; Sanakis, Y.; Raptopoulou, C. P.; Psycharis, V.; Boudalis, A. K.; Perlepes, S. P. Formation of the $\{Cu^{II}_3\ (\mu_3\text{-OH})\}^{5+}$ Core in Copper(II) Carboxylate Chemistry via Use of di-2-pyridyl Ketone Oxime $[(py)_2CNOH]$:$[Cu_3(OH)(O_2CR)_2\{(py)_2CNO\}_3]$ (R = Me, Ph). *Inorg. Chem. Commun.* **2006**, *9*, 814-818.

(12) Belinsky, M. I. Spin-Frustrated Trinuclear Cu(II) Clusters with Mixing of 2(S = 1/2) and S = 3/2 States by Antisymmetric Exchange. 2. Orbital Origin of In-Plane Dzialoshinsky–Moriya Exchange Parameters. *Inorg. Chem.* **2008**, *47*, 3521-3531.

(13) Cage, B.; Cotton, F. A.; Dalal, N. S.; Hillard, E. A.; Rakvin, B.; Ramsey, C. M. Observation of Symmetry Lowering and Electron Localization in the Doublet-States of a Spin-Frustrated Equilateral Triangular Lattice: $Cu_3(O_2Cl_6H_{23})\cdot 1.2C_6H_{12}$. *J. Am. Chem. Soc.* **2003**, *125*, 5270-5271.

(14) Zheng, X. G.; Kawae, T.; Yamada, H.; Nishiyama, K.; Xu. C. N. Coexisting Ferromagnetic Order and Disorder in a Uniform System of Hydroxyhalide $Co_2(OH)_3Cl$. *Phys. Rev. Lett.* **2006**, *97*, 247204.

(15) Grohol, D.; Matan, K.; Cho, J.-H.; Lee, S.-H.; Lynn, J. W.; Nocera, D. G.; Lee, Y. S. Spin Chirality on a Two-Dimensional Frustrated Lattice. *Nat. Mater.* **2005**, *4*, 323.

(16) Dietl, T. A Ten-Year Perspective on Dilute Magnetic Semiconductors and Oxides. *Nat. Mater.* **2010**, *9*, 965.

(17) Pearton, S. J.; Heo, W. H.; Ivill, M.; Norton, D. P.; Steiner, T. Dilute Magnetic Semiconducting Oxides. *Semicond. Sci. Technol.* **2004**, *19*, R59–R74.

(18) Ahmada, T.; Khatoonb, S.; Phul, R. A Review on Chemical Synthesis, Characterization and Optical Properties of Nanocrystalline Transition Metal Doped Dilute Magnetic Semiconductors. *Solid State Phenom.* **2013**, *201*, 103-129.

(19) Bussian, D. A.; Crooker, S. A.; Yin, M.; Brynda, M.; Efros, A. L.; Klimov, V. I. Tunable Magnetic Exchange Interactions in Manganese-doped Inverted Core-Shell ZnSeCdSe Nanocrystals. *Nat. Mater.* **2009**, *8*, 35–40.

(20) Coronado, E.; Galán-Mascarós, J. R.; Gómez-García, C. J.; Laukhin, V. Coexistence of Ferromagnetism and Metallic Conductivity in a Molecule-Based Layered Compound. *Nature* **2000**, *408*, 447–449.

(21) Dhara, B.; Jha, P. K.; Gupta, K., Bind, V. K.; Ballav, N. Diamagnetic Molecules Exhibiting Room-Temperature Ferromagnetism in Supramolecular Aggregates. *J. Phys. Chem. C* **2017**, *121*, 12159-12167.

(22) Dhara, B.; Tarafder, K.; Jha, P. K.; Panja, S. N.; Nair, S.; Oppeneer, P. M.; Ballav, N. Possible Room-Temperature Ferromagnetism in Self-Assembled Ensembles of Paramagnetic and Diamagnetic Molecular Semiconductors. *J. Phys. Chem. Lett.* **2016**, *7*, 4988–4995.

(23) Coronado, E. Molecular Magnetism: from Chemical Design to Spin Control in Molecules, Materials and Devices. *Nat. Rev. Mater.* **2020**, *5*, 87–104.

(24) Prigodin, V. N.; Raju, N. P.; Pokhodnya, K. I.; Miller, J. S.; Epstein, A. J. Spin-Driven Resistance in Organic-Based Magnetic Semiconductor V[TCNE]$_X$. *Adv. Mater.* **2002**, *14*, 1230-1233.

(25) Liu, W.; Zhang, H.; Shi, J.; Wang, Z.; Song, C.; Wang, X.; Lu, S.; Zhou, X.; Gu, L.; Louzguine-luzgin, D. V; Chen, M.W., Yao, K.F.; Chen, N. A Room-Temperature Magnetic Semiconductor from a Ferromagnetic Metallic Glass. *Nat. Commun.* **2016**, *7*, 13497.

(26) Chu, S.; Müller, P.; Nocera, D. G.; Lee, Y. S. Hydrothermal Growth of Single Crystals of the Quantum Magnets: Clinoatacamite, Paratacamite, and Herbertsmithite. *Appl. Phys. Lett.* **2011**, *98*, 092508−11.

(27) Liu, X.; Xu, L.; Huang, Y.; Cheng, H.; Seo, H. J. Paratacamite Phase Stability and Improved Optical Properties of $Cu_2(OH)_3Cl$ Crystal via Ni-Doping. *Mater. Des.* **2017**, *121*, 194−201.

(28) Li, Y.; Zhang, Q. Structure and Magnetism of S = 1/2 Kagome Antiferromagnets $NiCu_3(OH)_6Cl_2$ and $CoCu_3(OH)_6Cl_2$. *J. Phys.: Condens. Matter* **2013**, *25*, 026003.

(29) Novoselov, K. S.; Geim, A. K.; Morozov, S. V.; Jiang, D.; Zhang, Y.; Dubonos, S. V.; Grigorieva, I. V.; Firsov, A. A. Electric Field Effect in Atomically Thin Carbon Films. *Science* **2004**, *306*, 666-669.

(30) Jha, P. K.; Singh, S. K.; Kumar, V.; Rana, S.; Kurungot, S.; Ballav, N. High-Level Supercapacitive Performance of Chemically Reduced Graphene Oxide. *Chem* **2017**, *3*, 846-860.

(31) Zhao, Y.; Song, X.; Song, Q.; Yin, Z. A Facile route to the Synthesis Copper Oxide/Reduced Graphene Oxide Nanocomposites and Electrochemical Detection of Catechol Organic Pollutant. *CrystEngComm* **2012**, *14*, 6710-6719.

(32) Jha, P. K.; Gupta, K.; Debnath, A. K.; Rana, S.; Sharma, R. K.; Ballav, N. 3D Mesoporous Reduced Graphene Oxide with Remarkable Supercapacitive Performance. *Carbon* **2019**, *148*, 354-360.

(33) Shores, M. P.; Nytko, E. A.; Bartlett, B. M.; Nocera, D. G. A Structurally Perfect S = 1/2 Kagomé Antiferromagnet. *J. Am. Chem. Soc.* **2005**, *127*, 13462−13463.

(34) Wolf, S. A.; Awschalom, D. D.; Buhrman, R. A.; Daughton, J. M.; Von Molnar, S.; Roukes, M. L.; Chtchelkanova, A. Y.; Treger, D. M. Spintronics: A Spin-Based Electronics Vision for the Future. *Science* **2001**, *294*, 1488−1495.

(35) Zheng, X.; Kawae, T.; Kashitani, Y.; Li, C.; Tateiwa, N.; Takeda, K.; Yamada, H.; Xu, C.; Ren, Y. Unconventional Magnetic Transitions in the Mineral Clinoatacamite $Cu_2Cl(OH)_3$. *Phys. Rev. B: Condens. Matter Mater. Phys.* **2005**, *71*, 052409−13.

(36) Gupta, K.; Jha, P. K.; Dadwal, A.; Debnath, A. K.; Jaiswal, I.; Rana, S.; Joy, P. A.; Ballav, N. Embedding S= 1/2 Kagome-like Lattice in Reduced Graphene Oxide. *J. Phys. Chem. Lett.* **2019**, *10*, 2663-2668.

(37) Smaha, R. W.; He, W.; Jiang, J. M.; Wen, J.; Jiang, Y.-F.; Sheckelton, J. P.; Titus, C. J.; Wang, S. G.; Chen, Y.-S.; Teat, S. J. Materializing Rival Ground States in the Barlowite Family of Kagome Magnets: Quantum Spin Liquid, Spin Ordered, and Valence Bond Crystal States. *npj Quantum Mater*, **2020**, *5*, 1-11.

(38) Han, T.-H.; Singleton, J.; Schlueter, J. A. Barlowite: A Spin-1/2 Antiferromagnet with a Geometrically Perfect Kagome Motif. *Phys. Rev. Lett.* **2014**, *113*, 227203.

(39) Norman, M. Colloquium: Herbertsmithite and the Search for the Quantum Spin Liquid. *Rev. Mod. Phys.* **2016**, *88*, 041002.

(40) Braithwaite, R.; Mereiter, K.; Paar, W.; Clark, A. Herbertsmithite, $Cu_3Zn(OH)_6Cl_2$, a New Species, and the Definition of Paratacamite. *Mineral. Mag.* **2004**, *68*, 527−539.

(41) Zheng, X. G.; Yamashita, T.; Hagihala, M.; Fujihala, M.; Kawae, T. Magnetic Transitions in Botallackite-Structure $Cu_2(OH)_3Br$ and $Cu_2(OH)_3I$. *Phys. B* **2009**, *404*, 680.

(42) Gupta, K.; Dadwal, A.; Ninawe, P.; Joy, P. A.; Ballav, N. Integrating Structurally Perfect S = 1/2 Kagome-Lattice with Reduced Graphene Oxide. *J. Phys. Chem. C* **2020**, *124*, 19753.

(43) Gupta, K.; Dadwal, A.; Jha, P. K.; Jain, A.; Yusuf, S.; Joy, P. A.; Ballav, N. Exploring Magnetic *XY* Behavior in a Quasi-2D Anisotropic Triangular Lattice of Cu(II) by Functionalized Graphene. *Inorg. Chem.* **2020**, *59*, 6214.

Chapter 2

Clinoatacamite – S=1/2 Kagome-like Lattice onto Reduced Graphene Oxide

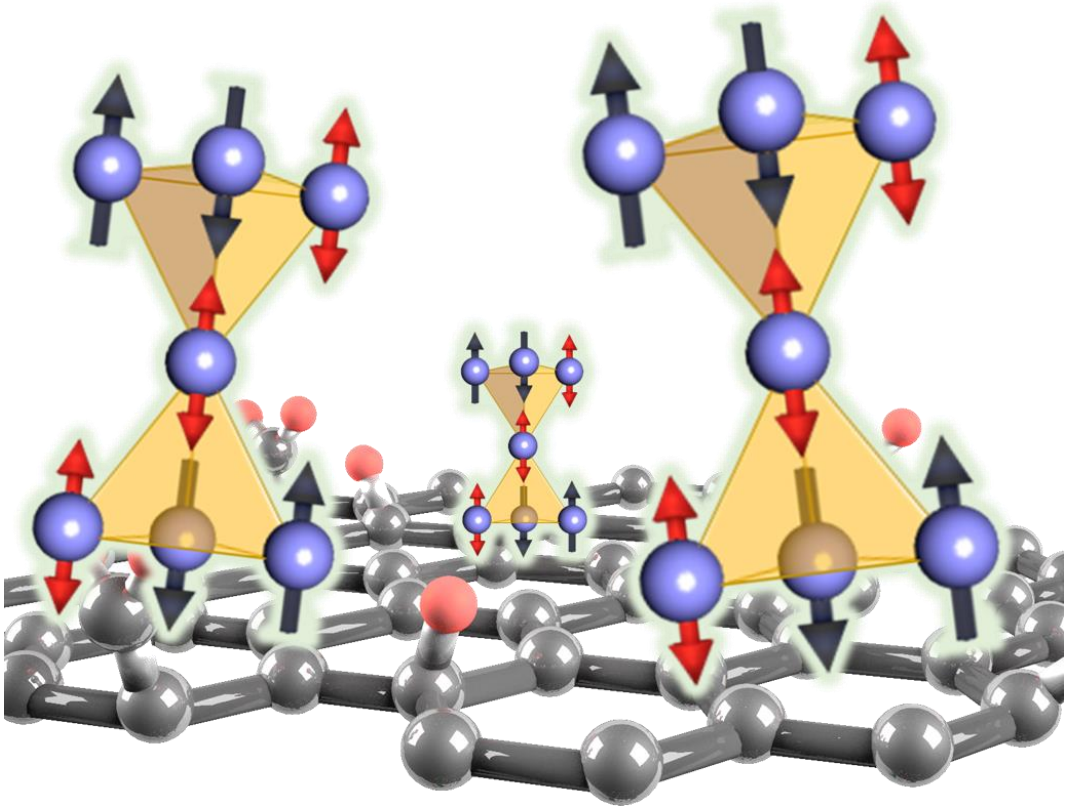

2.1 Introduction

Quantum mechanical fluctuations of electron spins (S=1/2) supressing solid-like ferromagnetic (↑↑) or antiferromagnetic (↑↓) ordering leading to a liquid-like state (↑↕) down to the lowest temperatures are termed quantum spin liquids (QSLs).[1-3] Localized spins in QSLs are frustrated due to competing exchange interactions (geometrical frustration) and giving rise to large degeneracy of the ground state that could have stimulating impact for the development of transformative quantum technologies.[4,5] A simple platform to study QSLs would be a two-dimensional triangular spin lattice with either edge-sharing or corner-sharing (kagome) lattice.[6] Although spins aligning at 120° in the former lattice can lead to the Néel ground state, sharing of the corners in the kagome lattice brings the ground state only with the noncollinearly aligned spins and thus leaves high degree of frustration.[7]

Various materials including natural minerals possessing S=1/2 kagome lattice have been explored as QSLs[2,8-9] and one of the well-known systems is the atacamite family of frustrated magnetic insulators [$Zn_xCu_{4-x}(OH)_6Cl_2$], where x=1 member (herbertsmithite) possesses a structurally perfect S=1/2 kagome lattice and x=0 member (clinoatacamite) comes with the added advantage of no site-specific disorder, an otherwise critical issue with the other members $1 \geq x > 0$ of the atacamite family.[10-12] Clinoatacamite is based on solely Cu(II) as the metal center in the intralayer kagome plane as well as at the interlayer site bridging the two kagome planes. It can be visualized to possess corner-sharing tetrahedrons with noncollinearly arranged apical spins of Cu(II) resembling an S=1/2 Heisenberg quantum pyrochlore lattice.[6,13,14] However, atacamite family members are poor conductors of electricity and are realized to be synthetically challenging (mostly solvothermal conditions involving Cu(II) salts)[15-18] which in turn restricts their potential for spintronic applications.

Herein, we report a straightforward strategy, oxidation-reduction in water involving cuprous chloride (CuCl) and graphene oxide (GO), whereby reduction of graphene oxide (GO) to reduced graphene oxide (rGO) with simultaneous oxidation of Cu(I) to Cu(II) stabilized in the form of clinoatacamite [$Cu_2(OH)_3Cl$] nanocrystals onto the surface of rGO yielded a stable nanocomposite exhibiting magnetic properties of pristine clinoatacamite as well as the semiconductivity of rGO. This study offers a unique opportunity to easily embed insulating QSLs, specifically the members of the atacamite family possessing S=1/2 kagome lattice, into a conducting rGO matrix and to investigate their exotic magnetic and electronic properties.

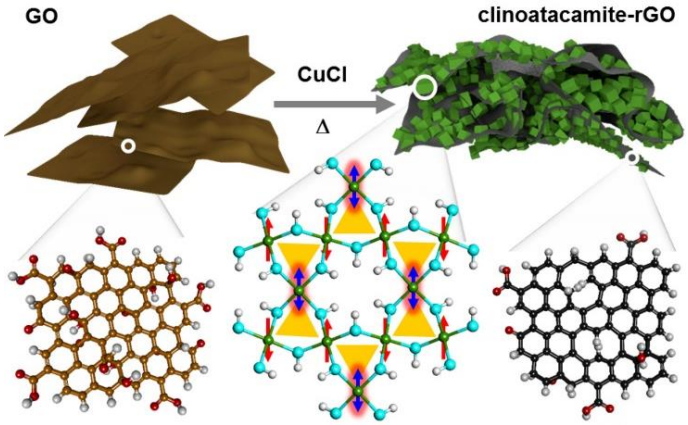

Figure 2.1. *Schematic elucidating the synthesis of clinoatacamite-rGO nanocomposite along with the structures of GO, rGO, and kagome plane in clinoatacamite (color code: brown and black, carbon; green, Cu(II); red and cyan, oxygen; white, hydrogen).*

2.2 Materials and Methods

Graphite flake (+100 mesh), potassium permanganate ($KMnO_4$), hydrogen peroxide (H_2O_2), and copper chloride (CuCl) were purchased from Sigma-Aldrich. Sulphuric acid (H_2SO_4) and methanol (MeOH) were purchased from RANKEM (India). Millipore water (MQ, ~18.2 MΩ·cm) was used whenever required.

The GO was synthesised and duly characterized following our previous report.[19] Further, GO was centrifuged at 500 rpm to remove the multilayers. In a 500 mL round bottomed flask, ~600 mg (~6 mmol) of CuCl was dispersed in 100 mL Millipore water, and 100 mL of GO (~1 mg/mL) was mixed, followed by stirring at 94 °C for ~24 h. A light green precipitate was filtered, washed with water and a small amount of methanol, and dried under vacuum for ~10 h at 150 °C (here assigned as clinoatacamite-rGO nanocomposite). Pristine clinoatacamite was synthesized by dispersing ~600 mg (~6 mmol) of CuCl in 200 mL of Millipore water followed by stirring at 94 °C for ~24 h, without using any external oxidizing agent; washing with water and methanol; and finally, drying under vacuum for ~10 h at 150 °C.

In order to realize the magnetic influence of rGO in the nanocomposite, rGO was extracted from the clinoatacamite-rGO nanocomposite, where composite was stirred in 0.5 M HCl solution at RT (300 K). The black colored material was filtered, washed, and vacuum-dried. After etching the clinoatacamite-rGO nanocomposite in acid, the amount of rGO was quantified to be around 10±3 wt% across five batches.

The magnetic responses of polycrystalline powder samples were recorded on a SQUID vibrating sample magnetometer (Quantum Design). Field-cooled (FC) magnetization was measured by cooling the sample in the applied magnetic field and recording the magnetization in the same field while warming. Zero-field-cooled (ZFC) magnetization was measured after cooling the sample in zero field and recording the magnetization in a field while warming. XPS measurements were carried out using Mg-K_α (1253.6 eV) source and DESA-150 electron analyzer (Staib Instruments, Germany). The binding-energy scale was calibrated to Au-$4f_{7/2}$ line of 84.0 eV. The analyzer was operated at 40 eV pass energy. Pressure in the chamber during analysis was ~ 5 x 10^{-9} Torr. Raman spectroscopy was done on powder samples using 632.8 nm laser (Horiba Jobin Yvon). PXRD patterns were recorded on a Bruker D8 Advance diffractometer with Cu Kα radiation (λ = 1.5406 Å) within the 2θ range of 15-80º. The PXRD pattern of clinoatacamite-rGO nanocomposite was simulated by the Powder Cell for Windows (PCW) software version 2.4 (reference: W. Kraus and G. Nolze), using the space group, lattice parameters and atomic positions from the literature.[18] FESEM images were taken under a Zeiss Ultra Plus scanning electron microscope after drop casting the samples (dispersed in methanol) on a silicon wafer. TEM images were recorded on drop casted sample (dispersed in methanol) over a 200 mesh Cu grid using JEM-2200FS transmission electron microscope. Heat capacity was recorded in a Quantum Design-PPMS-Evercool II instrument. Four-probe dc electrical conductivity (I-V) measurements were done on a PPMS as well as conventional Keithley 6221 setup.

2.3 Results and Discussion

In the first step, graphene oxide (GO) was prepared by the modified Hummer's method and duly characterized following our standardized protocol.[19] An aqueous solution of cuprous chloride (CuCl) was added to an aqueous dispersion of GO and stirred at 94 °C for ~24 h (see Materials and Methods for details). Oxidation of Cu(I) to Cu(II) and concomitant reduction of GO to rGO yielded a green colored solid, here named as clinoatacamite-rGO nanocomposite (Figure 2.1). In the family of atacamite, finger-print diffraction peaks at 2θ ≈ 32.5° and ~40° in the powder X-ray diffraction (PXRD) pattern confirmed the presence of clinoatacamite in the nanocomposite (Figure 2.2a).[16] A close similarity between the simulated[18] and our recorded PXRD patterns suggested phase-purity of clinoatacamite in the nanocomposite and also excluded the possibility of presence of other polymorphs, for example, paratacamite.[16,20] The

Fourier transform infrared (FTIR) spectrum of the composite confirmed the presence of phase-pure clinoatacamite by showing characteristic vibrational signatures in the spectral ranges of 750-1050 cm^{-1} and 3200-3500 cm^{-1} (Figure 2.2b).[15] Specifically, the peak at 3401 cm^{-1} which can serve as the fingerprint for detection of anatacamite was found to be absent in our clinoatacamite-rGO nanocomposite. The appearance of characteristic D (~1326 cm^{-1}) and G (1594 cm^{-1}) bands (from Raman) in clinoatacamite-rGO nanocomposite confirmed the presence of rGO in the material (Figure 2.2c).[19,21] X-ray photoelectron spectroscopy (XPS) was employed to probe the oxidation-reduction reaction in the conversions of GO to rGO as well as Cu(I) to Cu(II). The Cu2p XPS spectrum confirmed almost conclusive presence of Cu(II) revealing peaks at binding energy values of 933.4 eV ($Cu2p_{3/2}$) and 953.5 eV ($Cu2p_{1/2}$) along with the respective satellite features at 942.5 eV and 961.8 eV, as expected for clinoatacamite (Figure 2.2d and Appendix 2.1b).[22,23] The photoemission signal characteristic of Cu(I) species was almost absent (Figure 2.2d). The C 1s XPS spectrum of rGO was deconvoluted mainly into three peaks corresponding to –COOH, –C-O/–C-OH and –C=C– moieties at binding energy values of 288.4 eV, 286.4 eV and 284.7 eV, respectively (Appendix 2.1c). A comparative analysis of the XPS spectral intensity clearly suggested the conversion of GO to rGO (Appendix 2.1a, c).[19] Specifically, intensity values of the –COOH and –C-O/–C-OH peaks in rGO were significantly decreased and intensity value of the –C=C– peak increased – consistent with our recent claim of chemical reduction (Appendix 2.1).[19]

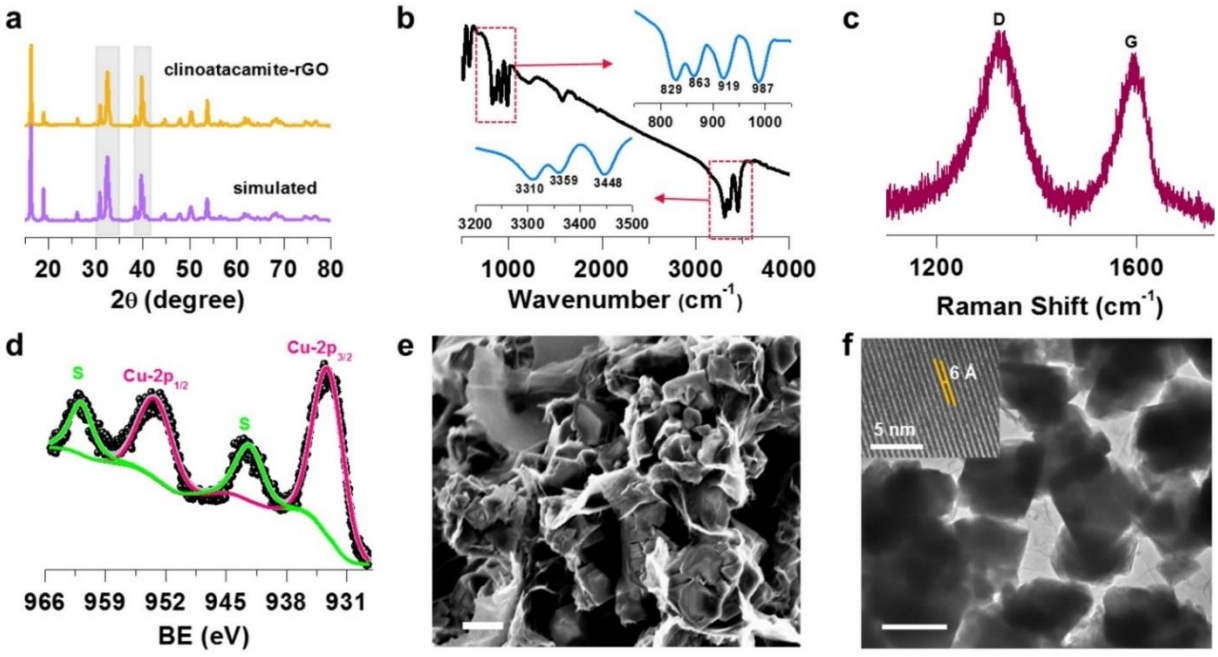

Figure 2.2. *(a) PXRD patterns of clinoatacamite (simulated) and clinoatacamite-rGO nanocomposite (experimental). (b) FTIR spectrum of clinoatacamite-rGO nanocomposite (insets: zoomed in spectra at the fingerprint regimes). (c) Raman spectrum of clinoatacamite-rGO nanocomposite revealing characteristic D and G bands of rGO. (d) Cu2p XPS spectrum of clinoatacamite-rGO nanocomposite. (e) FESEM image of clinoatacamite-rGO nanocomposite; scale bar, 500 nm. (f) HRTEM image of clinoatacamite-rGO nanocomposite (inset: zoomed-in view visualizing the fringes); scale bar, 500 nm.*

A closer look into the C1s XPS data showed the presence of –COOH (288.4 eV) and –C-O (286.4 eV) functional groups in rGO (after etching out clinoatacamite, see Appendix 2.1c) while both the functional groups were observed to be deprotonated $–COO^-$ (288.0 eV) and $–C-O^-$ (286.1 eV) in the nanocomposite (Appendix 2.1b).[24-25] Such an alternation in the binding energy values of C 1s photoemission clearly suggested that clinoatacamite embedded in the rGO matrix was indeed chemically bonded to the rGO sheets (Appendix 2.1). A strong red-shifted ($\Delta\nu$ = ~133 cm^{-1}) stretching frequency of the carboxy group in the FTIR spectra further supported transformation of –COOH to –COOCu in the clinoatacamite-rGO nanocomposite and complemented the XPS data (Appendix 2.2).[24,26,27] Perhaps, these oxygenated functional groups provided the nucleation sites for the growth of clinoatacamite nanocrystals. Field-emission scanning electron microscopy (FESEM) images showed the clinoatacamite nanocrystals wrapped with the rGO sheets (Figure 2.2e and Appendix 2.3a). High-resolution transmission electron microscopy (HRTEM) images revealed embedding of cuboid nanocrystals of clinoatacamite onto the rGO sheets (Figure 2.2f and Appendix 2.3b, c). Also, equally spaced fringes at 6 Å corresponded to the [011] plane ($2\theta \approx 16.4^{o}$) of pristine clinoatacamite (Figure 2.2f: inset)[28] thereby suggesting the single-crystalline nature of the material in the nanocomposite. Thorough energy-dispersive X-ray spectroscopy (EDXS) analysis revealed the Cu:Cl ratio to be ~2:1 which is present in clinoatacamite (Appendix 2.4). For a comparative assessment of the physical properties, pristine clinoatacamite was synthesized in a control experiment and duly characterized (Appendix 2.5).

To investigate magnetic behaviour of the clinoatacamite-rGO nanocomposite, dc magnetic susceptibility as a function of temperature was recorded in field-cooled (FC) and zero field-cooled (ZFC) modes at an applied field of 50 Oe (Figure 2.3a). The inverse magnetic susceptibility plot in the temperature range 150-300 K was fitted with the Curie-Weiss equation, $\chi=C/(T-\theta_{CW})$ and extracted values of Curie constant (C) and Curie-Weiss temperature (θ_{CW}) were found to be 1.10 $emu\cdot Oe^{-1}\cdot mol^{-1}\cdot K$ and -130.9 K, respectively (Appendix 2.6). A large negative value of θ_{CW} suggested strong nearest-neighbour antiferromagnetic interaction

to be operative in clinoatacamite. On the basis of the distance of Cu from Cl (2.7-2.8 Å) and from bridging oxo-ligand (1.9-2.3 Å), the magnetic exchange interactions could take place via bridging oxo-ligand offering shorter distance rather than Cl^- ligand (Appendix 2.7). The effective magnetic moment (μ_{eff}) per Cu ion was estimated to be ~2.09 μ_B (close to spin-only moment of ~1.73 μ_B) and justifying the dominance of Cu(II) with S=1/2 configuration in the system.

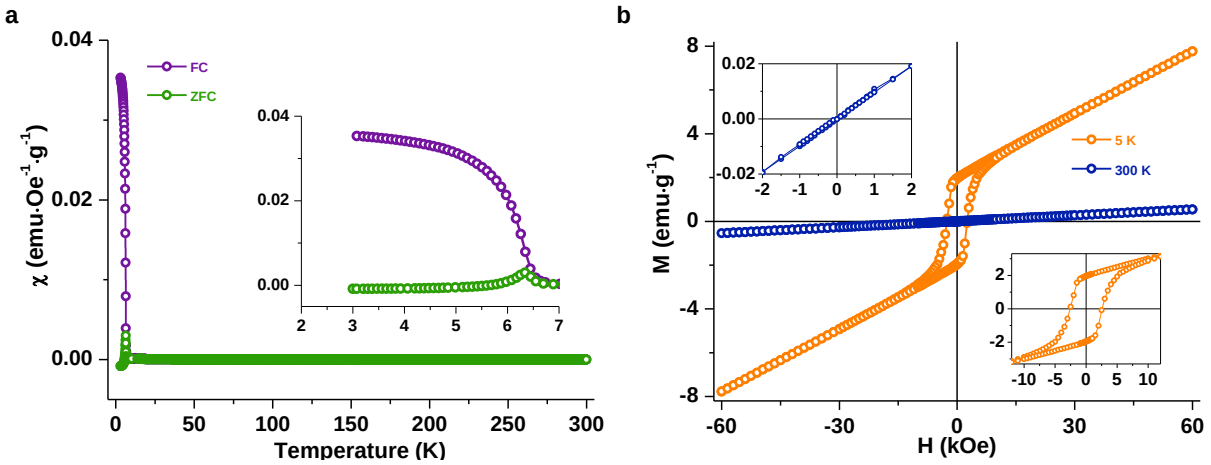

Figure 2.3. *(a) Magnetic susceptibility versus temperature plot (χ-T) of clinoatacamite-rGO nanocomposite recorded at an applied field of 50 Oe (inset: zoomed-in view to visualize the T_{Cr} at 6.4 K). (b) M-H plots of clinoatacamite-rGO nanocomposite at 300 K and 5 K (insets: zoomed-in view of M-H at 300 K and 5 K).*

The ZFC curve of the nanocomposite exhibited no magnetic transition until 6.4 K (critical temperature, T_{Cr}) where a sharp cusp was observed resembling ferromagnetic-like transition analogous to pristine clinoatacamite (Figure 2.3a).[6,7,18] Though strong antiferromagnetic interactions are predicted by the Curie-Weiss law, no Néel transition was observed in the magnetic susceptibility plot, and such an absence of the Néel transition could be ascribed to the high magnetic frustration present in the clinoatacamite-rGO nanocomposite. Using the equation, $f = |\theta_{CW}|/T_{Cr}$, the value of frustration factor, f, was estimated to be ~20.5 (f > 10 indicates high magnetic frustration), which clearly evidenced the presence of a magnetically frustrated kagome-lattice in the clinoatacamite-rGO nanocomposite.[12,29] The magnetic susceptibility in both FC and ZFC modes of rGO, extracted from the nanocomposite, consistently showed diamagnetic characteristics (Appendix 2.8) and notably, the extracted rGO did not show any traces of Cu species in the XPS data (Appendix 2.9). Thus, our magnetic

susceptibility data clearly reflect successful embedding of the clinoatacamite nanocrystals in rGO matrix without impeding the critical magnetic response.

Magnetization as a function of externally applied magnetic field (M-H) was recorded for the clinoatacamite-rGO nanocomposite, one at room-temperature (300 K) and the other at low-temperature (5 K) (Figure 2.3b). Appearance of a straight lined M-H curve at 300 K was typical of paramagnetic behaviour of the nanocomposite, and at 5 K, no saturation of magnetization was observed in the M-H curve even up to an applied field of 60 kOe, suggesting the presence of magnetically frustrated spin moments aligned non-collinearly.[7] Also, muon-spin experiments on clinoatacamite revealed a long-range magnetic order at 18.1 K followed by rapid spin fluctuation until 7 K; at further low temperatures, the coexistence of long-range magnetic order as well as spin fluctuation was observed.[7] Interestingly, for the nanocomposite, a prominent loop in the M-H plot was observed at 5 K with a large coercive field (H_C) of ~2500 Oe which is significantly higher than the value of pristine clinoatacamite (~1240 Oe at 5 K) prepared in this study (Appendix 2.10). In fact, our H_C value of pristine clinoatacamite matched well with an earlier reported value.[18] M−H plots of pure rGO at 300 and 5 K consistently revealed diamagnetic characteristics (Appendix 2.8b). One of the contributing factors for such higher values of H_C in our clinoatacamite−rGO nanocomposite could be enhanced magnetic interaction between the clinoatacamite nanocrystals via chemical bonding with the conducting rGO matrix. The particle size of the clinoatacamite−rGO nanocomposite could also potentially influence the value of H_C,[30–33] specifically keeping in mind that studies on the magnetism of kagome-like systems at the nanoscale are rare. However, our thorough FESEM analysis revealed a broad size distribution (500 nm to 2 μm) for both the materials, clinoatacamite−rGO nanocomposite and pristine clinoatacamite (Appendix 2.11), which suggests that the size effect is a minor contributor for the enhancement of the H_C value, though estimation of size by other complementary techniques would be desirable for such a claim. Notably, both micrometer-sized particles as well as fine powders (10−100 nm) of pristine clinoatacamite exhibited similar H_C values,[18] thereby supporting the role of rGO in enhancing the H_C value for our clinoatacamite−rGO nanocomposite.

In the nanometer ranges, usually the coercivity increases with increasing particle size, where each particle acts as a single domain.[31] However, after reaching a critical limit, the coercivity decreases with further increase in the size of the particle as the particle enters into the multidomain regime.[31] The average size of the clinoatacamite crystallites under study is

approximately 500 nm, which reflects the presence of rather multidomain grains (Appendix 2.11). Further, the crystallites are chemically bonded to rGO sheets (discussed above), which could potentially elevate the interparticle interaction (kind of dipolar) compared to that in pristine clinoatacamite.[30] The chemical bonding between the clinoatacamite and rGO can also induce spin arrangement anisotropy at the interface and/or lead to domain wall pinning;[34,35] thus, significant enhancement in the coercivity value of our clinoatacamite–rGO nanocomposite system (Appendix 2.10c) is ascribed to the combined effect of surface anisotropy and interparticle interactions.[30] A reduction in the remanent magnetization at 5 K in the clinoatacamite–rGO nanocomposite when compared to that of pristine clinoatacamite is also indicative of surface effects.[33]

Apart from the critical transition at ~6.4 K, clinoatacamite is known to possess antiferromagnetic transition at ~18 K,[18] which was apparently absent in our magnetic susceptibility measurements. However, the transition is well-observed in the temperature dependence of heat capacity (C_p) for clinoatacamite-rGO nanocomposite at zero and higher fields (1 T) along with the critical transition at ~6.2 K (Figure 2.4a). The anomaly observed at ~6.2 K could be due to the two-dimensional kagome layers which are weakly magnetically coupled to the interlayer Cu(II) ion and thus, it was susceptible to the applied magnetic field.[7,36] However, the one at ~18 K in the clinoatacamite-rGO nanocomposite was characteristic of an antiferromagnetic Néel ordering of clinoatacamite and did not vary significantly with the applied magnetic field.[36,37]

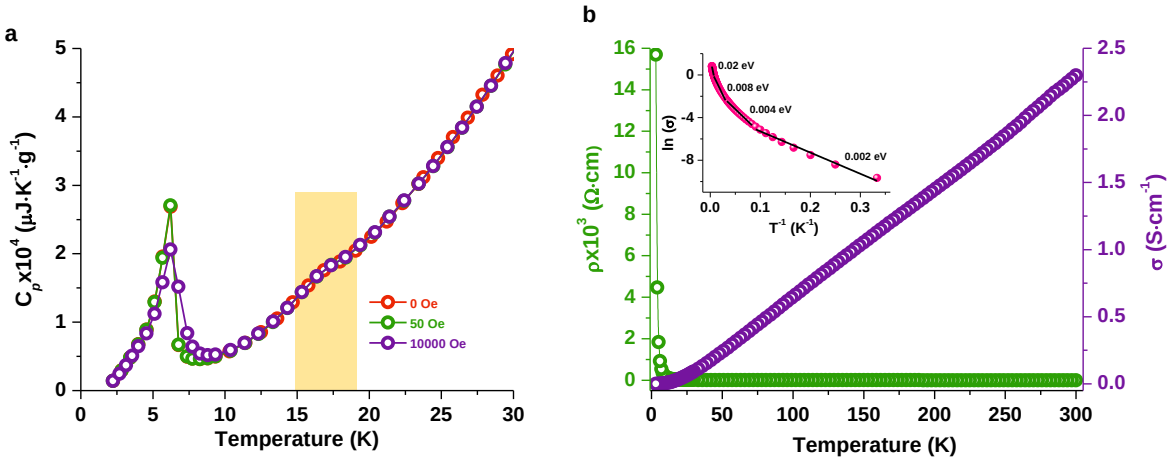

Figure 2.4. *(a) Specific heat capacity (C_p) of clinoatacamite-rGO nanocomposite as a function of temperature at varied fields. (b) Resistivity (ρ) and conductivity (σ) versus temperature plots of clinoatacamite-rGO nanocomposite recorded in PPMS (inset: Arrhenius plot).*

Electrical transport property of the clinoatacamite-rGO nanocomposite was investigated by four-probe resistivity measurements, and a value of ~200 $S \cdot m^{-1}$ at 300 K was measured (from physical property measurement system (PPMS) and a conventional Keithley source meter, Figure 2.4b and Appendix 2.12). The electrical conductivity value for the nanocomposite was found to be increasing with increasing temperature, both above and below 300 K – typical of a semiconductor.

The activation energy (E_a) estimated from the Arrhenius plot was found to be ~0.02 eV and ~0.05 eV in the temperature range of 140-300 K and 300-375 K, respectively (Figure 2.4b and Appendix 2.12 insets). The current−voltage (I−V) characteristic of pure rGO, extracted from the clinoatacamite-rGO nanocomposite, was Ohmic, and the conductivity value was estimated to be ~200 $S \cdot m^{-1}$ at 300 K (Appendix 2.13a).[38] Interestingly, a mechanical mixture of 10 wt % rGO with 90 wt % insulating clinoatacamite (resistance ≈ 10^{11} Ω; Appendix 2.13) revealed a very high resistance, ~10^{11} Ω at 300 K which is close to pristine clinoatacamite itself (Appendix 2.13). Apparently, the contribution of clinoatacamite to the resistivity of clinoatacamite-rGO nanocomposite is negligible (Figures 2.4b and Appendix 2.13). The Tauc plot revealed an optical band gap of ~1.5 eV for the clinoatacamite-rGO nanocomposite, a value significantly lower than that observed for pristine clinoatacamite (~2.67 eV) (Appendix 2.14).[39] Thus, our clinoatacamite-rGO nanocomposite indeed is a magnetic semiconductor. Magneto-transport measurements for such an exotic material will strengthen the understanding toward its application in spintronics.

2.4 Conclusions

In summary, we have demonstrated a novel method of embedding natural mineral clinoatacamite, possessing S=1/2 kagome-like lattice, into semiconducting reduced graphene oxide matrix. An unconventional precursor, Cu(I) salt, is employed to introduce a redox cycle in the synthesis, so as to reduce GO and form phase-pure clinoatacamite simultaneously, and such a unique approach of oxidation-reduction is anticipated to embed other analogues from the atacamite family into the rGO. The magnetic response of clinoatacamite-rGO nanocomposite revealed frustrated magnetic behaviour (T_{Cr} = 6.4 K) with a significantly improved value of H_C at 5 K compared to pristine clinoatacamite primarily assigned to be due to surface anisotropy. The electrical conductivity value of the clinoatacamite-rGO system was

impressive (~200 $S \cdot m^{-1}$ at 300 K), rendering the nanocomposite material magnetically as well as electronically intriguing. Further, our clinoatacamite-rGO system could provide an opportunity to study the influence of externally applied electric field on the frustration of quantum spins.

2.5 Appendix

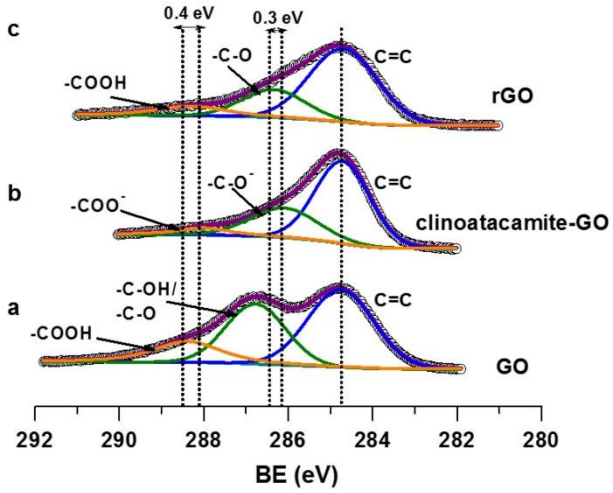

Appendix 2.1. *C1s XPS of GO (a), clinoatacamite-rGO nanocomposite (b), and rGO (c). Intensity ratio of rGO ($I_{C=C}/I_{(COOH+C-OH)}$):GO ($I_{C=C}/I_{(COOH+C-OH)}$) and Intensity ratio of clinoatacamite-rGO ($I_{C=C}/I_{(COOH+C-OH)}$):GO ($I_{C=C}/I_{(COOH+C-OH)}$) was consistently observed to be ~2:1 and thereby clearly confirmed the reduction process.*

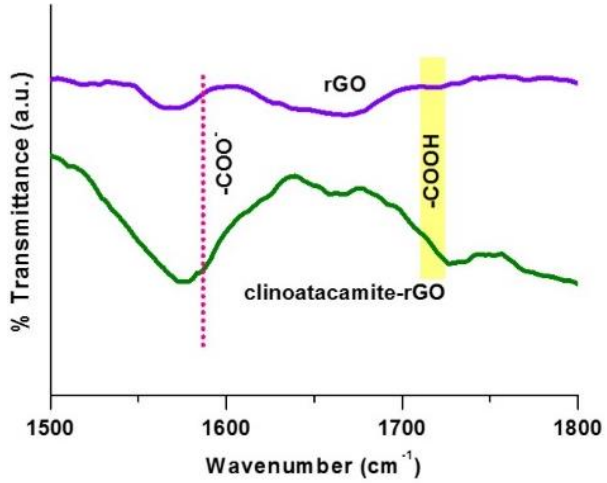

Appendix 2.2. *FTIR spectra of rGO and clinoatacamite-rGO nanocomposite.*

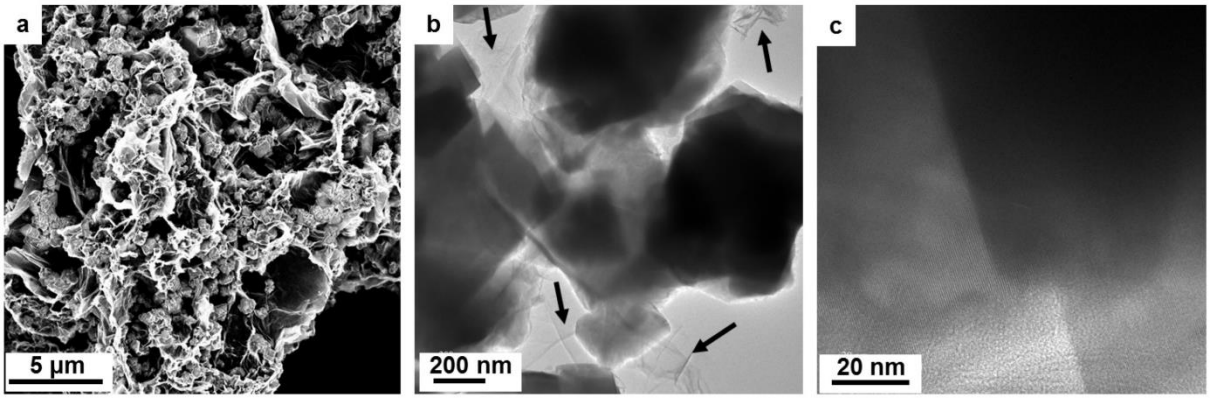

Appendix 2.3. *(a) FESEM and (b-c) HRTEM images of clinoatacamite-rGO nanocomposite (arrows point towards the rGO sheets).*

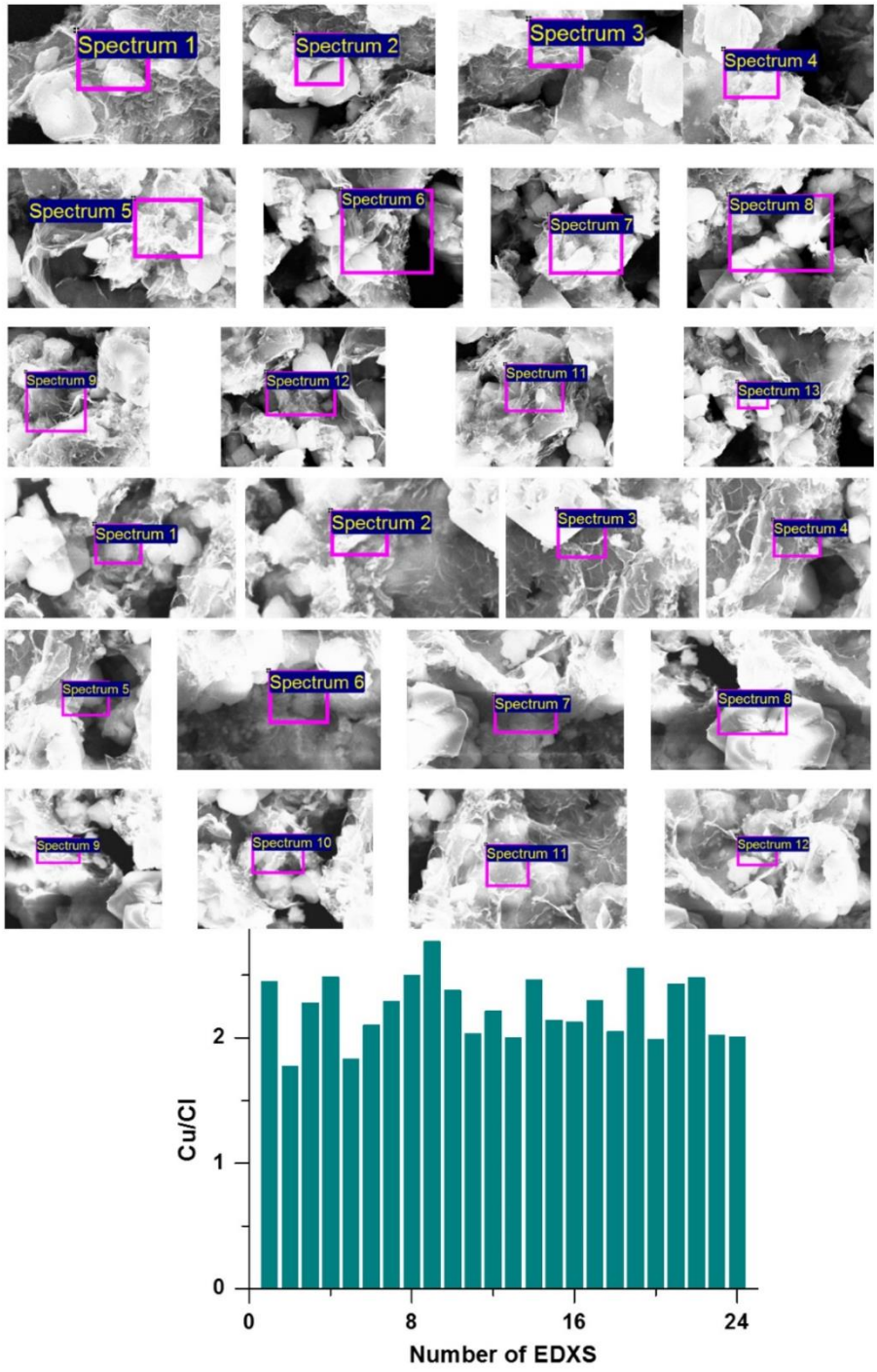

Appendix 2.4. *EDXS analysis of clinoatacamite-rGO nanocomposite at 24 different places. The average Cu:Cl ratio is ~2:1.*

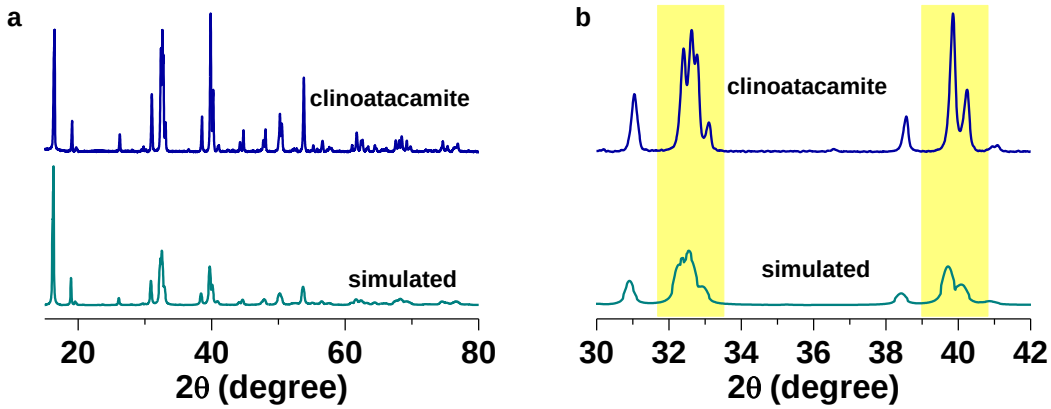

Appendix 2.5. *(a-b) PXRD patterns of pristine clinoatacamite (blue) and a simulated pattern (green).*

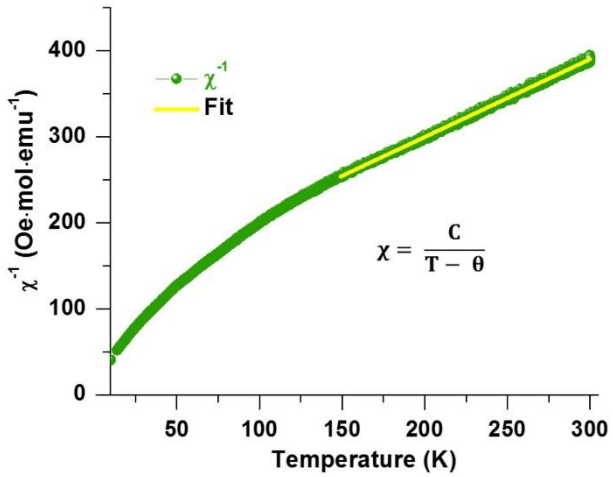

Appendix 2.6. *Inverse magnetic susceptibility versus temperature for clinoatacamite-rGO nanocomposite fitted with Curie-Weiss equation from 150 K to 300 K (inset: Curie-Weiss equation). The magnetic susceptibility of nanocomposite was normalised with respect to the mass of clinoatacamite only.*

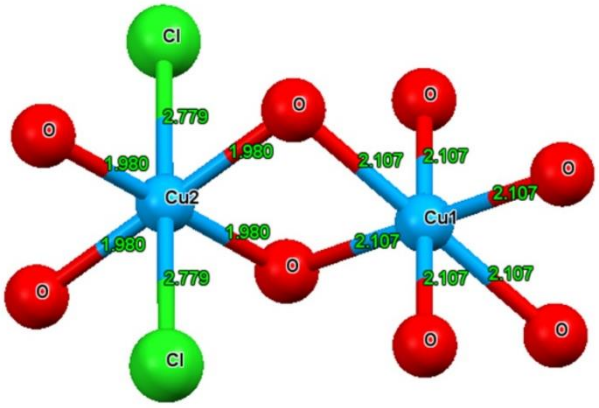

Appendix 2.7. *Cu(II) environment in clinoatacamite depicting the bond distances from chloride and oxo-bridging ligands (crystallographic information was taken from the Ref. 28).*

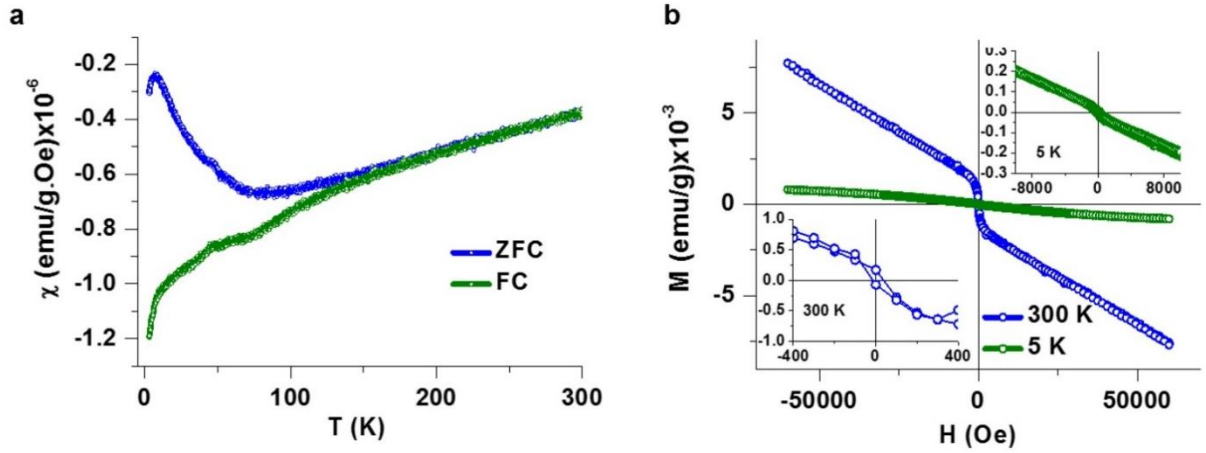

Appendix 2.8. *(a) Magnetic susceptibility versus temperature (χ-T) plot at an applied field of 50 Oe in FC and ZFC modes and (b) M-H plots at 300 K and 5 K for clean rGO after etching out the clinoatacamite.*

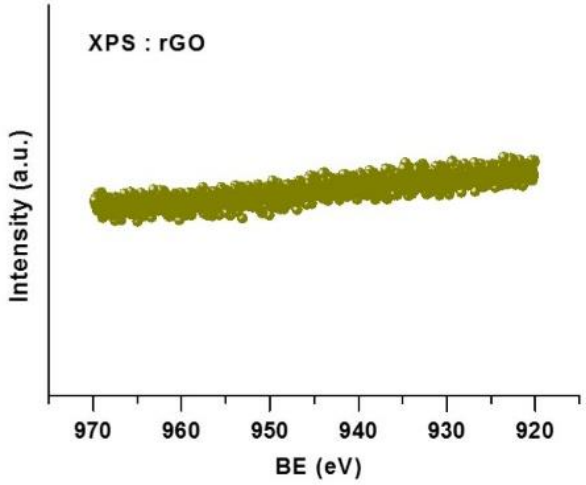

Appendix 2.9. *XPS spectrum of rGO recorded in the expected regime for Cu 2p.*

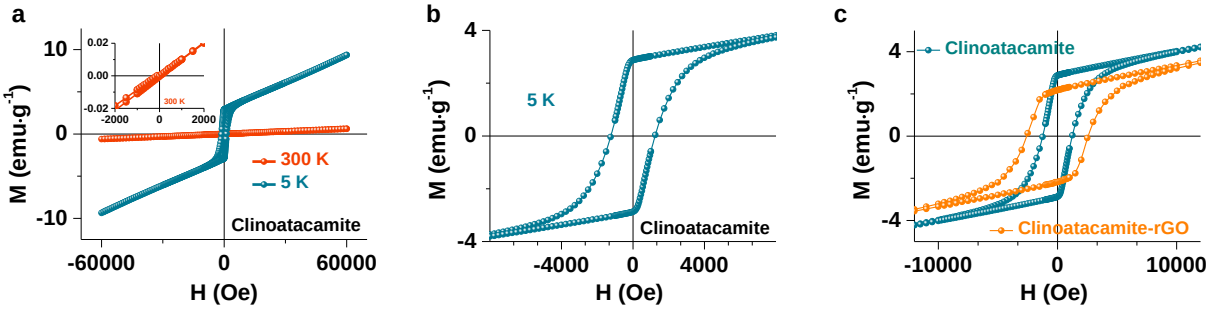

Appendix 2.10. *(a) M-H plots of pristine clinoatacamite recorded at 5 K and 300 K. (b) A zoomed-in M-H plot at 5 K. (c) M-H plots of pristine clinoatacamite and clinoatacamite-rGO nanocomposite at 5 K (M-H plot of the nanocomposite was normalised with respect to the mass of clinoatacamite only).*

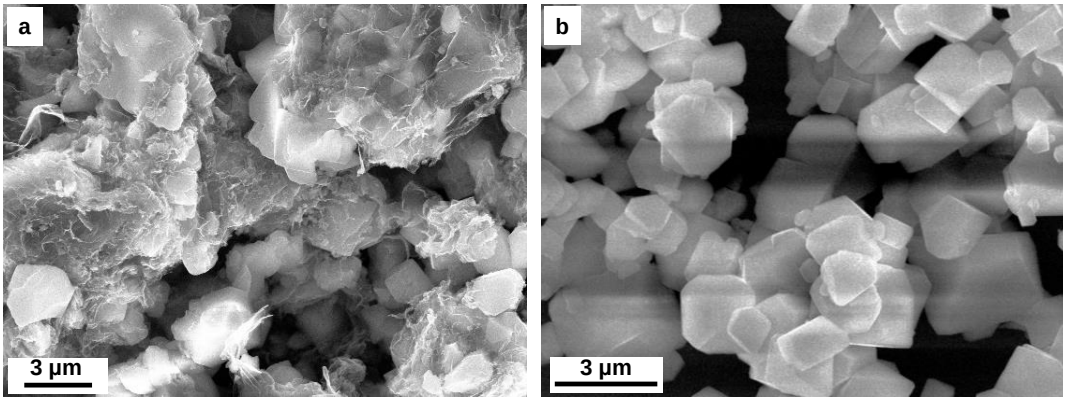

Appendix 2.11. *FESEM images of (a) clinoatacamite-rGO nanocomposite and (b) pristine clinoatacamite. Size of clinoatacamite in both cases is distributed in the range of 500 nm to 2 µm (these FESEM images were taken from a working distance of around 6.5 mm using 15 kV beam).*

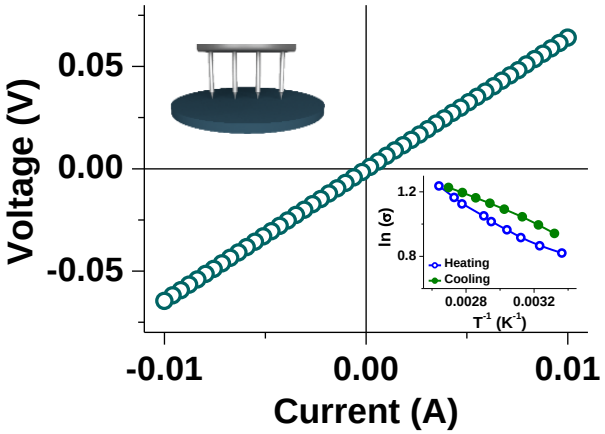

Appendix 2.12. *Four-probe dc current-voltage (I-V) plot of clinoatacamite-rGO nanocomposite at 300 K (inset: Arrhenius plot and four-probe setup used for the measurements).*

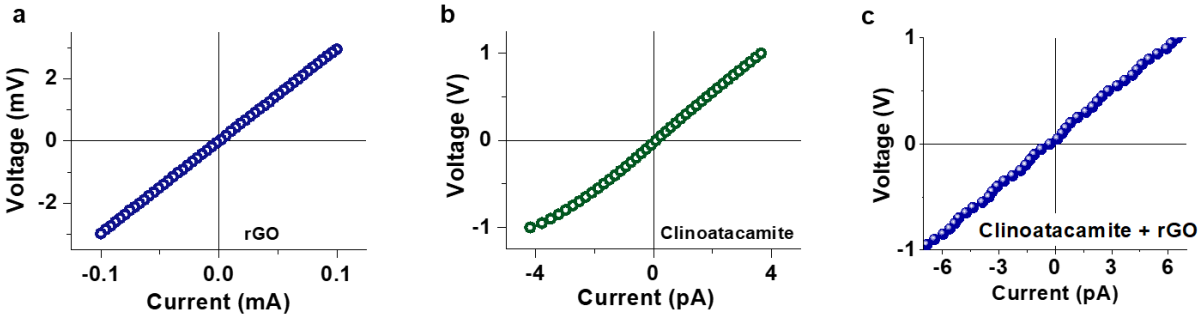

Appendix 2.13. *dc current-voltage (I-V) characteristics of (a) extracted pure rGO (thin film; four-probe), (b) pristine clinoatacamite (pelletized; two-probe), and (c) mechanical mixture of 10 wt% rGO and 90 wt% clinoatacamite (pelletized; two-probe).*

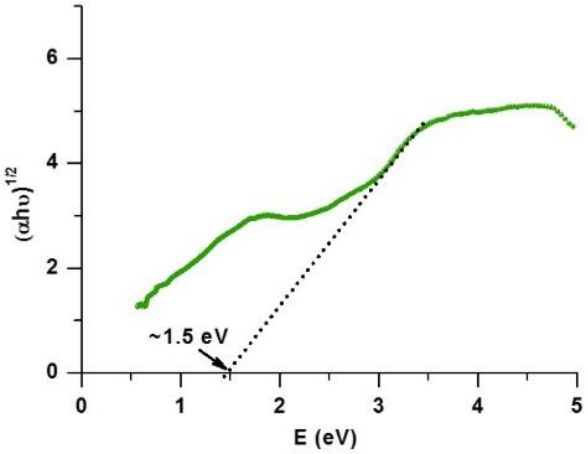

Appendix 2.14. *Tauc plot of clinoatacamite-rGO nanocomposite.*

2.6 References

(1) Balents, L. Spin Liquids in Frustrated Magnets. *Nature* **2010**, *464*, 199-208.

(2) Lee, P. A. An End to the Drought of Quantum Spin Liquids. *Science* **2008**, *321*, 1306-1307.

(3) Anderson, P. W. Resonating Valence Bonds: A New Kind of Insulator? *Mater. Res. Bull.* **1973**, *8*, 153-160.

(4) Ding, Z.-F.; Yang, Y.-X.; Zhang, J.; Tan, C.; Zhu, Z.-H.; Chen, G.; Shu, L. Possible Gapless Spin Liquid in the Rare-Earth Kagome Lattice Magnet $Tm_3Sb_3Zn_2O_{14}$. *Phys. Rev. B* **2018**, *98*, 174404-12.

(5) Wolf, S. A.; Awschalom, D. D.; Buhrman, R. A.; Daughton, J. M.; von Molnár, S.; Roukes, M. L.; Chtchelkanova, A. Y.; Treger, D. M. Spintronics: A Spin-Based Electronics Vision for the Future. *Science* **2001**, *294*, 1488-1495.

(6) Lacroix, C.; Mendels, P.; Mila, F. *Introduction to Frustrated Magnetism: Materials, Experiments, Theory*; Springer: Berlin, **2010**.

(7) Zheng, X.; Kubozono, H.; Nishiyama, K.; Higemoto, W.; Kawae, T.; Koda, A.; Xu, C. Coexistence of Long-Range Order and Spin Fluctuation in Geometrically Frustrated Clinoatacamite $Cu_2Cl(OH)_3$. *Phys. Rev. Lett.* **2005**, *95*, 057201-5.

(8) Lecheminant, P.; Bernu, B.; Lhuillier, C.; Pierre, L.; Sindzingre, P. Order Versus Disorder in the Quantum Heisenberg Antiferromagnet on the Kagomé Lattice Using Exact Spectra Analysis. *Physical Review B* **1997**, *56*, 2521-2529.

(9) Ran, Y.; Hermele, M.; Lee, P. A.; Wen, X.-G. Projected-Wave-Function Study of the Spin-1/2 Heisenberg Model on the Kagomé Lattice. *Phys. Rev. Lett.* **2007**, *98*, 117205-9.

(10) Braithwaite, R.; Mereiter, K.; Paar, W.; Clark, A. Herbertsmithite, $Cu_3Zn(OH)_6Cl_2$, a New Species, and the Definition of Paratacamite. *Mineral. Mag.* **2004**, *68*, 527-539.

(11) De Vries, M.; Kamenev, K.; Kockelmann, W.; Sanchez-Benitez, J.; Harrison, A. Magnetic Ground State of an Experimental S= 1/2 Kagome Antiferromagnet. *Phys. Rev. Lett.* **2008**, *100*, 157205-9.

(12) Shores, M. P.; Nytko, E. A.; Bartlett, B. M.; Nocera, D. G. A Structurally Perfect S = 1/2 Kagomé Antiferromagnet. *J. Am. Chem. Soc.* **2005**, *127*, 13462-13463.

(13) Wills, A.; Perring, T.; Raymond, S.; Fåk, B.; Henry, J.; Telling, M. In Inelastic Neutron Scattering Studies of the Quantum Frustrated Magnet Clinoatacamite, γ-$Cu_2(OD)_3Cl$, a Proposed Valence Bond Solid (VBS). *J. Phys.: Conf. Ser.* **2009**, *145*, 012056-60.

(14) Harris, M. J.; Zinkin, M. P. Frustration in the Pyrochlore Antiferromagnets. *Mod. Phys. Lett. B* **1996**, *10*, 417-438.

(15) Engelbrekt, C.; Malcho, P.; Andersen, J.; Zhang, L.; Ståhl, K.; Li, B.; Hu, J.; Zhang, J. Selective Synthesis of Clinoatacamite $Cu_2(OH)_3Cl$ and Tenorite Cuo Nanoparticles by pH Control. *J. Nanopart. Res.* **2014**, *16*, 2562-74.

(16) Chu, S.; Müller, P.; Nocera, D. G.; Lee, Y. S. Hydrothermal Growth of Single Crystals of the Quantum Magnets: Clinoatacamite, Paratacamite, and Herbertsmithite. *Appl. Phys. Lett.* **2011**, *98*, 092508-11.

(17) Chu, S.; McQueen, T. M.; Chisnell, R.; Freedman, D. E.; Müller, P.; Lee, Y. S.; Nocera, D. G. A Cu^{2+} (S= 1/2) Kagomé Antiferromagnet: $Mg_XCu_{4-X}(OH)_6Cl_2$. *J. Am. Chem. Soc.* **2010**, *132*, 5570-5571.

(18) Zheng, X.; Kawae, T.; Kashitani, Y.; Li, C.; Tateiwa, N.; Takeda, K.; Yamada, H.; Xu, C.; Ren, Y. Unconventional Magnetic Transitions in the Mineral Clinoatacamite $Cu_2Cl(OH)_3$. *Phys. Rev. B* **2005**, *71*, 052409-13.

(19) Jha, P. K.; Singh, S. K.; Kumar, V.; Rana, S.; Kurungot, S.; Ballav, N. High-Level Supercapacitive Performance of Chemically Reduced Graphene Oxide. *Chem* **2017**, *3*, 846-860.

(20) Roberts, A. C.; Szymanski, J. T.; Grice, J. D.; Dutrizac, J. E.; Jambor, J. L. Clinoatacamite, a New Polymorph of $Cu_2(OH)_3Cl$, and Its Relationship to Paratacamite and "Anarakite". *Can. Mineral.* **1996**, *34*, 61-72.

(21) Moon, I. K.; Lee, J.; Ruoff, R. S.; Lee, H. Reduced Graphene Oxide by Chemical Graphitization. *Nat. Commun.* **2010**, *1*, 73-79.

(22) Hüfner, S.; *Photoelectron Spectroscopy: Principles and Applications*; Springer: Berlin, **2003**.

(23) Rana, S.; Prasoon, A.; Sadhukhan, P.; Jha, P. K.; Sathe, V.; Barman, S. R.; Ballav, N. Spontaneous Reduction of Copper(II) to Copper(I) at Solid–Liquid Interface. *J. Phys. Chem. Lett.* **2018**, *9*, 6364-6371.

(24) Huang, L.; Jiang, J.; Ai, L. Interlayer Expansion of Layered Cobalt Hydroxide Nanobelts to Highly Improve Oxygen Evolution Electrocatalysis. *ACS Appl. Mater. Interfaces* **2017**, *9*, 7059-7067.

(25) Fleutot, S.; Martinez, H.; Dupin, J. C.; Baraille, I.; Forano, C.; Renaudin, G.; Gonbeau, D. Experimental (X-Ray Photoelectron Spectroscopy) and Theoretical Studies of Benzene Based Organics Intercalated into Layered Double Hydroxide. *Solid State Sci.* **2011**, *13*, 1676-1686.

(26) Gupta, K.; Dadwal, A.; Rana, S.; Jha, P. K.; Jain, A.; Yusuf, S. M.; Joy, P. A.; Ballav, N. Metamagnetism in Nanosheets of Co^{II}-MOF with T_N at 26 K and a Giant Hysteretic Effect at 5 K. *Inorg. Chem.* **2018**, *57*, 15044-15047.

(27) Lenin, R.; Joy, P. A. Role of Primary and Secondary Surfactant Layers on the Thermal Conductivity of Lauric Acid Coated Magnetite Nanofluids. *J. Phys. Chem. C* **2016**, *120*, 11640-11651.

(28) Wills, A.; Henry, J. On the Crystal and Magnetic Ordering Structures of Clinoatacamite, γ-$Cu_2(OD)_3Cl$, a Proposed Valence Bond Solid. *J. Phys.: Condens. Matter* **2008**, *20*, 472206-14.

(29) Ramirez, A. Strongly Geometrically Frustrated Magnets. *Annu. Rev. Mater. Sci.* **1994**, *24*, 453-480.

(30) Fraile Rodríguez, A.; Kleibert, A.; Bansmann, J.; Voitkans, A.; Heyderman, L. J.; Nolting, F. Size-Dependent Spin Structures in Iron Nanoparticles. *Phys. Rev. Lett.* **2010**, *104*, 127201.

(31) Sung Lee, J.; Myung Cha, J.; Young Yoon, H.; Lee, J.-K.; Keun Kim, Y. Magnetic Multi-Granule Nanoclusters: A Model System That Exhibits Universal Size Effect of Magnetic Coercivity. *Sci. Rep.* **2015**, *5*, 12135.

(32) Kodama, R. H.; Berkowitz, A. E. Atomic-Scale Magnetic Modeling of Oxide Nanoparticles. *Phys. Rev. B: Condens. Matter Mater. Phys.* **1999**, *59*, 6321−6336.

(33) Kodama, R. H. Magnetic Nanoparticles. *J. Magn. Magn. Mater.* **1999**, *200*, 359−372.

(34) Leighton, C.; Nogués, J.; Jönsson-Åkerman, B. J.; Schuller, I. K. Coercivity Enhancement in Exchange Biased Systems Driven by Interfacial Magnetic Frustration. *Phys. Rev. Lett.* **2000**, *84*, 3466− 3469.

(35) Zhao, Z. L.; Ding, J.; Chen, J. S.; Wang, J. P. Coercivity Enhancement by Ru Pinning Layer in FePt Thin Films. J. *Appl. Phys.* **2003**, *93*, 7753−7755.

(36) Morodomi, H.; Ienaga, K.; Inagaki, Y.; Kawae, T.; Hagiwara, M.; Zheng, X. G. Specific Heat Study of Geometrically Frustrated Magnet Clinoatacamite $Cu_2Cl(OH)_3$. *J. Phys.: Conf. Ser.* **2010**, *200*, 032047-51.

(37) Morodomi, H.; Ienaga, K.; Inagaki, Y.; Kawae, T.; Hagiwara, M.; Zheng, X. G. Magnetic Field Dependence of Specific Heat in Clinoatacamite $Cu_2Cl(OH)_3$. *J. Phys.: Conf. Ser.* **2012**, *400*, 032058-62.

(38) Jha, P. K.; Gupta, K.; Debnath, A. K.; Rana, S.; Sharma, R.; Ballav, N. 3D Mesoporous Reduced Graphene Oxide with Remarkable Supercapacitive Performance. *Carbon* **2019**, *148*, 354− 360.

(39) Liu, X.; Xu, L.; Huang, Y.; Cheng, H.; Seo, H. J. Paratacamite Phase Stability and Improved Optical Properties of $Cu_2(OH)_3Cl$ Crystal via Ni-Doping. *Mater. Des.* **2017**, *121*, 194-201.

Chapter 3

Barlowite – S=1/2 Antiferromagnet Possessing Kagome Planes onto Reduced Graphene Oxide

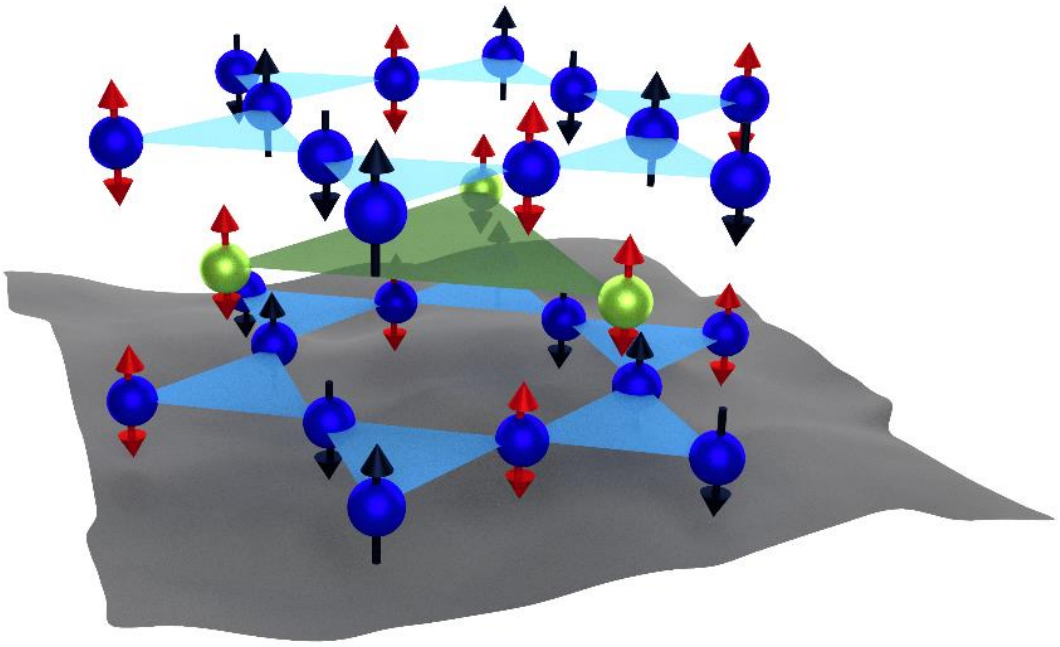

3.1 Introduction

Quantum spin liquids (QSLs) constitute a distinct class of matter, manifesting fluctuating spins throughout the lattice – a long range spin entanglement.[1-3] Such systems possess strong competing nearest neighbour interactions bringing spin frustration which, in turn, suppresses the long range magnetic ordering down to the lowest temperature.[4] Though, geometrically frustrated lattices have been extensively searched for a QSL ground state, the focus has majorly centered on low-dimensional S=1/2 spin lattices, such as triangular or kagome lattices with antiferromagnetically interacting spins.[5-10] So far, S=1/2 kagome spin lattice is sought to be an ideal candidate to host a QSL state where one of the leading candidates with experimentally observed QSL features is herbertsmithite [$Cu_3Zn(OH)_6Cl_2$] – a naturally occurring mineral from the family of atacamites.[6, 11]

Herbertsmithite has a three-dimensional (3D) structural lattice of alternately stacked kagome and triangular planes (pyrochlore lattice), where the triangular planes are all occupied by diamagnetic Zn(II) ions and the kagome planes with Cu(II) ions, thus rendering a two-dimensional (2D) S=1/2 kagome spin lattice – a host for QSL.[6] Herbertsmithite is, in fact, realized by replacing 1/4th of Cu(II) ions with Zn(II) ions in clinoatacamite [$Cu_4(OH)_6Cl_2$] i.e., occupying all the interlayer sites between kagome planes by Zn(II) ions.[6, 11-12] In clinoatacamite, spins within a kagome plane interact antiferromagnetically, however, the interlayer sites offers Cu-O-Cu angle of ~97° with a favourable ferromagnetic interaction as also observed for paratacamite [$Cu_{4-x}Zn_x(OH)_6Cl_2$, $0.33 \leq x < 1$], having a combination of Cu(II) and Zn(II) ions at the interlayer site.[12-13] Notably, the coordination environment of metal ions within the kagome plane and at the interlayer site is similar in herbertsmithite, which often gives rise to anti-site disorder i.e., presence of Cu(II) ions at the interlayer site or Zn(II) ions in the kagome plane.[6, 14] The stoichiometry of Cu(II) and Zn(II) ions in herbertsmithite can be estimated, however, due to similar sizes and diffraction properties of Cu(II) and Zn(II) ions,[15] anti-site disorder mostly remains undetectable and a plight, for herbertsmithite, demanding for an alternative. This renewed the interest recently in barlowite [$Cu_4(OH)_6FBr$] – another member of atacamite family of minerals, having Cu(II) based S=1/2 kagome planes with a weaker inter-kagome coupling (Figure 3.1).[7] In the case of barlowite, kagome planes are stacked exactly over one another giving rise to a trigonal prismatic interlayer site, unlike ABC packing of kagome planes in herbertsmithite with a trigonally compressed octahedral interlayer site, thus reducing the chance of Cu(II) ions occupying interlayer site over the site in kagome plane with pronounced Jahn-Teller distortion (Appendix 3.1).[16-18] Further, as a result of

reduced inter kagome coupling in barlowite, only ≥56% occupancy of the interlayer site with a diamagnetic ion is required to generate a robust QSL state despite the Cu(II) impurities in the interlayer site.[7, 19]

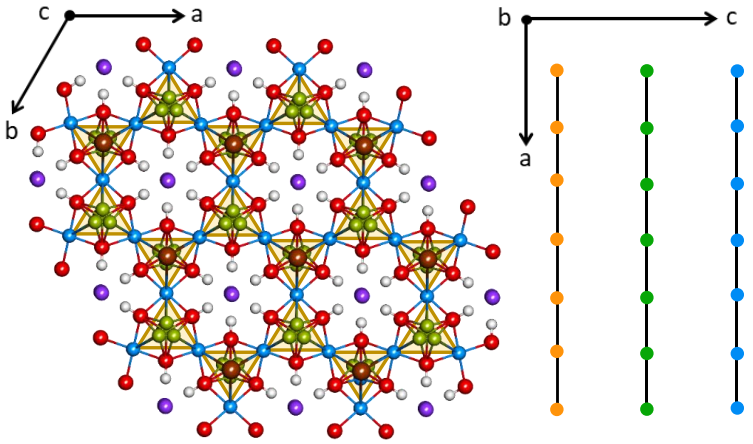

Figure 3.1. *View along crystallographic c-axis (left panel) depicting top view of kagome plane, and b-axis (right panel) depicting the stacking of kagome planes in barlowite, only Cu(II) ions are shown in the right panel for clarity. (Color code: blue, green, orange-Cu in consecutive kagome planes; dark yellow-Cu at interlayer site; red-O; brown-Br; purple-F; white-H).*

These interesting members of atacamite family of minerals are, however, difficult to synthesize chemically in phase-pure forms and have been produced majorly from Cu(II) source via hydrothermal or other high temperature protocols.[6, 16-17, 20-23] Recently, we have shown a simple oxidation-reduction reaction starting from Cu(I) precursor along with different counter anions, chloride and bromide, to successfully yield phase pure clinoatacamite and botallackite [$Cu_2(OH)_3Br$], respectively, under suitable conditions.[24-25] Employing a Cu(I) precursor, not only enabled us to synthesize these frustrated magnets at close-to-ambient conditions but also gave an opportunity to explore the oxidation process of Cu(I) to Cu(II) to bring such frustrated magnets and exotic matrices into a single material.[24-25] Here we show, a robust synthesis of barlowite starting from Cu(I) precursor along with a combination of anions (fluoride and bromide) below the boiling point of water in aqueous medium. Further graphene oxide (GO) was added into the reaction mixture as an additional chemical precursor where Cu(I) act as a reducing agent for GO resulting in the formation of reduced graphene oxide (rGO) and Cu(I) itself oxidizes to Cu(II), as a result, barlowite crystallites were integrated with rGO sheets generating a magnetic semiconductor, here named as barlowite-rGO nanocomposite. Further, barlowite is known in literature to possess two morphologies, rod-like and hexagonal plate-like morphology exhibiting distinct magnetic transitions,[20] and we anticipate the alteration in here

demonstrated protocol could lead to the generation of both the morphologies which will enable us to further investigate the synthesis-dependent properties of barlowite over rGO and is currently under investigation with preliminary data.

3.2 Materials and Methods

Graphite flake (+100 mesh), potassium permanganate ($KMnO_4$), hydrogen peroxide (H_2O_2), copper bromide (CuBr), hydrobromic acid (HBr), and ammonium fluoride (NH_4F) were ordered from Sigma-Aldrich. Sodium hydroxide (NaOH) was purchased from Vetec. Sulfuric acid (H_2SO_4) and methanol (MeOH) were brought from RANKEM (India). Millipore water (MQ, ~18.2 MΩ·cm) was used whenever required. Graphene oxide (GO) was prepared and well characterized by following a literature report.[26] Aqueous solution (~1mg/mL) of GO was subsequently prepared and centrifuged at 1000 rpm to remove the multilayers, if any, before further use.

Synthesis of barlowite: CuBr (~322.7 mg, ~2.25 mmol), NaOH (~90mg, ~2.25 mmol), HBr (~122 μL, ~2.25 mmol), and NH_4F (~83.3 mg, ~2.25 mmol) were added to a flask with 100 mL MQ water and stirred at ~94 °C for 24 h. The green coloured product thus obtained was washed with MQ water and MeOH followed by vacuum drying before further characterization and experiments.

Synthesis of barlowite-rGO nanocomposite: Aqueous dispersion (50 mL) of CuBr (~322.7 mg, ~2.25 mmol), NaOH (~90mg, ~2.25 mmol), HBr (~122 μL, ~2.25 mmol), and NH_4F (~83.3 mg, ~2.25 mmol) was added to a flask with 50 mL aqueous GO dispersion and the reaction mixture was stirred at ~94 °C for 24 h. The greenish black coloured product thus obtained was washed with MQ water and MeOH and was vacuum dried before further characterization and experiments.

Magnetic response was recorded on a SQUID vibrating sample magnetometer (Quantum Design). Magnetization was recorded in field-cooled (FC) mode by cooling the sample in 50 Oe applied magnetic field and recording the magnetization in same field while warming. Zero field-cooled (ZFC) magnetization was recorded after cooling the sample in zero applied magnetic field and recording the magnetization in 50 Oe field while warming. The ac magnetic susceptibility measurements were carried out in a CRYOGENIC make Vibrating Sample Magnetometer (VSM) under zero field condition (ZFC). The measurement was carried out in warming cycle. Raman spectroscopy was done on powder samples using a 514 nm laser on Horiba Jobin Yvon Raman microscope. Heat capacity was recorded in a Quantum Design-

PPMS-Evercool II instrument. PXRD patterns were recorded on Bruker D8 Advance diffractometer with Cu Kα radiation (λ = 1.5406 Å); 2θ range of 10−40°. FTIR spectrum was recorded on a pressed pellet of powder sample mixed with KBr on NICOLET 6700 spectrophotometer. FESEM images were taken under a Zeiss Ultra Plus scanning electron microscope over a Si wafer where methanolic dispersion of the sample was drop casted and dried. HRTEM images of the samples were taken on drop casted samples (methanolic dispersion) over a 200 mesh Cu grid in a JEM-2200FS transmission electron microscope. Temperature dependent four-probe DC electrical conductivity (I−V) measurements were done on conventional Keithley 6221 setup on a pelletized sample. Two-probe DC electrical conductivity (I−V) measurements were done via Keithley 4200 SCS Parameter Analyzer system equipped with an Everbeing probe station on a pelletized sample.

3.3 Results and Discussion

Pristine barlowite was synthesized by stirring an aqueous solution of CuBr and NH_4F along with other reagents at ~94 °C for 24 h. The isolated green product was characterized by powder X-ray diffraction (PXRD) technique indicating the formation of phase pure barlowite where the experimentally recorded pattern for here synthesized barlowite matches well with the simulated pattern reported for pristine barlowite (Figure 3.2a).[18] FTIR spectrum of barlowite exhibited strong bands at ~558 cm^{-1}, ~851 cm^{-1}, ~1029 cm^{-1}, ~1063 cm^{-1}, ~3273 cm^{-1}, and a broad hump at ~2000 cm^{-1}; where the bands in the range of 400-700 cm^{-1} are assigned to Cu-O stretching, and those from ~700 to ~1060 cm^{-1} are ascribed to CuO-H deformations (Appendix 3.2).[20, 27] Appendix 3.3 shows the Raman spectrum of barlowite with peaks at ~75 cm^{-1}, ~185 cm^{-1}, ~443 cm^{-1}, and ~523 cm^{-1}, in line with the literature reports, confirming the formation of barlowite without any impurities.[20]

Field-emission scanning electron microscopic (FESEM) and high-resolution transmission electron microscopic (HRTEM) images revealed the rod-like morphology of here synthesized barlowite with the length of rods varying from micro- to nano-metre range which is a result of varied stacking of kagome planes along the crystallographic c-axis at different nucleation sites (Figure 3.2b and c). Thorough energy dispersive X-ray spectroscopic (EDXS) analysis was done to estimate the stoichiometry of Br:F in barlowite and an average value of ~1:1 was observed (Appendix 3.4).

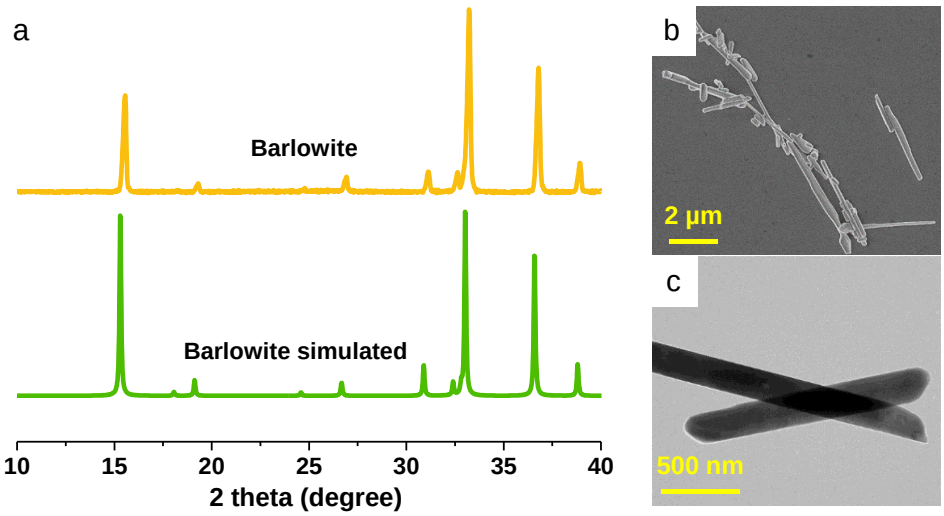

Figure 3.2. *(a) PXRD pattern, (b) FESEM image, and (c) HRTEM image of barlowite.*

To further explore the oxidation process of Cu(I) to Cu(II), GO was introduced in the reaction mixture, without changing the other reaction conditions, to synthesize barlowite-rGO nanocomposite. PXRD pattern of barlowite-rGO nanocomposite is similar to that of pristine barlowite confirming the formation of phase-pure barlowite in the nanocomposite, also, the Raman signatures of barlowite were maintained in the nanocomposite with peaks situated at ~75 cm^{-1}, ~185 cm^{-1}, ~443 cm^{-1}, and ~523 cm^{-1} (Appendix 3.5 and 3.3).[20] Further, barlowite crystallites with rod-like morphology and polydispersity similar to pristine barlowite were observed to be extensively wrapped with rGO sheets from the FESEM and HRTEM images of barlowite-rGO nanocomposite (Appendix 3.6). The Br:F stoichiometry of ~1:1 was observed for barlowite-rGO nanocomposite from EDXS analysis.

The dc magnetic susceptibility of barlowite was recorded as a function of temperature at an externally applied field of strength 50 Oe. A long range ordered state appeared for here synthesized barlowite, corresponding to the Néel transition with a broad cusp at ~16.0 K spanning over a range of ~2 K (14 – 16 K) as also suggested by Goodenough-Kanamori-Anderson (GKA) rules (Figure 3.3a).[28] Barlowite, in literature, is known to possess Néel temperature around 15.4 K with some ferromagnetic moment followed by a second transition at around 13.8 K.[16] The inverse susceptibility plot for barlowite in the temperature range of 200 – 300 K was fitted with Curie-Weiss equation, $\chi=C/(T-\theta_{CW})$ and the value of Weiss temperature (θ_{CW}) was found to be -184.9 K indicating a strong antiferromagnetic interaction between the spins, and the value of curie constant was observed to be ~2.53 $emu \cdot Oe^{-1} \cdot mol^{-1} \cdot K$ (Appendix 3.7a). The antiferromagnetic interaction predicted by the Curie-Weiss law is highly

suppressed in barlowite due to high spin frustration in the lattice as also reflected in the value of frustration factor *f* (= $|\theta_{CW}|/T_{Cr}$), 12.3 (*f* > 10 indicates high magnetic frustration). Magnetization as a function of externally applied magnetic field (M-H) was recorded at 300 K and 3 K. At 300 K, a straight-lined M-H curve without any cusp – characteristic of paramagnetic behavior was observed (Figure 3.3b). While at 3 K, a coercive field (H_C) of ~600 Oe was observed without any saturation of magnetization even at an applied field of 60 kOe indicating the presence of non-collinearly aligned spins in the frustrated lattice of barlowite (Figure 3.3b). At room temperature, the interlayer site in barlowite exhibits dynamic disorder at three possible positions to maintain the geometrically perfect kagome motif in the lattice with hexagonal symmetry. As the temperature is lowered to 276 K, the Cu(II) ions at the interlayer site occupy one of the three available positions, thus lowering the symmetry of the lattice.[29] Below 276 K, the spin lattice of barlowite bears a resemblance to the spin lattice of clinoatacamite, in the sense, that there are S=1/2 antiferromagnetic kagome planes linked via Cu(II) sites favouring ferromagnetic inter-plane interactions, however, no long range order is observed because of high spin frustration until further low temperatures.[24]

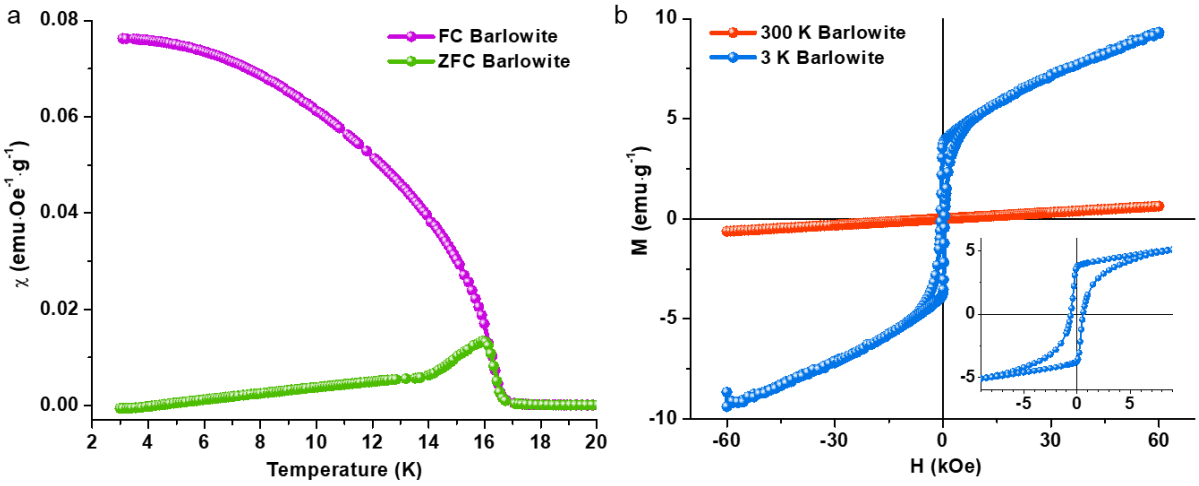

Figure 3.3. *(a) dc magnetic susceptibility at an externally applied field of 50 Oe, and (b) M-H plots at 300 K and 3 K of barlowite.*

Figure 3.4 depicts the ac magnetic susceptibility (χ'_{ac}) as a function of temperature under varied frequencies and zero applied dc magnetic field, where a peak independent of frequency was observed, characteristic of Néel ordering. The peak is centered at ~16.7 K, corroborating the onset of increase in magnetization in the dc susceptibility plot corresponding to the Néel transition in barlowite (Figure 3.4).

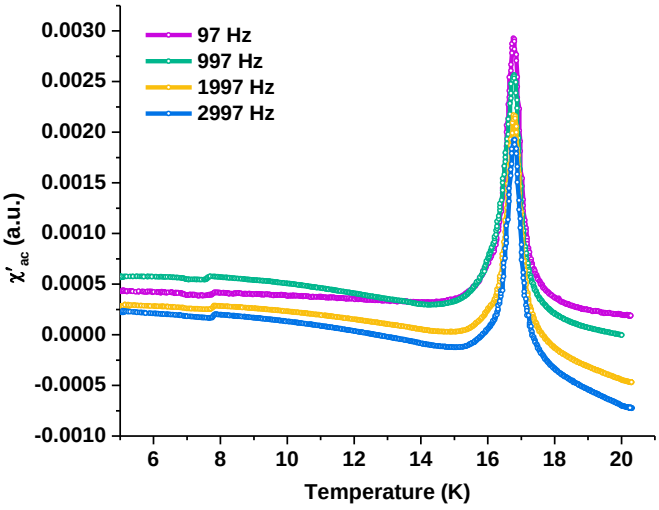

Figure 3.4. *ac magnetic susceptibility (χ'_{ac}) of barlowite as a function of temperature at varied applied frequencies and zero applied dc magnetic field.*

Additionally, heat capacity was recorded at various externally applied magnetic fields and a clear transition is observed at ~15.8 K and interestingly, the transition shifts to higher temperatures at high externally applied magnetic fields ca. 2000 Oe suggesting that the specific heat at low temperatures is majorly magnetic (Figure 3.5a).[16]

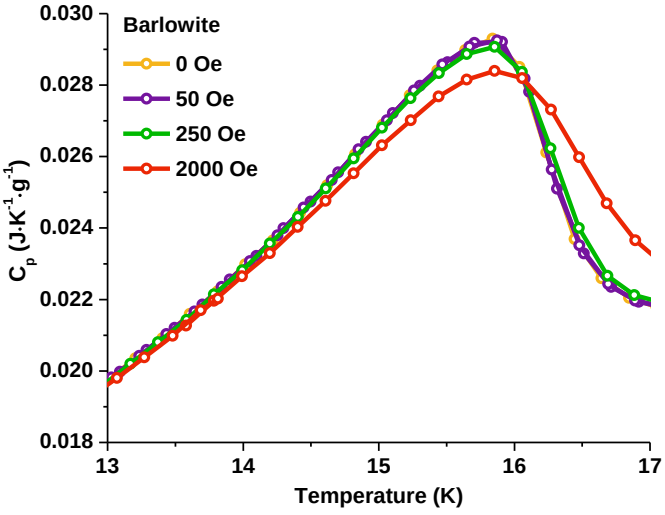

Figure 3.5. *Specific heat recorded at varied applied magnetic fields versus temperature for barlowite.*

In the case of barlowite-rGO nanocomposite, the magnetic signatures of pristine barlowite were retained. Magnetic susceptibility was recorded at an applied magnetic field of 50 Oe and a cusp at around 15 K is observed in the ZFC curve signifying the antiferromagnetic transition (Figure 3.6a). Owing to the presence of semiconducting rGO in the nanocomposite, electrical transport properties were investigated for both the samples. For barlowite, a resistance value of ~2.0*10^{10}

Ω was estimated from the I-V plot at 300 K, recorded in two-probe configuration, revealing the electrically insulating behavior of pristine barlowite, however, barlowite-rGO nanocomposite offered an electrical conductivity value of ~85 $S \cdot m^{-1}$ at 300 K, recorded in four-probe configuration (Figure 3.6b).

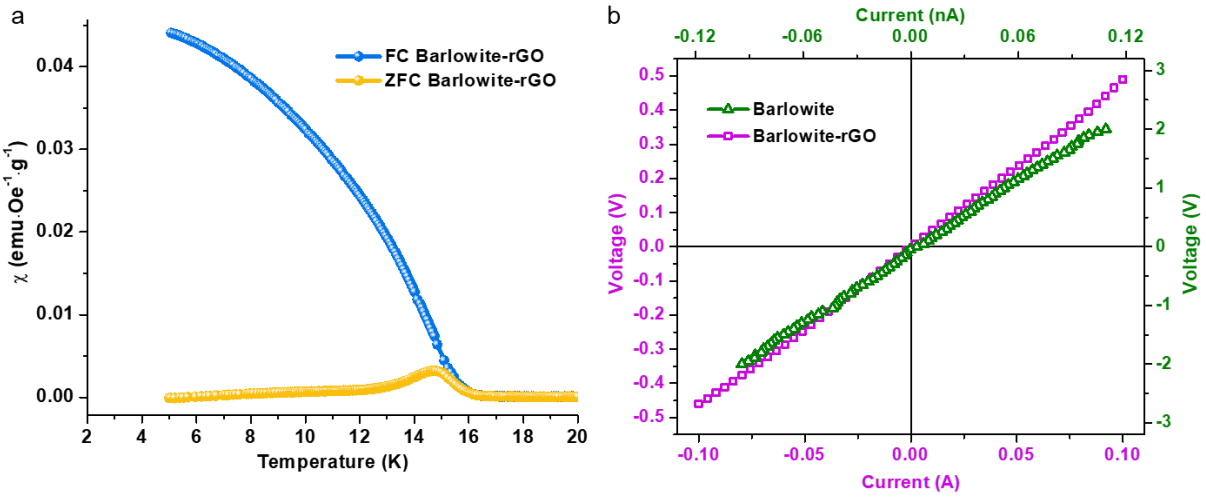

Figure 3.6. *(a) dc magnetic susceptibility of barlowite-rGO nanocomposite at an applied field of 50 Oe; and (b) I-V characteristics of barlowite and barlowite-rGO nanocomposite recorded at 300 K in two-probe and four-probe configuration, respectively.*

Further, I-V plot of the mechanical mixture of two components with a composition similar to the nanocomposite (~85 wt% barlowite + ~15 wt% rGO), gave a resistance value of ~$3.8*10^{10}$ Ω at 300 K, thus ruling out the possibility of formation of mechanical mixture in barlowite-rGO system (Appendix 3.8b).

3.4 Conclusions

In summary, we have demonstrated a simple and straightforward protocol to synthesis phase-pure Cu(II) based frustrated magnet named barlowite, possessing geometrically perfect S=1/2 kagome motif. We employed an unconventional Cu(I) precursor in the abovementioned robust synthetic protocol and by introducing graphene oxide (GO) as an additional precursor, we were able to anchor barlowite onto nanosheets of reduced GO (rGO), integrating the magnetic characteristics of barlowite with the electrical transport properties of rGO engendering barlowite-rGO systems as a magnetic semiconductor. The oxidation-reduction approach to synthesize phase-pure barlowite and in situ anchoring onto rGO sheets presented here can potentially be extended to other spin lattices as well generating an interesting class of magnetic semiconductors.

3.5 Appendix

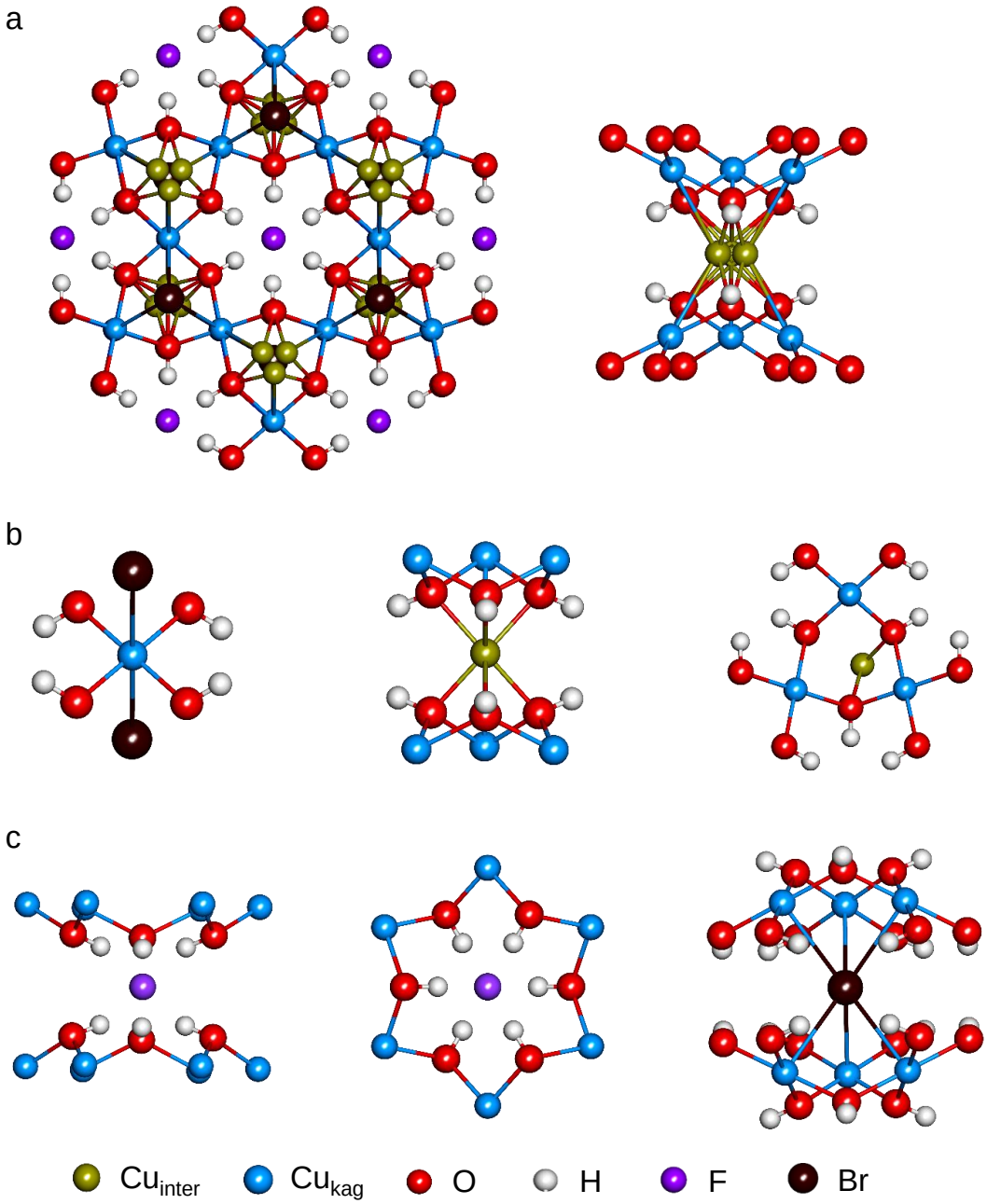

Appendix 3.1. *Structural insight into barlowite (adopted form Ref. 18); (a) top view of the kagome plane (left) and stacking via interlayer site (right); (b) coordination environment of two distinct Cu(II) sites; (c) coordination environment of fluoride and bromide in the structure.*

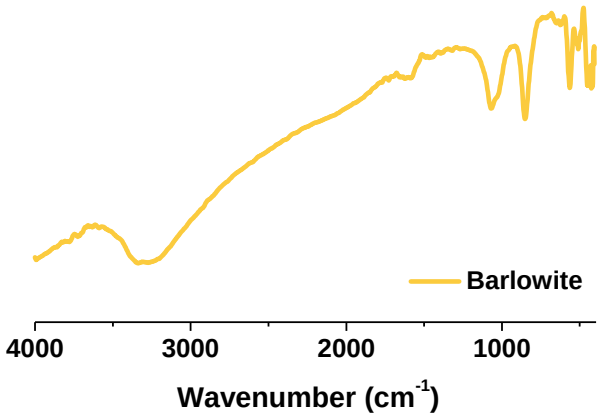

Appendix 3.2. *FTIR spectrum of pristine barlowite.*

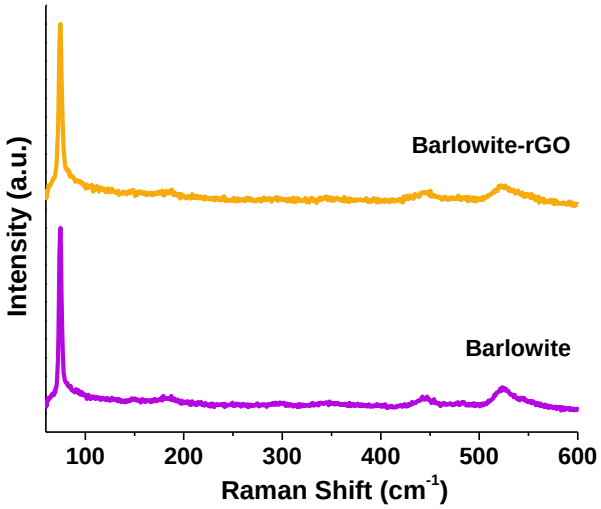

Appendix 3.3. *Raman spectra of pristine barlowite and barlowite-rGO nanocomposite.*

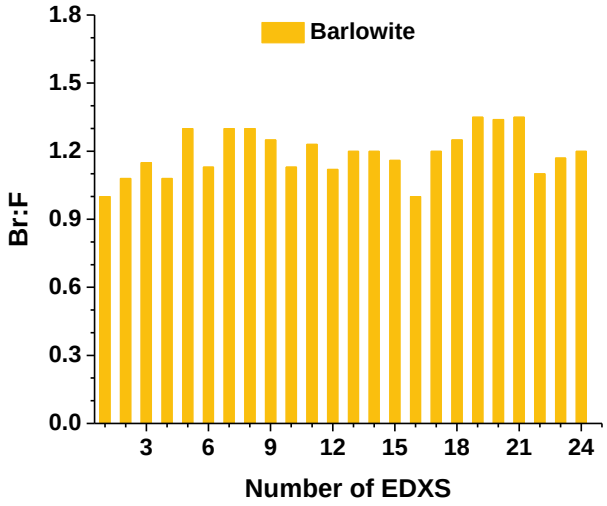

Appendix 3.4. *EDXS analysis for pristine barlowite.*

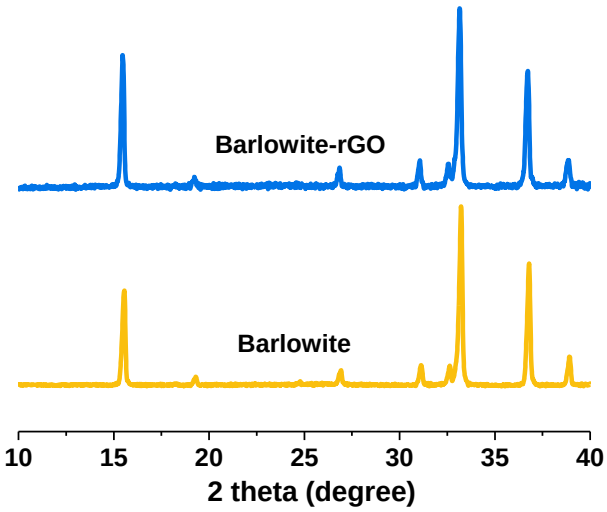

Appendix 3.5. *Experimentally recorded PXRD patterns of pristine barlowite and barlowite-rGO nanocomposite.*

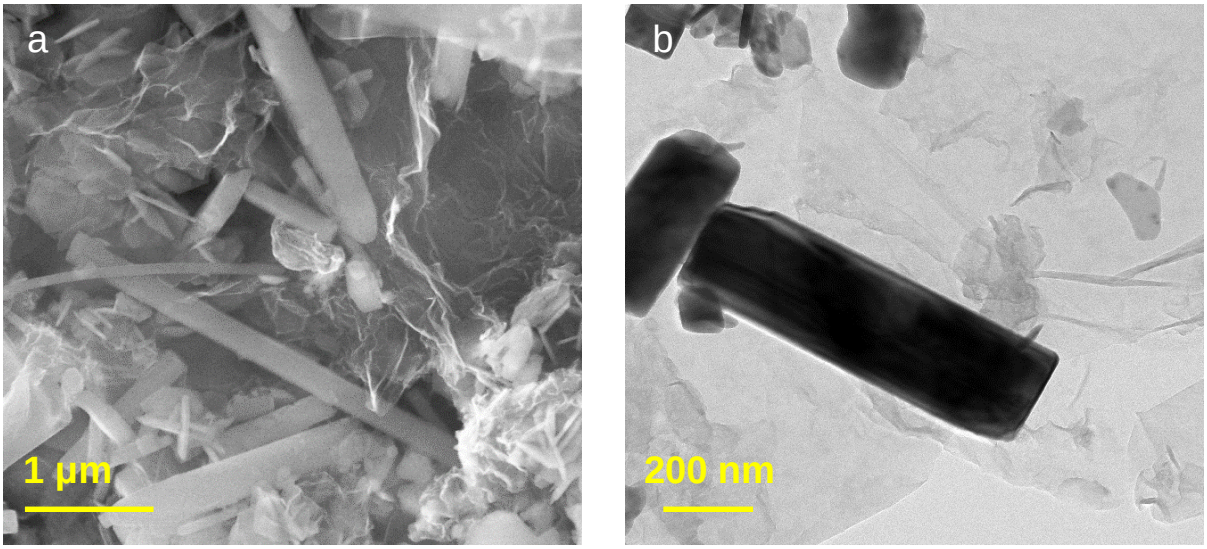

Appendix 3.6. *(a) FESEM, and (b) HRTEM images of barlowite-rGO nanocomposite depicting barlowite crystallites wrapped with rGO sheets.*

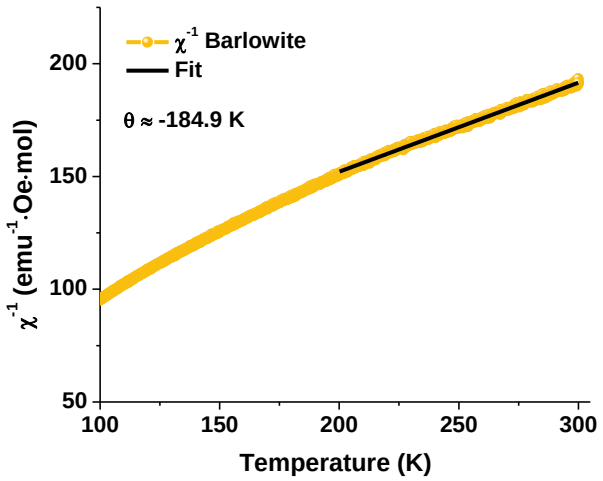

Appendix 3.7. *Inverse susceptibility plot for pristine barlowite with Curie-Weiss fit in the temperature range of 200 K – 300 K.*

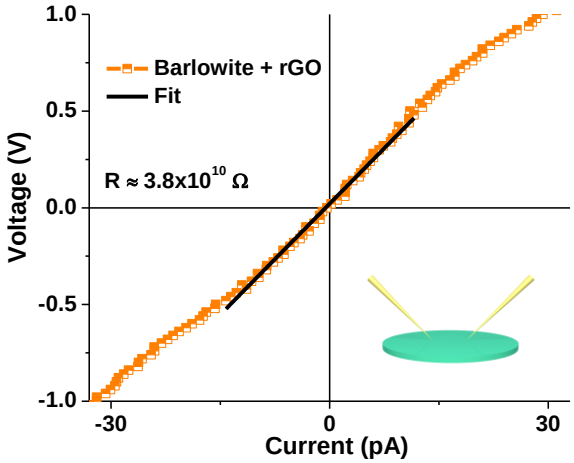

Appendix 3.8. *I-V plot of barlowite at 300 K (inset: schematic of two-probe configuration used).*

3.6 References

(1) Balents, L. Spin Liquids in Frustrated Magnets. *Nature* **2010**, *464*, 199-208.

(2) Lee, P. A. An End to the Drought of quantum Spin Liquids. *Science* **2008**, *321*, 1306-1307.

(3) Anderson, P. W. Resonating Valence Bonds: A New Kind of Insulator? *Mater. Res. Bull.* **1973**, *8*, 153-160.

(4) Broholm, C.; Cava, R.; Kivelson, S.; Nocera, D.; Norman, M.; Senthil, T. Quantum Spin Liquids. *Science* **2020**, *367*, eaay0668.

(5) Motrunich, O. I. Variational Study of Triangular Lattice Spin-1⁄2 Model with Ring Exchanges and Spin Liquid State in κ−$(ET)_2Cu_2(CN)_3$. *Phys. Rev. B* **2005**, *72*, 045105.

(6) Shores, M. P.; Nytko, E. A.; Bartlett, B. M.; Nocera, D. G. A Structurally Perfect S=1/2 Kagome Antiferromagnet. *J. Am. Chem. Soc.* **2005**, *127*, 13462-13463.

(7) Smaha, R. W.; He, W.; Jiang, J. M.; Wen, J.; Jiang, Y.-F.; Sheckelton, J. P.; Titus, C. J.; Wang, S. G.; Chen, Y.-S.; Teat, S. J. Materializing Rival Ground States in the Barlowite Family of Kagome Magnets: Quantum Spin Liquid, Spin Ordered, and Valence Bond Crystal States. *npj Quantum Mater*, **2020**, *5*, 1-11.

(8) Paddison, J. A.; Daum, M.; Dun, Z.; Ehlers, G.; Liu, Y.; Stone, M. B.; Zhou, H.; Mourigal, M. Continuous Excitations of the Triangular-Lattice Quantum Spin Liquid $YbMgGaO_4$. *Nat. Phys.* **2017**, *13*, 117-122.

(9) Itou, T.; Oyamada, A.; Maegawa, S.; Tamura, M.; Kato, R. Quantum Spin Liquid in the Spin-1⁄2 Triangular Antiferromagnet $EtMe_3Sb[Pd(dmit)_2]_2$. *Phys. Rev. B* **2008**, *77*, 104413.

(10) Okamoto, Y.; Nohara, M.; Aruga-Katori, H.; Takagi, H. Spin-Liquid State in the S= 1/2 Hyperkagome Antiferromagnet $Na_4Ir_3O_8$. *Phys. Rev. Lett.* **2007**, *99*, 137207.

(11) Norman, M. Colloquium: Herbertsmithite and the Search for the Quantum Spin Liquid. *Rev. Mod. Phys.* **2016**, *88*, 041002.

(12) Zheng, X.; Kawae, T.; Kashitani, Y.; Li, C.; Tateiwa, N.; Takeda, K.; Yamada, H.; Xu, C.; Ren, Y. Unconventional Magnetic Transitions in the Mineral Clinoatacamite $Cu_2Cl(OH)_3$. *Phys. Rev. B* **2005**, *71*, 052409.

(13) Mendels, P.; Bert, F.; De Vries, M.; Olariu, A.; Harrison, A.; Duc, F.; Trombe, J.; Lord, J.; Amato, A.; Baines, C. Quantum Magnetism in the Paratacamite Family: Towards an Ideal Kagomé Lattice. *Phys. Rev. Lett.* **2007**, *98*, 077204.

(14) Freedman, D. E.; Han, T. H.; Prodi, A.; Müller, P.; Huang, Q.-Z.; Chen, Y.-S.; Webb, S. M.; Lee, Y. S.; McQueen, T. M.; Nocera, D. G. Site Specific X-Ray Anomalous Dispersion of the Geometrically Frustrated Kagomé Magnet, Herbertsmithite, $ZnCu_3(OH)_6Cl_2$. *J. Am. Chem. Soc.* **2010**, *132*, 16185-16190.

(15) Huheey, J. E.; Keiter, E. A.; Keiter, R. L.; Medhi, O. K. *Inorganic chemistry: principles of structure and reactivity*. Pearson Education India: 2006.

(16) Han, T.-H.; Singleton, J.; Schlueter, J. A. Barlowite: A Spin-1/2 Antiferromagnet with a Geometrically Perfect Kagome Motif. *Phys. Rev. Lett.* **2014**, *113*, 227203.

(17) Pasco, C.; Trump, B.; Tran, T. T.; Kelly, Z.; Hoffmann, C.; Heinmaa, I.; Stern, R.; McQueen, T. Single-Crystal Growth of $Cu_4(OH)_6BrF$ and Universal Behavior in Quantum Spin Liquid Candidates Synthetic Barlowite and Herbertsmithite. *Phys. Rev. Mater.* **2018**, *2*, 044406.

(18) Elliott, P.; Cooper, M. A.; Pring, A. Barlowite, $Cu_4FBr(OH)_6$, a New Mineral Isotructural with Claringbullite: Description and Crystal Structure. *Mineralogical Mag.* **2014**, *78*, 1755-1762.

(19) Feng, Z.; Wei, Y.; Liu, R.; Yan, D.; Wang, Y.-C.; Luo, J.; Senyshyn, A.; dela Cruz, C.; Yi, W.; Mei, J.-W. Effect of Zn Doping on the Antiferromagnetism in Kagome $Cu_{4-x}Zn_x(OH)_6FBr$. *Phys. Rev. B* **2018**, *98*, 155127.

(20) Smaha, R. W.; He, W.; Sheckelton, J. P.; Wen, J.; Lee, Y. S. Synthesis-Dependent Properties of Barlowite and Zn-Substituted Barlowite. *J. Solid State Chem.* **2018**, *268*, 123-129.

(21) Han, T.; Helton, J.; Chu, S.; Prodi, A.; Singh, D.; Mazzoli, C.; Müller, P.; Nocera, D.; Lee, Y. S. Synthesis and Characterization of Single Crystals of the Spin-1/2 Kagome-Lattice Antiferromagnets $Zn_xCu_{4-x}(OH)_6Cl_2$. *Phys. Rev. B* **2011**, *83*, 100402.

(22) Chu, S.; Müller, P.; Nocera, D. G.; Lee, Y. S. Hydrothermal growth of single crystals of the quantum magnets: Clinoatacamite, Paratacamite, and Herbertsmithite. *Appl. Phys. Lett.* **2011**, *98*, 092508.

(23) Zheng, X.; Yamashita, T.; Hagihala, M.; Fujihala, M.; Kawae, T. Magnetic Transitions in Botallackite-Structure $Cu_2(OH)_3Br$ and $Cu_2(OH)_3I$. *Phys. B: Condens. Matter* **2009**, *404*, 680-682.

(24) Gupta, K.; Jha, P. K.; Dadwal, A.; Debnath, A. K.; Jaiswal, I.; Rana, S.; Joy, P. A.; Ballav, N. Embedding S= 1/2 Kagome-like Lattice in Reduced Graphene Oxide. *J. Phys. Chem. Lett.* **2019**, *10*, 2663-2668.

(25) Gupta, K.; Dadwal, A.; Jha, P. K.; Jain, A.; Yusuf, S.; Joy, P. A.; Ballav, N. Exploring Magnetic *XY* Behavior in a Quasi-2D Anisotropic Triangular Lattice of Cu (II) by Functionalized Graphene. *Inorg. Chem.* **2020**, *59*, 6214.

(26) Jha, P. K.; Singh, S. K.; Kumar, V.; Rana, S.; Kurungot, S.; Ballav, N. High-Level Supercapacitive Performance of Chemically Reduced Graphene Oxide. *Chem* **2017**, *3*, 846-860.

(27) Chukanov, N. V.; Chervonnyi, A. D. *Infrared Spectroscopy of Minerals and Related Compounds*. Springer: **2016**.

(28) Goodenough, J. B. *Magnetism and Chemical Bond*. Interscience Publ.: **1963**; Vol. 1.

(29) Henderson, A.; Dong, L.; Biswas, S.; Revell, H. I.; Xin, Y.; Valenti, R.; Schlueter, J. A.; Siegrist, T. Order–Disorder Transition in the S = 1/2 Kagome Antiferromagnets Claringbullite and Barlowite. *Chem. Commun.* **2019**, *55*, 11587-11590.

Chapter 4

Paratacamite – 2D S=1/2 Spin Kagome Lattice onto Reduced Graphene Oxide

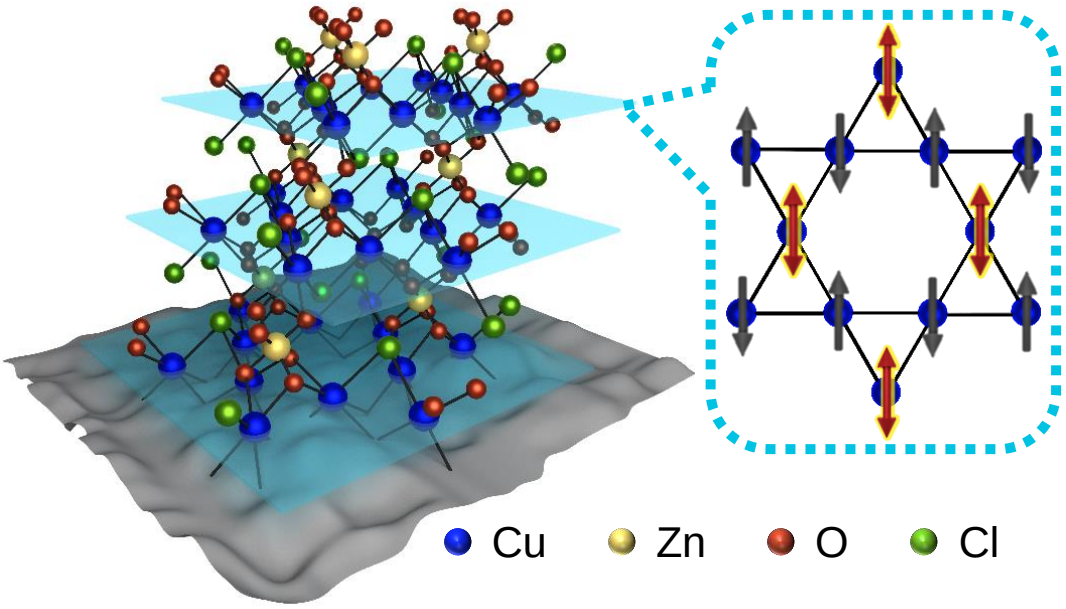

4.1 Introduction

Quantum spin liquid (QSL) is a long-predicted spin state possessing strong quantum spin fluctuations suppressing the spin freezing down to the lowest measured temperature.[1] The interest in QSLs and the experimental search saw an up rise when P. W. Anderson proposed a resonating valence bond (RVB) in a triangular spin lattice as a QSL state. It was further invoked when RVB spin liquid was related to the Cooper pairs in oxide-based superconductor.[2-4] Such a spin state is usually anticipated from low dimensional and/or geometrically frustrated lattices (kagome-lattice) with odd number of active spins in the unit cell to subdue an otherwise energetically favourable Néel ground state.[2] Thus, in search of elusive QSL state, highly-frustrated magnetic systems were explored, in particular, herbertsmithite [$Cu_3Zn(OH)_6Cl_2$] with structurally perfect S=1/2 kagome lattice. Even, striking evidence of QSL features on herbertsmithite were provided by neutron scattering measurements.[5, 6]

Herbertsmithite consists of kagome spin lattice – a corner-shared triangular lattice comprised of $M(OH)_3$ triangles, where M is the spin bearing metal ion (Figure 4.1).[7] Based on the O-M-O bond angle in kagome lattice, spins have a tendency to align antiferromagnetically; however, they are restricted by the geometry of lattice.[7, 8] Though, materials exhibiting such hydroxide based kagome planes include jarosites as well as atacamites, S=1/2 kagome planes were present only in the family of atacamites [$Cu_{4-x}M_x(OH)_6X_2$] where M=Zn, Cu, Co, Ni and X=Cl, Br, I.[9-11]

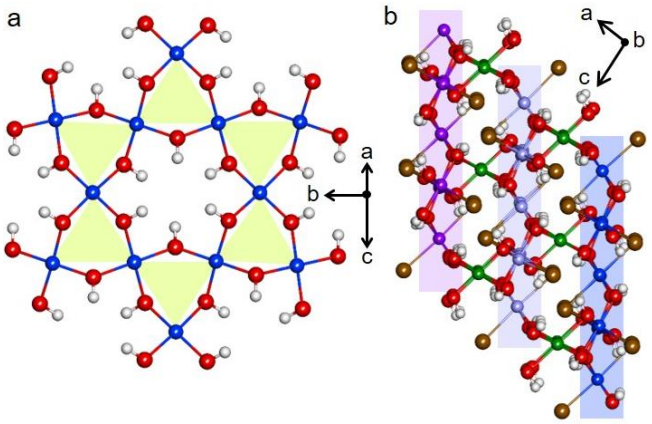

Figure 4.1. *(a) Top-view of Cu(II)-based kagome plane, and (b) side-view to visualize the ABC stacking of kagome planes in herbertsmithite. (Color code: blue, mauve, purple-Cu in three consecutive kagome planes; green-interlayer Cu; red-O; brown-Cl, and white-H).*

One of the end members of atacamite family, herbertsmithite, possesses Cu(II)-based kagome planes separated via diamagnetic Zn(II) ions in the interlayer site.[6, 12] Since the ionic radii and

coordination environment of Cu(II) and Zn(II) is comparable,[13] there is a possibility of anti-site disorder; however, recent site-specific X-ray scattering studies done on herbertsmithite revealed an excess of Cu(II) ions with 15% occupancy in the interlayer site while no Zn(II) ions were observed in the kagome plane.[14] Even with the slight excess of Cu(II) ions in the interlayer site, herbertsmithite shows no magnetic order down to 50 mK and is known to exhibit QSL features.[10, 15] However, synthesizing phase-pure herbertsmithite without involving hydrothermal conditions (autoclave vessels and/or tube furnace) remained difficult.[7, 10, 14, 16-34]

4.2 Materials and Methods

Graphite flake (+100 mesh), potassium permanganate ($KMnO_4$), hydrogen peroxide (H_2O_2), copper chloride (CuCl) and zinc chloride ($ZnCl_2$) were used as received from Sigma-Aldrich. Sodium hydroxide (NaOH) was purchased from Vetec. Sulfuric acid (H_2SO_4) and methanol (MeOH) were purchased from RANKEM (India). Millipore water (MQ, ~18.2 MΩ·cm) was used wherever required. Graphene Oxide (GO) was synthesized and duly characterized following our previous report.[35] Further, GO was centrifuged at 1000 rpm to remove the multilayers, if any.

Synthesis of H-rGO: In a flask, aqueous dispersion (100 mL) of CuCl (~445 mg, ~4.5 mmol), $ZnCl_2$ (~200 mg, ~0.67 mmol) and NaOH (~216 mg, ~5.4 mmol) was added, followed by 100 mL aqueous dispersion of GO (~1 mg/mL). Reaction mixture was then stirred at ~94 °C for 24 h and the precipitate (H-rGO) was filtered and washed with MQ H_2O and MeOH. H-rGO was vacuum dried before further characterization and experiments.

Synthesis of P-rGO: Reaction conditions were similar to H-rGO except the amount of reactants as follows; CuCl (~445 mg, ~4.5 mmol), $ZnCl_2$ (~402 mg, ~1.3 mmol) and NaOH (~162 mg, ~4 mmol).

Synthesis of pristine H: In a flask, aqueous dispersion (200 mL) of CuCl (~445.5 mg, ~4.5 mmol), $ZnCl_2$ (~300 mg, ~1 mmol), and NaOH (~180 mg, ~4.5 mmol) was stirred at ~94 °C for 24 h. The precipitate formed was filtered and washed with MQ H_2O and MeOH followed by vacuum drying before further characterization. The final product was light blue in color.

Synthesis of pristine P: Reaction conditions were similar to the synthesis of herbertsmithite except the amount of reactants as follows; CuCl (~445mg, ~4.5 mmol), $ZnCl_2$ (~200 mg, ~0.67 mmol), and NaOH (~163 mg, ~4 mmol). The final product was light green in color.

Magnetic response for all the samples was recorded on SQUID vibrating sample magnetometer (Quantum Design). Magnetization was recorded in field-cooled (FC) mode by cooling the sample in 50 Oe applied magnetic field and recording magnetization in 50 Oe applied field while warming. Zero-field-cooled (ZFC) magnetization was recorded after cooling the sample in zero field and recording the magnetization in 50 Oe while warming. Raman spectroscopy was done on powdered samples using a 632.8 nm laser on Horiba Jobin Yvon Raman microscope with 50X objective lens. PXRD patterns were recorded on Bruker D8 Advance diffractometer with Cu Kα radiation (λ = 1.5406 Å); 2θ range of 30−45°. FESEM images were taken under a Zeiss Ultra Plus scanning electron microscope by drop casting the methanolic dispersion of samples on Si wafer. Four-probe dc electrical conductivity (I−V) measurements were done on a conventional Keithley 6221 setup. Two-probe dc electrical conductivity (I−V) measurements were done on a Keithley 4200 SCS Parameter Analyzer system equipped with an Everbeing probe station. Seebeck coefficient measurements were done on Linses LSR-3.

4.3 Results and Discussion

Herein, we have employed an elegantly simple chemistry to synthesize phase-pure herbertsmithite, at close-to-ambient conditions for the first time (see the Materials and Methods for details). Slight alternation in the stoichiometry of chemical precursors also enabled us to successfully isolate structural analogue of herbertsmithite, i.e., paratacamite with the characteristic magnetic property.[6] Both herbertsmithite and paratacamite possess Cu(II)-based kagome planes, the difference lies in the occupancy of interlayer site between the two kagome planes with >33% Zn(II) occupancy in paratacamite while 100% Zn(II) occupancy for herbertsmithite (Figure 4.1).[6]

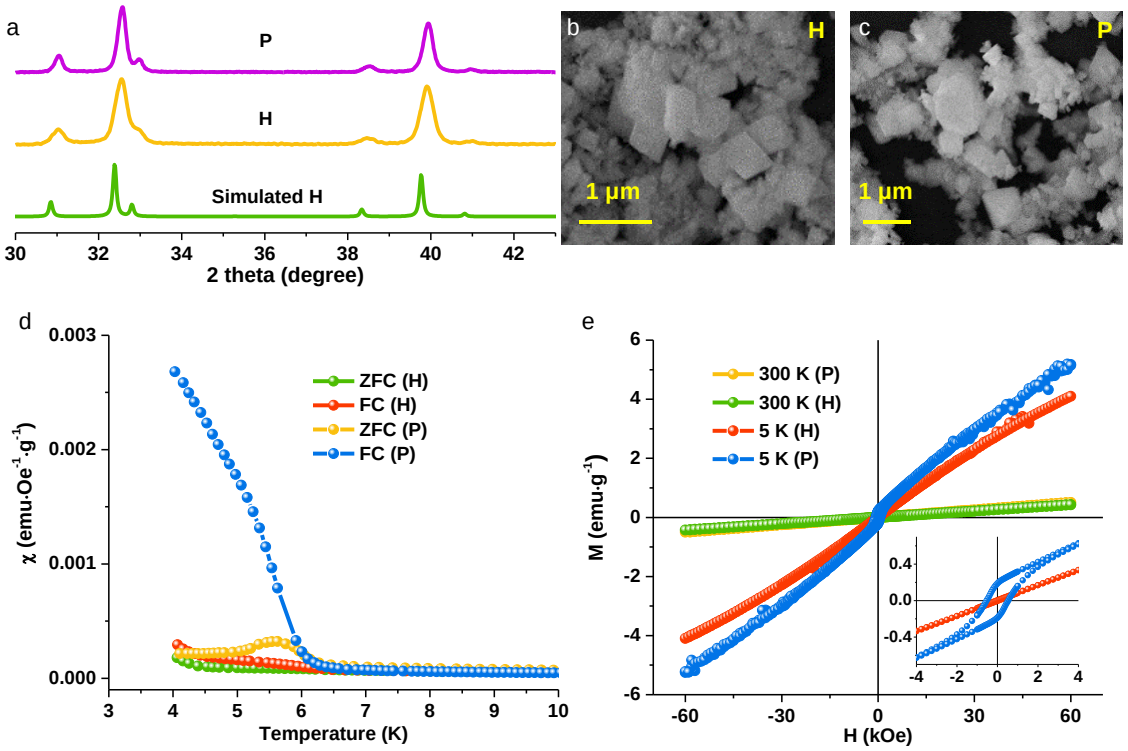

Figure 4.2. *(a) PXRD patterns, (b-c) FESEM images, (d) magnetic susceptibility, and (e) M-H plots of herbertsmithite (H), and paratacamite (P).*

H and P solids were characterized by powder X-ray diffraction (PXRD) and the clean patterns show fingerprint peaks at $2\theta \approx 32.5°$ (doublet) and $2\theta \approx 40°$ (singlet) confirming the presence of crystalline and phase-pure H and P (Figure 4.2a).[16] The Raman spectra exhibited strong bands at ~122 cm^{-1} and ~147 cm^{-1} (OCuO bending), ~365 cm^{-1} (CuCl stretching), and ~502 cm^{-1} corresponding to CuO stretching in P (Appendix 4.1).[36] Weaker bands at ~276 cm^{-1} (lattice mode), and ~942 cm^{-1} corresponding to hydroxyl deformation were also present, supporting the successful formation of both H and P (Appendix 4.1).[36] Field-emission scanning electron microscopy (FESEM) images of H and P reveal micro- and nano-crystallites with sharp-edges and morphological features were indistinctive (Figure 4.2b and c). Energy dispersive X-ray spectroscopy (EDXS) was used to determine the stoichiometric ratios of Cu and Zn in the final products and our extensive EDXS analysis suggested the formula units to be $[Cu_3Zn(OH)_6Cl_2]$ for H and $[Cu_3Cu_{0.3}Zn_{0.7}(OH)_6Cl_2]$ for P (Appendix 4.2).

Magnetic responses of H and P were recorded in field-cooled (FC) and zero field-cooled (ZFC) modes at an externally applied magnetic field of 50 Oe. The kagome planes in H are magnetically isolated by diamagnetic Zn(II) ions in between and hence no long-range magnetic order is observed down to 4 K (Figure 4.2d). However, due to a combination of Cu(II) ions and

Zn(II) ions at the interlayer site of P, an additional linkage Cu_{kag}-O-Cu_{inter} is present with an angle of ~97° (Cu_{kag} – Cu in kagome plane, Cu_{inter} – Cu in interlayer site) which could allow ferromagnetic exchange interaction between two consecutive kagome planes as suggested by Goodenough-Kanamori-Anderson (GKA) rules.[7, 8] In fact, for P, sharp increase in the magnetization, in comparison to H, could be due to ferromagnetic-like order below ~5.5 K (Figure 4.2d).

The inverse susceptibility plots were fitted with Curie-Weiss equation, $\chi=C/(T-\theta_{CW})$ in the range of 200 K to 300 K for both H and P (Appendix 4.3). Weiss temperature (θ_{CW}) was estimated to be -207.8 K and -247.5 K for H and P, respectively, indicating a strong antiferromagnetic interaction between the spins.[8] The suggested antiferromagnetic interaction between the spins is suppressed and is not observed experimentally due to high spin frustration prevailing in the lattice, also supported by the value of frustration factor *f* (= $|\theta_{CW}|/T_{Cr}$), ~37.8 and ~45.0 for H and P, respectively. Notably, H and P powder samples obtained previously by hydrothermal methods and our powder H and P samples consistently show $\theta_{CW} > 200$ K viz. *f* values beyond 35. Magnetization of H and P as a function of externally applied field were recorded (Figure 4.2e). At 300 K, M-H curves characteristic of a paramagnet were observed for both H and P. In the case of H, at 5 K, no coercive field (H_C) and/or saturation of magnetization even at 60 kOe suggested no long-range magnetic order (Figure 4.2e). For P, at 5 K, a coercive field of, $H_C \approx 570$ Oe along with no saturation magnetization beyond 60 kOe was indicative of ferromagnetic-like interactions in the lattice below 5.5 K (Figure 4.2e).

As for the H-rGO and P-rGO systems, PXRD patterns revealed characteristic peaks at $2\theta \approx 32.5°$ and $2\theta \approx 40°$, confirming the presence of phase-pure H and P (Figure 4.3a).[16] The Raman spectra of H-rGO and P-rGO exhibited strong bands at ~122 cm^{-1}, ~147 cm^{-1}, ~365 cm^{-1}, and ~502 cm^{-1} along with weaker bands at ~276 cm^{-1}, and ~942 cm^{-1}, likewise pristine H and P (Appendix 4.1).[36] Further, FESEM images of both H-rGO and P-rGO systems depicted extensive wrapping of the crystallites of H and P with rGO sheets consistently (Figure 4.3b and c). A thorough EDXS analysis was carried out to determine the Cu:Zn ratio and values of $x \approx 1$ and $x \approx 0.6$ were estimated for the H-rGO and P-rGO systems, respectively (Appendix 4.2).

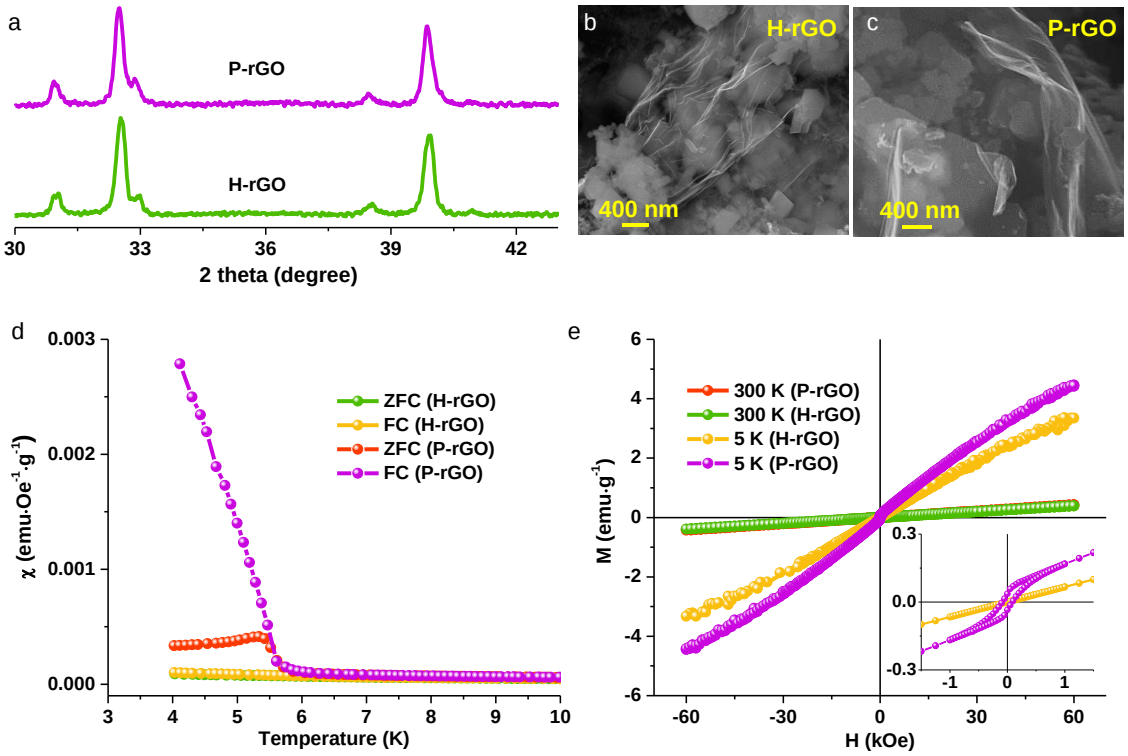

Figure 4.3. *(a) PXRD patterns, and (b-c) FESEM images, (d) magnetic susceptibility, and (e) M-H plots of H-rGO and P-rGO.*

The dc magnetic susceptibility of H-rGO and P-rGO systems were investigated as a function of temperature at an externally applied field of 50 Oe, in FC and ZFC modes. The inverse susceptibility plots were fitted with the Curie-Weiss equation in the range of 200 K to 300 K for both H-rGO and P-rGO, and θ_{CW} were estimated to be -217.4 K and -265.7 K, respectively, indicating strong antiferromagnetic interaction between the spins (Appendix 4.3).[8] Also, the value of frustration factor *f* was calculated to be ~39.5 and ~48.3 for H-rGO and P-rGO, respectively suggesting the presence of strong spin frustration in both the systems. Likewise pristine H and P, long-range order in H-rGO as well as P-rGO was strongly suppressed by the high spin frustration stemming from geometry of the kagome-lattice. In fact, no long-range magnetic order was observed for the H-rGO system till 4 K (ZFC and FC plots looked alike) ascribed to the magnetically isolated kagome planes in the lattice of H (Figure 4.3d). For P-rGO, in view of the combination Cu(II) and Zn(II) ions at the interlayer sites of P, a ferromagnetic-like transition was consistently observed at ~5.5 K with no shift in the T_{Cr} value compared to pristine P (Figure 4.3d).

M-H curves of both H-rGO and P-rGO revealed paramagnetic behavior at 300 K (Figure 4.3e). For H-rGO, no saturation of magnetization as well as no coercive field (H_C) was observed

supporting the absence of long-range magnetic order at 5 K (Figure 4.3e). M-H curve corresponding to P-rGO exhibited unsaturated magnetic moments even at an applied field of 60 kOe, characteristic of frustrated spins, along with a coercive field of, $H_C \approx 90$ Oe at 5 K, owing to the ferromagnetic-like coupling between the kagome planes (Figure 4.3e). Overall, characteristic magnetic signatures of pristine H and P were successfully retained in the H-rGO and P-rGO, respectively.

Since H and P are expected to be electrically insulating and we have subsequently blended them with semiconducting rGO matrix, electrical transport measurements were carried out for the H-rGO and P-rGO systems using conventional four-probe method in pelletize configuration. In fact, we could not get a reasonable current-voltage characteristics for the pristine H and P pellets using the four-probe method. Therefore two-probe current-voltage measurements were explored and resistance values of ~$6.0*10^{11}$ Ω and ~$2.8*10^{13}$ Ω at 300 K for H and P, respectively were measured which suggested that these materials are indeed electrical insulators (Appendix 4.4).

Interestingly, electrical conductivity values of H-rGO and P-rGO were realized to be ~10 $S \cdot m^{-1}$ and ~55 $S \cdot m^{-1}$ at 300 K, respectively (Appendix 4.5). The electrical conductivity values of both H-rGO and P-rGO systems gradually increased upon increasing the temperature thereby indicating their semiconducting behavior and from the Arrhenius plots activation energy (E_a) values were estimated to be ~0.06 eV and ~0.05 eV for the H-rGO and P-rGO, respectively (Appendix 4.5).[37] Such small values of E_a indicates facile electrical conduction by thermally-assisted tunneling of charge carriers across grain boundaries of H or P and rGO. Further, mechanical mixtures were prepared by physically mixing pristine H and P (~90 wt%) with extracted rGO (~10 wt%) and respective resistance values of ~$8.6*10^{9}$ Ω (H+rGO) and ~$3.2*10^{10}$ Ω (P+rGO) were evaluated from the measurements done in two-probe configuration at 300 K (Appendix 4.4). The resistance values measured for the physical mixtures (H+rGO and P+rGO) were found to be similar to those obtained for the pristine H and P thereby ruling out the possibility of formation of a mechanical mixture in our H-rGO and P-rGO systems. To further investigate the electrical transport behavior, Seebeck coefficient (S) was recorded as a function of temperature where the sign of Seebeck coefficient can reveal the nature of majority charge carriers in electrical semiconductors. For the H-rGO system, negative values of Seebeck coefficient in the temperature range of 300 K – 430 K indicated the n-type semiconducting behavior with electrons being the majority charge carriers (Appendix 4.6).[38]

4.4 Conclusions

In conclusions, we have presented facile chemical synthesis of phase-pure S=1/2 kagome-lattice antiferromagnets H and P as well as their successful integration with semiconducting rGO matrix without impeding characteristic magnetic signatures. Estimated *f* values of here synthesized H and P crystalline solids were as good as H and P powders obtained from inconvenient reaction conditions and even *f* values were found to be significantly retained upon integration with rGO. H-rGO and P-rGO systems were attributed as magnetic semiconductors. We anticipate our simple chemical principles to stimulate synthesis of other Cu(II)-based QSL candidates as well as their integration with semiconducting matrixes like rGO.

4.5 Appendix

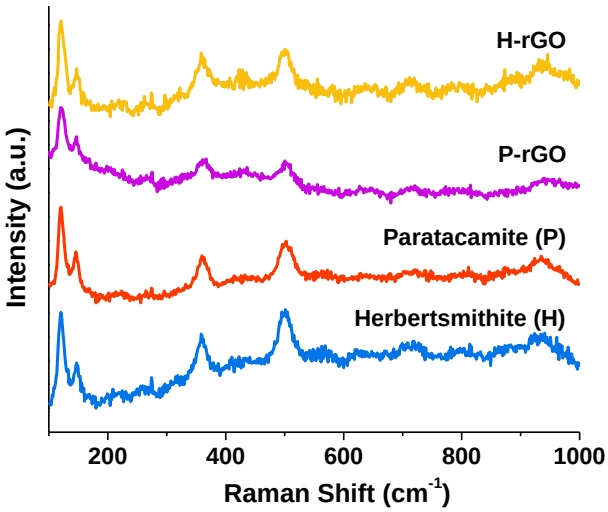

Appendix 4.1. *Raman spectra of pristine H, pristine P, H-rGO, and P-rGO.*

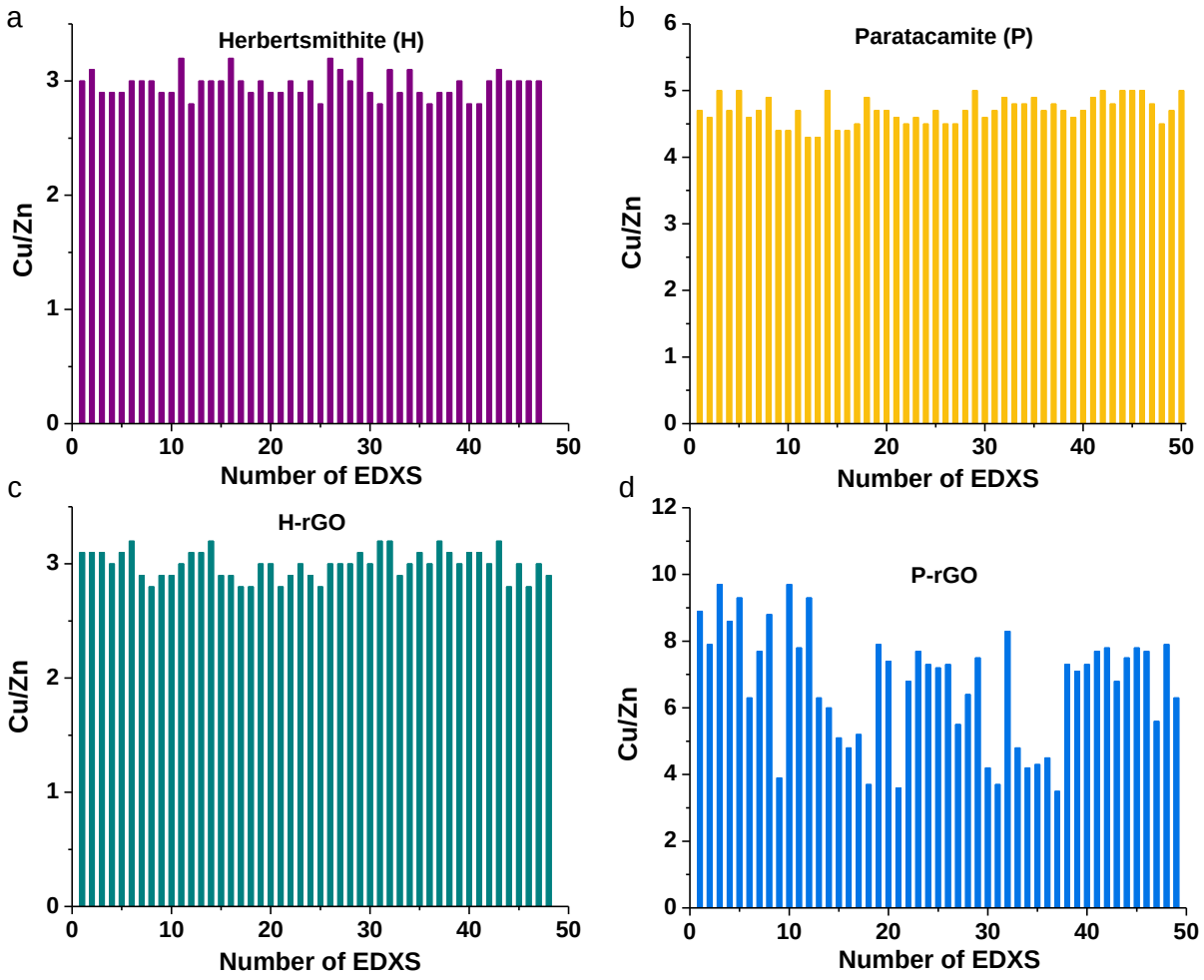

Appendix 4.2. *EDXS analysis of (a) pristine H, (b) pristine P, (c) H-rGO, and (d) P-rGO (closely matching with expected Cu:Zn ratio of 3, 4.7, 3, and 5.7, respectively).*

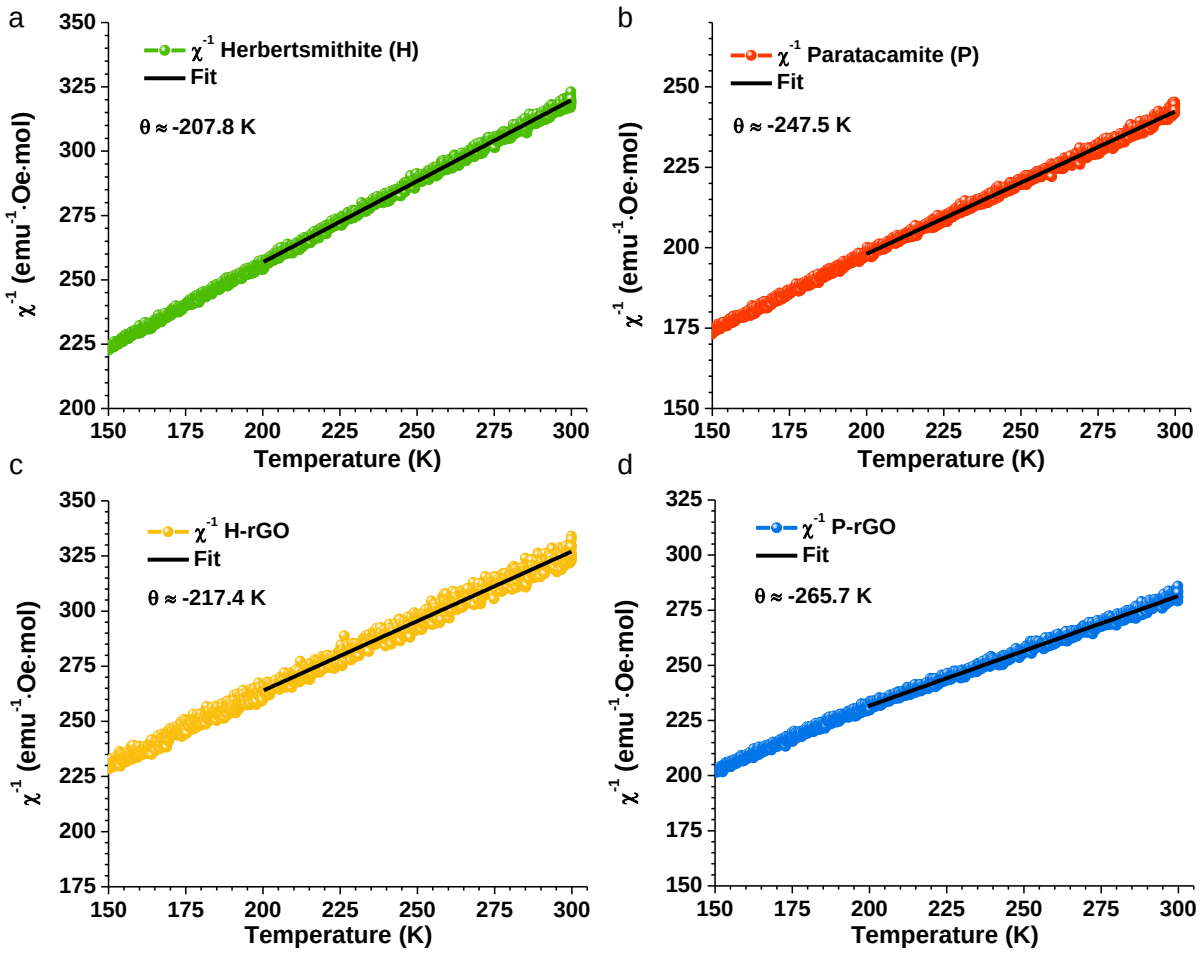

Appendix 4.3. *ZFC inverse as a function of temperature with Curie-Weiss fit in the temperature range of 200 K to 300 K for (a) pristine H, (b) pristine P, (c) H-rGO, and (d) P-rGO.*

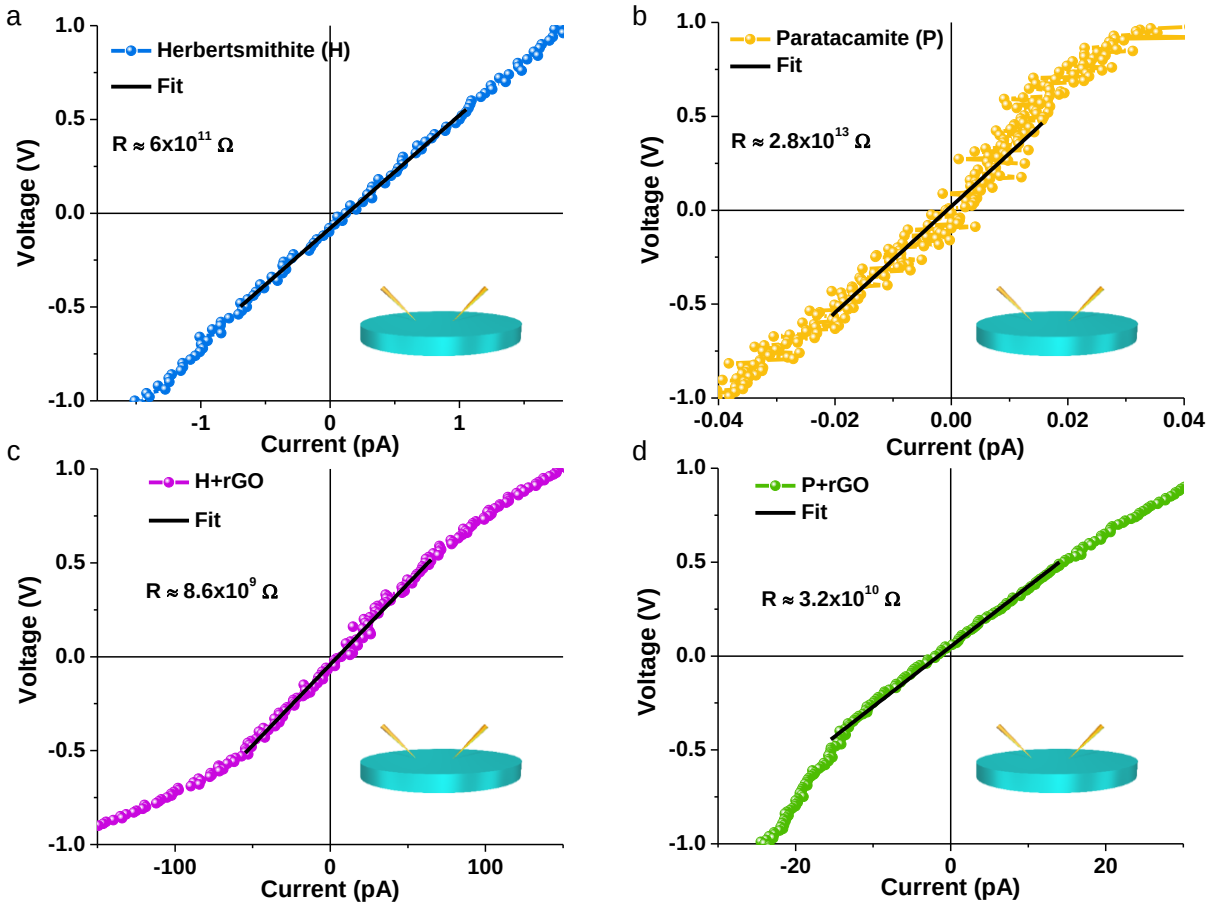

Appendix 4.4. *(a-d) I-V profiles of pristine H, pristine P, and mechanical mixtures (H+rGO and P+rGO) at 300 K (insets: schematic of 2-probe configuration).*

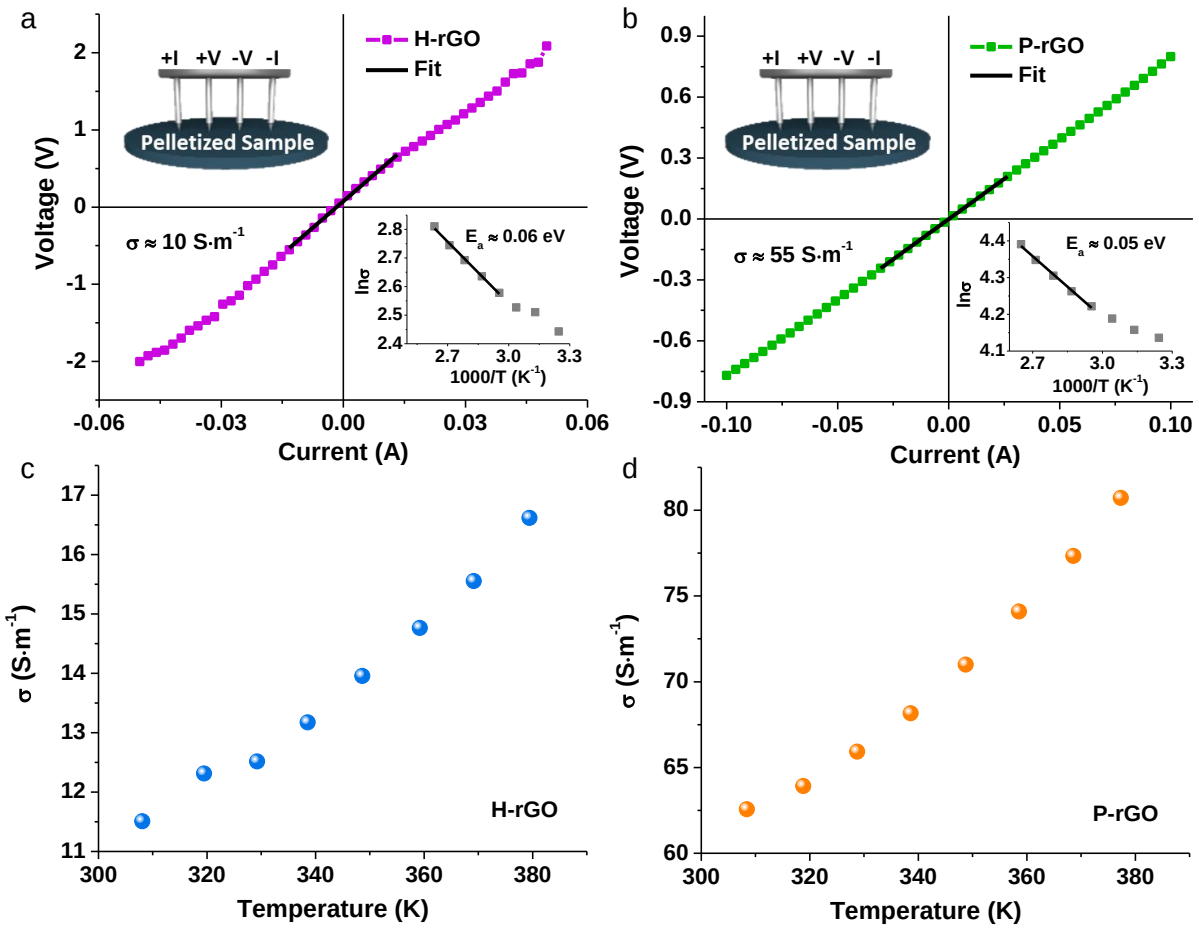

Appendix 4.5. *(a-b) I-V profiles at 300 K (insets: schematic for 4-probe configuration used, and Arrhenius plots); (c-d) electrical conductivity as a function of temperature of H-rGO, and P-rGO.*

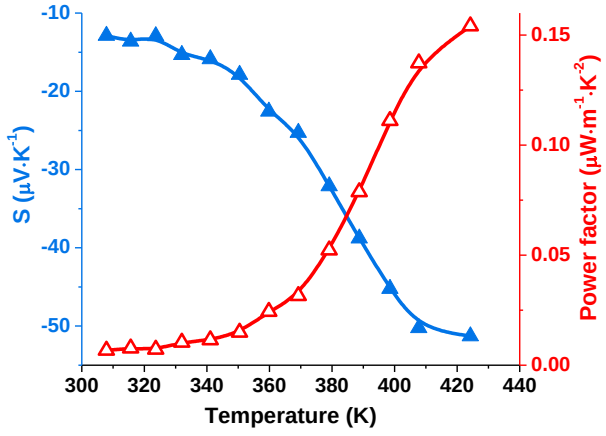

Appendix 4.6. *Seebeck coefficient (S) and power factor ($P = S^2 \cdot \sigma$) plotted against temperature for H-rGO.*

4.6 References

(1) Broholm, C.; Cava, R.; Kivelson, S.; Nocera, D.; Norman, M.; Senthil, T., Quantum Spin Liquids. *Science* **2020,** *367*, 263.

(2) Lee, P. A., An End to the Drought of Quantum Spin Liquids. *Science* **2008,** *321*, 1306-1307.

(3) Anderson, P. W., Resonating Valence Bonds: A New Kind of Insulator? *Mater. Res. Bull.* **1973,** *8*, 153-160.

(4) Anderson, P. W., The Resonating Valence Bond State in La_2CuO_4 and Superconductivity. *Science* **1987,** *235*, 1196-1198.

(5) Helton, J., et al., Spin Dynamics of the Spin-1/2 Kagome Lattice Antiferromagnet $ZnCu_3(OH)_6Cl_2$. *Phys. Rev. Lett.* **2007,** *98*, 107204.

(6) Braithwaite, R.; Mereiter, K.; Paar, W.; Clark, A., Herbertsmithite, $Cu_3Zn(OH)_6Cl_2$, a New Species, and the Definition of Paratacamite. *Mineral. Mag.* **2004,** *68*, 527-539.

(7) Shores, M. P.; Nytko, E. A.; Bartlett, B. M.; Nocera, D. G., A Structurally Perfect S= 1/2 Kagome Antiferromagnet. *J. Am. Chem. Soc.* **2005,** *127*, 13462-13463.

(8) Goodenough, J. B., *Magnetism and Chemical Bond*. Interscience Publ.: 1963; Vol. vol. 1.

(9) Nocera, D. G.; Bartlett, B. M.; Grohol, D.; Papoutsakis, D.; Shores, M. P., Spin Frustration in 2D Kagome Lattices: A Problem for Inorganic Synthetic Chemistry. *Chem. Eur. J.* **2004,** *10*, 3850-3859.

(10) Puphal, P.; Zoch, K. M.; Désor, J.; Bolte, M.; Krellner, C., Kagome Quantum Spin Systems in the Atacamite Family. *Phys. Rev. Mater.* **2018,** *2*, 063402.

(11) Colman, R. H.; Sinclair, A.; Wills, A. S., Magnetic and Crystallographic Studies of Mg-Herbertsmithite, γ-$Cu_3Mg(OH)_6Cl_2$—A New S = 1/2 Kagome Magnet and Candidate Spin Liquid. *Chem. Mater.* **2011,** *23*, 1811-1817.

(12) Norman, M., Colloquium: Herbertsmithite and the Search for the Quantum Spin Liquid. *Rev. Mod. Phys.* **2016,** *88*, 041002.

(13) Huheey, J. E.; Keiter, E. A.; Keiter, R. L.; Medhi, O. K., *Inorganic Chemistry: Principles of Structure and Reactivity*. Pearson Education India: 2006.

(14) Freedman, D. E., et al., Site Specific X-ray Anomalous Dispersion of the Geometrically Frustrated Kagomé Magnet, Herbertsmithite, $ZnCu_3(OH)_6Cl_2$. *J. Am. Chem. Soc.* **2010,** *132*, 16185-16190.

(15) Mendels, P.; Bert, F., Quantum Kagome Frustrated Antiferromagnets: One Route to Quantum Spin Liquids. *Compt. Rend. Phys.* **2016,** *17*, 455-470.

(16) Chu, S.; Müller, P.; Nocera, D. G.; Lee, Y. S., Hydrothermal Growth of Single Crystals of the Quantum Magnets: Clinoatacamite, Paratacamite, and Herbertsmithite. *Appl. Phys. Lett.* **2011,** *98*, 092508.

(17) Pozo, G.; de la Presa, P.; Prato, R.; Morales, I.; Marin, P.; Fransaer, J.; Dominguez-Benetton, X., Spin Transition Nanoparticles made Electrochemically. *Nanoscale* **2020,** *12*, 5412-5421.

(18) Velázquez, M.; Bert, F.; Mendels, P.; Denux, D.; Veber, P.; Lahaye, M.; Labrugère, C., Aqueous Solution Growth at 200° C and Characterizations of pure, ^{17}O-or D-based Herbertsmithite $Zn_xCu_{4-x}(OH)_6Cl_2$ Single Crystals. *J. Cryst. Growth* **2020,** *531*, 125372.

(19) Khuntia, P., et al., Gapless Ground State in the Archetypal Quantum Kagome Antiferromagnet $ZnCu_3(OH)_6Cl_2$. *Nat. Phys.* **2020**, 1-6.

(20) Pustogow, A.; Li, Y.; Voloshenko, I.; Puphal, P.; Krellner, C.; Mazin, I. I.; Dressel, M.; Valentí, R., Nature of Optical Excitations in the Frustrated Kagome Compound Herbertsmithite. *Phys. Rev. B* **2017,** *96*, 241114.

(21) Sushkov, A. B.; Jenkins, G. S.; Han, T.-H.; Lee, Y. S.; Drew, H. D., Infrared Phonons as a Probe of Spin-Liquid States in Herbertsmithite $ZnCu_3(OH)_6Cl_2$. *J. Phys.: Condens. Matter* **2017,** *29*, 095802.

(22) Zorko, A.; Herak, M.; Gomilšek, M.; van Tol, J.; Velázquez, M.; Khuntia, P.; Bert, F.; Mendels, P., Symmetry Reduction in the Quantum Kagome Antiferromagnet Herbertsmithite. *Phys. Rev. Lett.* **2017,** *118*, 017202.

(23) Kelly, Z.; Gallagher, M.; McQueen, T., Electron Doping a Kagome Spin Liquid. *Phys. Rev. X* **2016,** *6*, 041007.

(24) Han, T.-H.; Norman, M.; Wen, J.-J.; Rodriguez-Rivera, J. A.; Helton, J. S.; Broholm, C.; Lee, Y. S., Correlated Impurities and Intrinsic Spin-Liquid Physics in the Kagome Material Herbertsmithite. *Phys. Rev. B* **2016,** *94*, 060409.

(25) Fu, M.; Imai, T.; Han, T.-H.; Lee, Y. S., Evidence for a Gapped Spin-Liquid Ground State in a Kagome Heisenberg Antiferromagnet. *Science* **2015,** *350*, 655-658.

(26) Asaba, T.; Han, T.-H.; Lawson, B.; Yu, F.; Tinsman, C.; Xiang, Z.; Li, G.; Lee, Y. S.; Li, L., High-Field Magnetic Ground State in S = 1/2 Kagome Lattice Antiferromagnet $ZnCu_3(OH)_6Cl_2$. *Phys. Rev. B* **2014,** *90*, 064417.

(27) Nilsen, G.; De Vries, M.; Stewart, J.; Harrison, A.; Rønnow, H., Low-Energy Spin Dynamics of the S = 1/2 Kagome System Herbertsmithite. *J. Phys.: Condens. Matter* **2013,** *25*, 106001.

(28) Han, T.-H.; Helton, J. S.; Chu, S.; Nocera, D. G.; Rodriguez-Rivera, J. A.; Broholm, C.; Lee, Y. S., Fractionalized Excitations in the Spin-Liquid State of a Kagome-Lattice Antiferromagnet. *Nature* **2012,** *492*, 406-410.

(29) Kozlenko, D.; Kusmartseva, A. F.; Lukin, E.; Keen, D.; Marshall, W.; De Vries, M.; Kamenev, K. V., From Quantum Disorder to Magnetic Order in an S = 1/2 Kagome Lattice: A Structural and Magnetic Study of Herbertsmithite at High Pressure. *Phys. Rev. Lett.* **2012,** *108*, 187207.

(30) de Vries, M.; Wulferding, D.; Lemmens, P.; Lord, J.; Harrison, A.; Bonville, P.; Bert, F.; Mendels, P., Extension of the Zinc Paratacamite Phase Diagram: Probing the Effect of Spin Vacancies in an S = 1/2 Kagome Antiferromagnet. *Phys. Rev. B* **2012,** *85*, 014422.

(31) Shaginyan, V.; Msezane, A.; Popov, K., Thermodynamic Properties of the Kagome Lattice in Herbertsmithite. *Phys. Rev. B* **2011,** *84*, 060401.

(32) Han, T.; Helton, J.; Chu, S.; Prodi, A.; Singh, D.; Mazzoli, C.; Müller, P.; Nocera, D.; Lee, Y. S., Synthesis and Characterization of Single Crystals of the Spin-1/2 Kagome-Lattice Antiferromagnets $Zn_xCu_{4-x}(OH)_6Cl_2$. *Phys. Rev. B* **2011,** *83*, 100402.

(33) Wulferding, D.; Lemmens, P.; Scheib, P.; Röder, J.; Mendels, P.; Chu, S.; Han, T.; Lee, Y. S., Interplay of Thermal and Quantum Spin Fluctuations in the Kagome Lattice Compound Herbertsmithite. *Phys. Rev. B* **2010,** *82*, 144412.

(34) Bert, F.; Nakamae, S.; Ladieu, F.; L'hôte, D.; Bonville, P.; Duc, F.; Trombe, J.-C.; Mendels, P., Low Temperature Magnetization of the S = 1/2 Kagome Antiferromagnet $ZnCu_3(OH)_6Cl_2$. *Phys. Rev. B* **2007,** *76*, 132411.

(35) Jha, P. K.; Singh, S. K.; Kumar, V.; Rana, S.; Kurungot, S.; Ballav, N. High-Level Supercapacitive Performance of Chemically Reduced Graphene Oxide. *Chem* **2017**, *3*, 846-860.

(36) Frost, R. L.; Martens, W.; Kloprogge, J. T.; Williams, P. A., Raman Spectroscopy of the Basic Copper Chloride Minerals Atacamite and Paratacamite: Implications for the Study of Copper, Brass and Bronze Objects of Archaeological Significance. *J. Raman Spectrosc.* **2002,** *33*, 801-806.

(37) Dhara, B.; Nagarkar, S. S.; Kumar, J.; Kumar, V.; Jha, P. K.; Ghosh, S. K.; Nair, S.; Ballav, N., Increase in Electrical Conductivity of MOF to Billion-Fold upon Filling the Nanochannels with Conducting Polymer. *J. Phys. Chem. Lett.* **2016,** *7*, 2945-2950.

(38) Sootsman, J. R.; Chung, D. Y.; Kanatzidis, M. G., New and Old Concepts in Thermoelectric Materials. *Angew. Chem. Int. Ed.* **2009,** *48*, 8616-8639.

Chapter 5

Botallackite – 2D S=1/2 Anisotropic Triangular Lattice onto Reduced Graphene Oxide

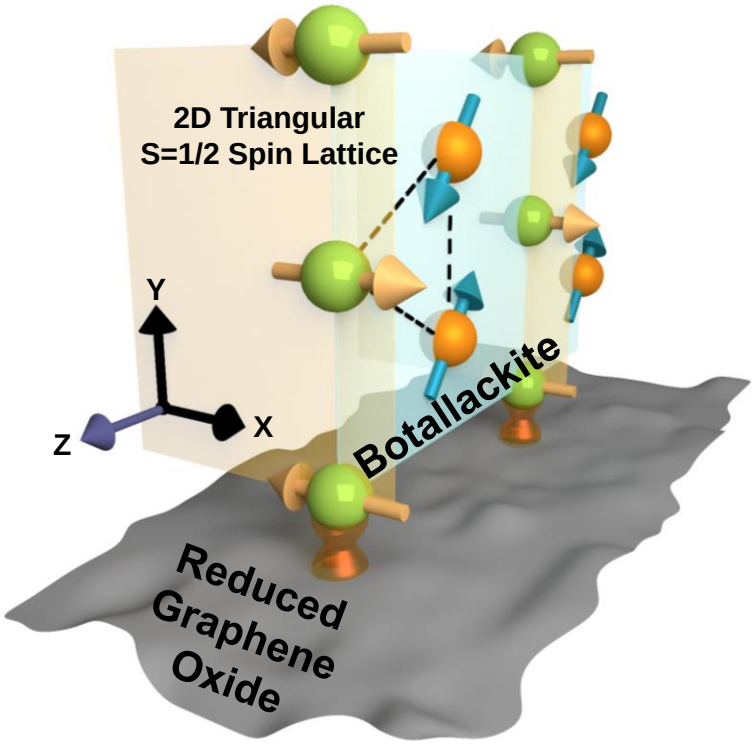

5.1 Introduction

Two-dimensional (2D) magnetic materials have received enormous interest in the scientific community, from both experimental and theoretical perspectives, as they offer unconventional magnetic ground states including emergence of quantum effects.[1-6] The primary origin lies in the restricted dimensionality of spin precession bringing magnetic fluctuations; thus in turn, leading to different non-classical phases, for example, Berezinskii−Kosterlitz−Thouless (BKT) transition.[7-8] Three dimensional (3D) spin precession results in Heisenberg system (generalized magnetic Hamiltonian $H = -\Sigma_{ij} J S_i.S_j$; where J is the nearest-neighbor exchange interaction for isotropic spins at i and j lattice sites). When restricted to an easy plane (2D) of magnetization, it results in an *XY* system ($J_x=J_y$, $J_z=0$); while the restriction in an easy axis (1D) leads to the Ising system ($J_x=J_y=0$). Amongst these order parameters, *XY* system requires single layer of the magnetically active lattice; however, in the presence of multilayers, inter-plane exchange interactions leads to 3D magnetic ordering and thus, experimental realization of *XY* spin anisotropy is challenging.[9-11] In some cases, externally applied magnetic field on spatially anisotropic 2D spin-lattice was observed to induce the easy plane anisotropy leading to crossover from Heisenberg antiferromagnetic state to 2D *XY* behavior or Ising ground state depending on the direction of applied magnetic field.[12-14]

To realize the *XY* spin anisotropy experimentally, 2D materials are highly sought after where 3D magnetic ordering is negligible.[15-16] Structurally 3D materials can also behave like 2D magnetic systems if the 2D spin-lattices are separated by non-magnetic layers and thus reducing the possibility of 3D magnetic ordering.[17-19] One of the naturally occurring 2D magnetic materials is botallackite ($Cu_2(OH)_3Br$) belonging to atacamite family of minerals (Cu(II); S=1/2) with a rare occurrence in nature whereby it recrystallizes into paratacamite (a structurally perfect S=1/2 Kagome spin lattice).[17]

Botallackite (Bo) is a layered material possessing 2D corner sharing S=1/2 triangular spin-lattice with two distinct Cu(II) octahedral coordination sites, Cu1 and Cu2 (Figure 5.1).[20-21] Cu1 and Cu2 sites differ in terms of ligands surrounding them, four hydroxide ions with two bromide ions for Cu1, while five hydroxide ions with one bromide ion for Cu2; and the layers are well-separated giving rise to quasi-2D magnetic properties of Bo.[22-24] Herein, we chemically anchored Bo lattice onto functionalized graphene – reduced graphene oxide (rGO) via unconventional oxidation-reduction chemistry. Remarkably, in the Bo-rGO

nanocomposite, an additional transition at ~5 K was observed after crossing the Néel temperature ($T_N \approx 8.9$ K), possibly due to the emergence of *XY* spin anisotropy.

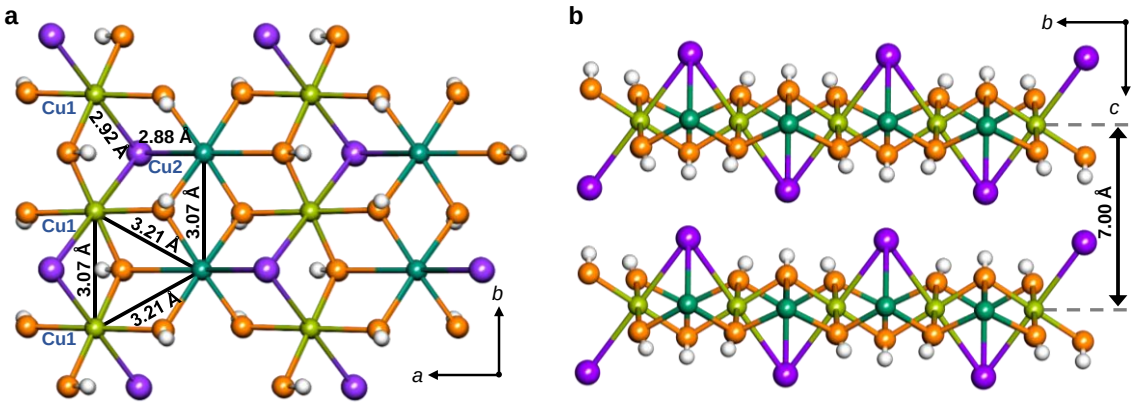

Figure 5.1. *Crystal structure of Bo along (a) c- and (b) a- crystallographic axes (color code: green/cyan – copper, orange – oxygen, purple – bromide, white – hydrogen).*

5.2 Materials and Methods

Graphite flake (+100 mesh), potassium permanganate ($KMnO_4$), hydrogen peroxide (H_2O_2), and copper bromide (CuBr) were used as received from Sigma-Aldrich. Sulfuric acid (H_2SO_4) and methanol (MeOH) were purchased from RANKEM (India). Millipore water (MQ, ~18.2 MΩ·cm) was used wherever required. Graphene Oxide (GO) was synthesized and duly characterized following our previous report.[25] Further, GO was centrifuged at 1000 rpm to remove the multilayers, if any. In a flask, ~640 mg (~4.46 mmol) CuBr was dispersed in 100 mL MQ H_2O followed by addition of 100 mL aqueous solution of GO (~1 mg/mL) and the reaction mixture was then allowed to stir at ~94 °C for ~24 h. The precipitate thus formed (dark green in color, **Bo-rGO** nanocomposite) was filtered and washed with MQ H_2O and MeOH followed by vacuum drying before further characterization and analysis. **Pristine Bo** was synthesized by stirring the aqueous dispersion of CuBr (~860 mg, ~6.0 mmol) in 200 mL MQ H_2O) at ~94 °C for ~24 h. Green colored precipitate was then filtered and washed with MQ H_2O and MeOH followed by vacuum drying before further experiments.

Magnetic response of Bo and Bo-rGO was recorded on SQUID vibrating sample magnetometer (Quantum Design). Magnetization in field-cooled (FC) mode was recorded by cooling the sample in the mentioned applied magnetic field and recording magnetization in the same field while warming. Zero-field-cooled (ZFC) magnetization was recorded after cooling the sample

in zero field and recording the magnetization in the mentioned magnetic field while warming. The ac magnetic susceptibility measurements were carried out in a CRYOGENIC make Vibrating Sample Magnetometer (VSM) under zero field condition (ZFC). The measurement was carried out in warming cycle. Raman spectroscopy was done on powder samples using a 632.8 nm laser on Horiba Jobin Yvon Raman microscope with 50X objective lens. Heat capacity was recorded in a Quantum Design-PPMS-Evercool II instrument. PXRD patterns were recorded on Bruker D8 Advance diffractometer with Cu Kα radiation (λ = 1.5406 Å); 2θ range of 10−50°. The simulated PXRD pattern for pristine Bo was generated by using Powder Cell for Windows (PCW) software version 2.4,[26] using the space group, lattice parameters, and atomic positions from the literature.[21] FESEM images were taken under a Zeiss Ultra Plus scanning electron microscope by drop casting the dispersion of samples in MeOH on Si wafer. TEM images were recorded on a drop casted sample (dispersed in methanol) over a 200 mesh Cu grid using a JEM-2200FS transmission electron microscope.

5.3 Results and Discussion

Chemical anchoring of Bo crystallites onto rGO sheets was achieved via interaction between oxy/carboxy functional groups of rGO and Cu(II) ions from the solution, which served as the nucleation sites (see materials and methods for details). Pristine Bo was synthesized as a control sample under similar reaction conditions in absence of GO (graphene oxide) as the precursor. Crystallinity of the Bo-rGO nanocomposite was probed by powder X-ray diffraction (PXRD) technique where all the peaks corresponding to Bo lattice (from the simulated pattern) were observed for both pristine Bo and Bo-rGO (no impurity peaks of Cu oxides).[21] However, the intensity ratio of peaks corresponding to 001 and 121 planes is significantly higher in Bo-rGO (I_{001}/I_{121}) compared to pristine Bo, indicating preferred orientation of growth in Bo-rGO along 001 direction (*ab* plane)[24] (Figures 5.2a and 5.1a). Both pristine Bo and Bo-rGO nanocomposite are thermally stable up to ~500 K (Appendix 5.1). In the nanocomposite, Bo crystallites were extensively wrapped with rGO sheets as visualized from field-emission scanning electron microscopic (FESEM) and transmission electron microscopic (TEM) images (Figure 5.2b, c and appendix 5.2). Further, the high-resolution TEM images of Bo-rGO nanocomposite exhibited fringes spaced at ~5.7 Å corresponding to 100 plane of Bo (Appendix 5.2d). Selected area electron diffraction (SAED) pattern recorded on the Bo-rGO

nanocomposite revealed monoclinic lattice originating from the Bo crystallites in line with the crystal structure of Bo (Appendix 5.2d).[21]

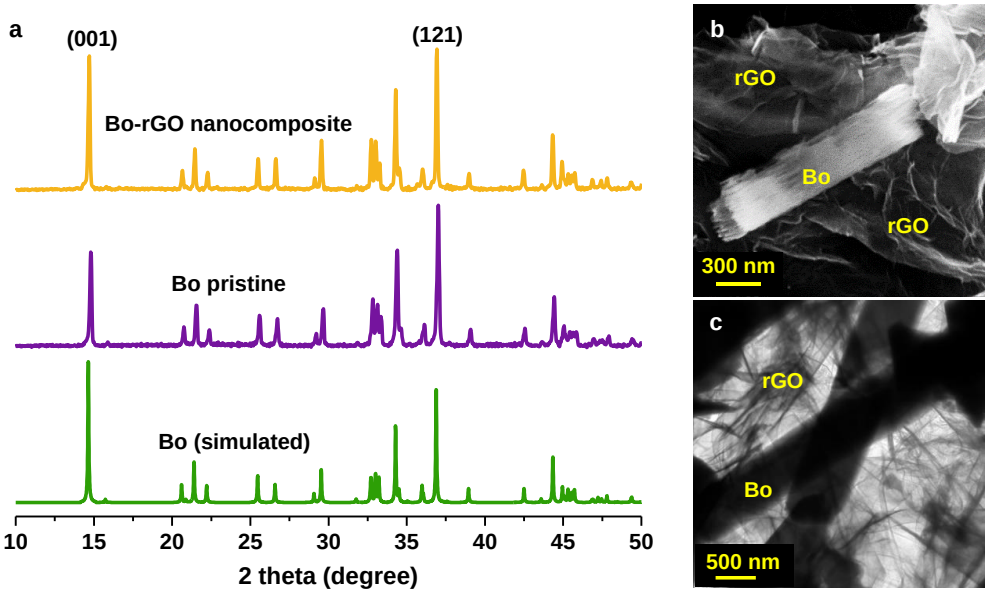

Figure 5.2. *(a) PXRD patterns of Bo-rGO nanocomposite, pristine Bo and simulated Bo. (b-c) FESEM and HRTEM images of Bo-rGO nanocomposite, respectively.*

To investigate the phase-purity of Bo (absence of any polymorph), Fourier-transformed infrared (FTIR) and Raman spectra were recorded. FTIR spectra of the Bo-rGO nanocomposite showed fingerprint peaks of Bo at ~3508 cm^{-1} (O-H stretching), ~532 cm^{-1}, ~511 cm^{-1} and ~422 cm^{-1} (O-Cu-O stretching) along with the characteristic peaks in the region from 850 to 680 cm^{-1} with peaks characteristic of rGO as well (Appendix 5.3a).[27-28] Raman spectra of the Bo-rGO nanocomposite exhibited the fingerprint peaks for Bo at ~101 cm^{-1} (Br-Cu-Br stretching), ~110 cm^{-1} and ~172 cm^{-1} (O-Cu bending and stretching), accompanied by various modes in the range from 247 to 319 cm^{-1} (O-Cu-O bending), 394 to 500 cm^{-1} (O-Cu-O stretching), and from 780 to 880 cm^{-1} for Cu-O-H bending (no impurity peaks) (Appendix 5.3b).[28] Further, the Raman spectrum exhibited characteristic D and G bands of rGO at ~1328 cm^{-1} and ~1586 cm^{-1}, respectively (Appendix 5.3c).[25, 29]

The dc magnetic susceptibility values as a function of temperature were recorded, in field-cooled (FC) and zero field-cooled modes (ZFC), for both pristine Bo and Bo-rGO nanocomposite. A maximum in the susceptibility for pristine Bo was observed at 10 K followed by a decrease in the susceptibility down to 5 K in both FC and ZFC plots, indicative of antiferromagnetic ordering with $T_N \approx 9.3$ K estimated from the maxima in $d\chi/dT$ plot (Figure

5.3a and appendix 5.4).[22-23] A similar maximum in magnetization was observed for Bo-rGO nanocomposite at 10 K at various applied magnetic fields affirming antiferromagnetic ordering with $T_N \approx 8.9$ K (Figure 5.3a and appendix 5.4). T_N for botallackite in literature varies in the range of 8 – 10 K based on dc susceptibility (9 K),[22] heat capacity (9.3 K)[24] and μSR (10 K)[22] measurements. Inverse magnetic susceptibility in the temperature range of 200 K – 300 K was fitted with Curie-Weiss equation, $\chi=C/(T-\theta_{CW})$. For Bo-rGO nanocomposite, the Curie constant (C) was found to be ~0.90 emu·Oe^{-1}·mol^{-1}·K and Weiss temp (θ) was estimated to be -13.1 K, indicating an overall weak antiferromagnetic interaction amongst spins with an effective magnetic moment of ~1.34 μ_B per Cu(II) ion, while for pristine Bo, the values are ~0.96 emu·Oe^{-1}·mol^{-1}·K, -13.1 K and ~1.38 μ_B, respectively (Appendix 5.5). Also, spin frustration in triangular lattice of Bo was almost unaltered in Bo-rGO nanocomposite with an *f* (= $|\theta_{CW}|/T_{Cr}$) value of ~1.3 for both.[17, 30]

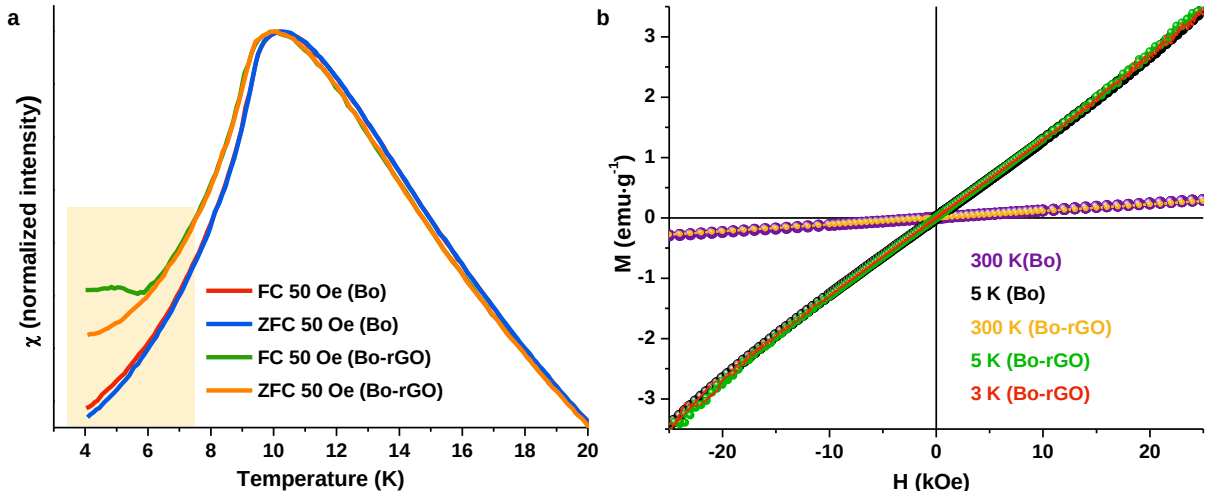

Figure 5.3. *(a) dc magnetic susceptibility plots in FC and ZFC modes at 50 Oe, (b) M-H plots at 300 K, 5 K, and 3 K of Bo and Bo-rGO nanocomposite (note: M-H plots were normalized only by the weight of magnetically active Bo).*

Insights into the crystal structure of Bo, revealed Cu–O–Cu angle of 102.7° and 101.8° in Cu1 and Cu2 chains, respectively, suggesting ferromagnetic superexchange interaction within the single chains, as reported.[31-32] Further, Cu1 and Cu2 chains bridged via hydroxide ions at two different Cu–O–Cu angles of 107.1° and 94.7° also suggested ferromagnetic superexchange interactions (Appendix 5.6).[31-32] Apart from hydroxide bridge, bromide bridge is also present in Cu1 chains, however, the Cu–Br–Cu angle is 63.2° and thus direct Cu–Cu exchange would dominate to give antiferromagnetic ordering (Figure 5.1 and appendix 5.6).[31-32] Such contradiction to classical Goodenough-Kanamori-Anderson (GKA) rules[31] favoring

ferromagnetic ordering is rather common in the domain of triangular spin-lattices, specifically in the atacamite family members, whereby antiferromagnetic ordering consistently prevailed.[22-23] Interestingly, magnetization for the Bo-rGO nanocomposite reproducibly exhibited a small cusp at 5 K, at 50 Oe and 100 Oe, followed by an up-rise and subsequent gradual saturation below 5 K which was negligible in pristine Bo (a small offset in FC and ZFC plots for Bo) (Figure 5.3a and appendix 5.4).

The cusp at 5 K is a clear signature of the onset of *XY* spin anisotropy in the magnetic response of Bo-rGO nanocomposite, where spins align in the easy plane of magnetization, thereby resulting in decrease in the overall magnetization.[12-13] Magnetization was then recorded as a function of externally applied magnetic field. At 300 K, both pristine Bo and Bo-rGO nanocomposite revealed M-H curves characteristic of a paramagnet. At 5 K, magnetization significantly enhanced; however, no hysteresis loop in the M-H curves was observed (Figure 5.3b and appendix 5.7).

Additionally, we have recorded ac susceptibility for the Bo-rGO system and a sharp downfall in χ'_{ac} (real part of ac susceptibility) was observed below ~8 K complimenting the dc susceptibility measurements whereby the magnetization decreases below ~8.9 K and thereby affirming antiferromagnetic ordering (Figure 5.4). The peak in χ'_{ac} was observed to be frequency independent and thus, ruling out the possibility of a spin-glass behaviour in the Bo-rGO system. Further below ~8 K, χ'_{ac} showed a slight uprise in the magnetization till 5 K, while M-H plots at 5 K and 3 K consistently exhibited no coercive fields, altogether reinforcing the emergence of *XY* spin anisotropy rather than ferromagnetic correlation and/or spin canting phenomena (Figure 5.3b and appendix 5.7).[33]

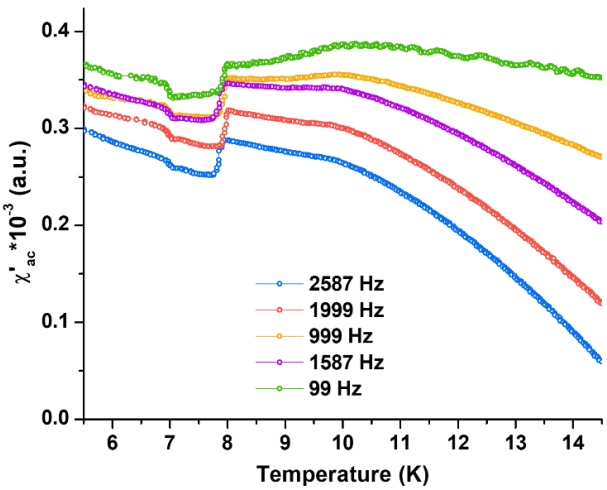

Figure 5.4. *Real part of ac susceptibility (χ'_{ac}) recorded for Bo-rGO at different frequencies.*

Further, heat capacity was recorded for Bo-rGO at various applied magnetic fields (Figure 5.5a): interestingly, a field independent hump at ~25 K^2 in C/T versus T^2 plot was observed (Figure 5.5b), supporting the dc and ac magnetic susceptibilities.[24] In Bo-rGO, Bo lattice is anchored onto rGO sheets which brings the orientated growth (or structural anisotropy along 001 direction) in the sample as reflected in (i) PXRD patterns (intensity of peak corresponding to 001 plane at ~14.8° is higher in Bo-rGO than pristine Bo, with respect to the most intense peak at ~37°); (ii) Raman spectra (peaks corresponding to O-Cu-O modes are affected significantly, as indicated by the altered intensity ratio in Bo-rGO and pristine Bo); and (iii) FESEM images (stacking of crystallites along *c* axis in Bo-rGO is much greater than that compared to pristine Bo) (Figure 5.2a, 5.6b, 5.2b and appendix 5.8). It is this oriented growth of Bo onto rGO sheets which can be assigned to the anisotropic magnetic response compared to polycrystalline Bo. For the measurements on single crystal Bo, $\chi_{\perp a}$ and $\chi_{\perp c}$ components were found to decrease sharply below ~9 K, whereas a gradual increase in $\chi_{\perp b}$ component was noted.[24] The Bo-rGO nanocomposite presented in our manuscript has preferred orientation along the 001 direction, that is, *ab* crystallographic plane of Bo; therefore, we are measuring the response predominantly corresponding to $\chi_{\parallel a}$ and $\chi_{\parallel b}$ in the dc magnetization measurement, and thus, a small minimum in χ_{dc} is observed.

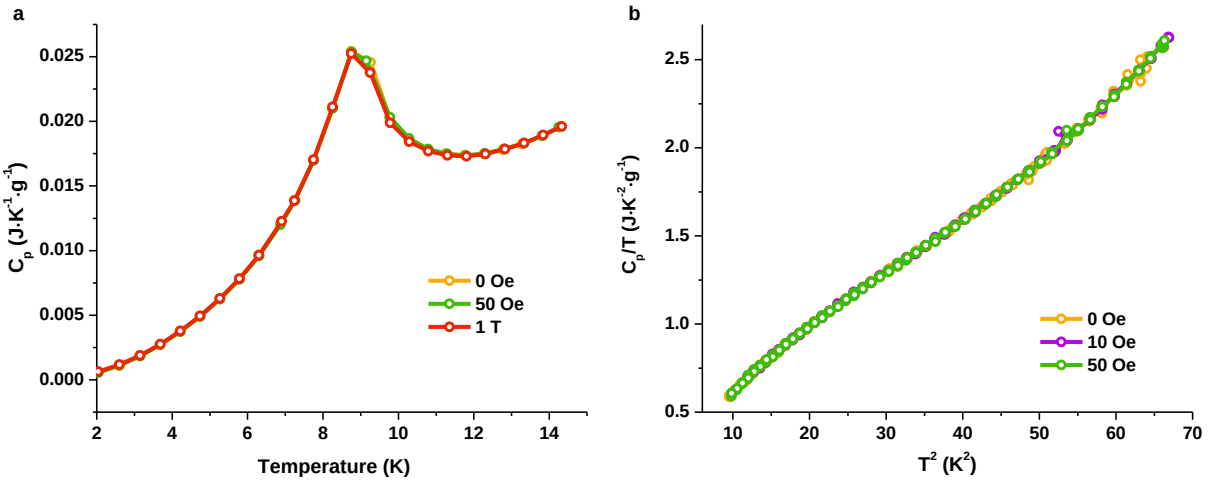

Figure 5.5. *Heat capacity recorded for Bo-rGO at varied externally applied magnetic fields, (a) C_p vs T and (b) C_p/T vs T^2 to visualize both the transitions.*

In Bo, both Cu1 and Cu2 sites are significantly distorted resulting in typical z-out Jahn-Teller (J-T) distortion.[34] Consequently, half-filled e_g level loses the degeneracy to gain overall stability and as a result, t_{2g} and e_g orbital levels further splits into four sets at different energy

levels (Figure 5.6a). The unpaired electron, both at Cu1 and Cu2 sites will preferentially occupy the $d_{x^2-y^2}$ orbital. Of the three spins on a triangle, two are antiparallel and the third one is noncollinearly aligned with respect to the antiparallel spins (Figure 5.6a).[35] In addition to spin ordering, highly aligned $d_{x^2-y^2}$ orbitals along the Cu2 sites (those at the Cu1 sites are inclined at an angle 45° and do not share the same plane) could bring orbital ordering.[34, 36-39] Such an anisotropic orbital arrangement within 2D spin-lattice indicates the presence of high anisotropy for the Cu2 chains compared to Cu1 chains thus rendering the material an antiferromagnet even after experiencing spin flop (Appendix 5.7). Similar magnetic response was observed earlier for pristine Bo and attributed to spin flop transition; however, Cu(II) sites experiencing spin flop were not assigned.[24] On the basis of the J-T effect, we can unequivocally assign Cu1 sites to undergo spin flop, while Cu2 sites will remain antiferromagnetically coupled.

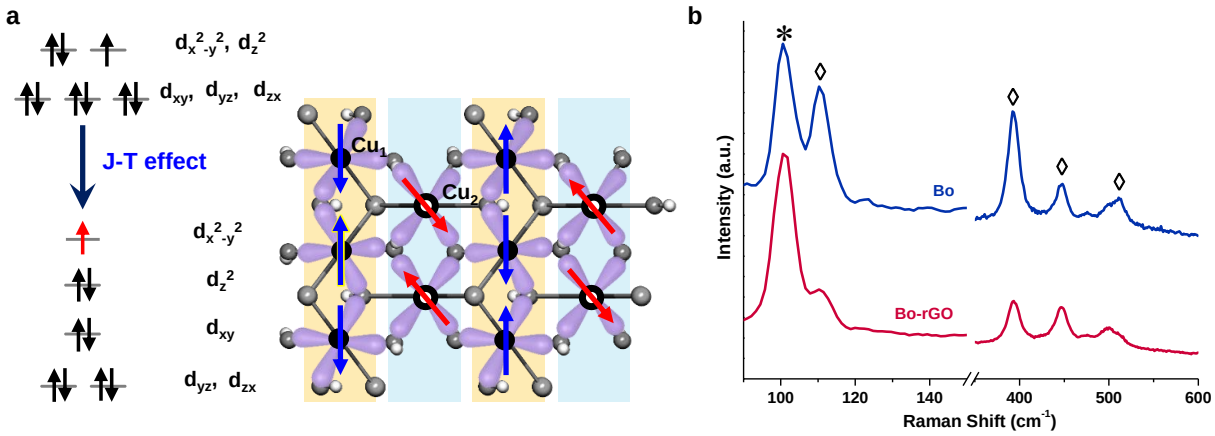

Figure 5.6. *(a) J-T effect and proposed orbital ordering in Bo. (b) Raman spectra of Bo and Bo-rGO nanocomposite. (*) Br-Cu-Br modes; (◇) O-Cu-O modes.*

In the case of Bo-rGO nanocomposite, chemical anchoring induced the *XY* anisotropy, where rGO is suggested to bind with Bo via Cu2 site. Once the nucleation starts on rGO sheets, it is spatially difficult for Bo to grow with *ab*-plane parallel to rGO sheets due to extended bromide ions hindering the functional groups from rGO to take the position of hydroxide ion in Bo. However, growing with *ab*-plane perpendicular to rGO sheets will be spatially favored where functional groups from rGO can approach to the required distance, replacing the axial hydroxide in the Cu2 site, in order to stabilize Bo crystallites, as can be visualized in the FESEM image, where predominant presence of stacked *ab* planes was observed for Bo-rGO system contrary to pristine Bo (Figure 5.2b and appendix 5.8). Also, the oxy/carboxy functional groups from rGO were found to be ligating to Cu(II) ions in the monodentate fashion from the FTIR spectra ($\Delta\nu \approx 260$ cm^{-1}, where values >200 cm^{-1} indicate monodentate binding mode)[40-

[41] and thus, does not perturb the crystal structure of Bo. Furthermore, in the Raman spectra, peaks corresponding to O–Cu–O modes (bending and stretching) are significantly modulated in terms of their intensity ratio in Bo-rGO nanocomposite compared to pristine Bo, while the Br–Cu–Br modes are almost intact (Figure 5.6b). Thus, chemical anchoring of Bo onto rGO sheets induced the preferred orientation and, in turn, possible *XY* anisotropy. The dc electrical conductivity value of the nanocomposite was found to be ~30 $S \cdot m^{-1}$ at 300 K and increased upon increasing temperature, thereby defining the Bo-rGO system as a magnetic semiconductor (Appendix 5.9).[30]

5.4 Conclusions

In summary, we have chemically embedded phase-pure botallackite $Cu_2(OH)_3Br$, a rare mineral from atacamite family having quasi-2D triangular anisotropic S=1/2 spin-lattice, onto reduced graphene oxide sheets. The unusual interface of 2D magnetic and 2D electronic lattices lead to the inference of *XY* anisotropy in the Bo-rGO nanocomposite based on complimentary ac and dc magnetic susceptibilities as well as heat capacity measurements. Though we have suggestive evidence for *XY* spin anisotropy, further detailed study is vital for a strong claim stating the induction of *XY* spin anisotropy. Further, inherent J-T effect in Bo enabled us to assign preferential spin flop at one of the two Cu(II) sites. Such an observation offers insight into the origin of *XY* behavior in anisotropic 2D spin-lattice, and our unique redox chemistry paves the way to modulate the existing magnetic anisotropy in other 2D magnetic materials by rGO.

5.5 Appendix

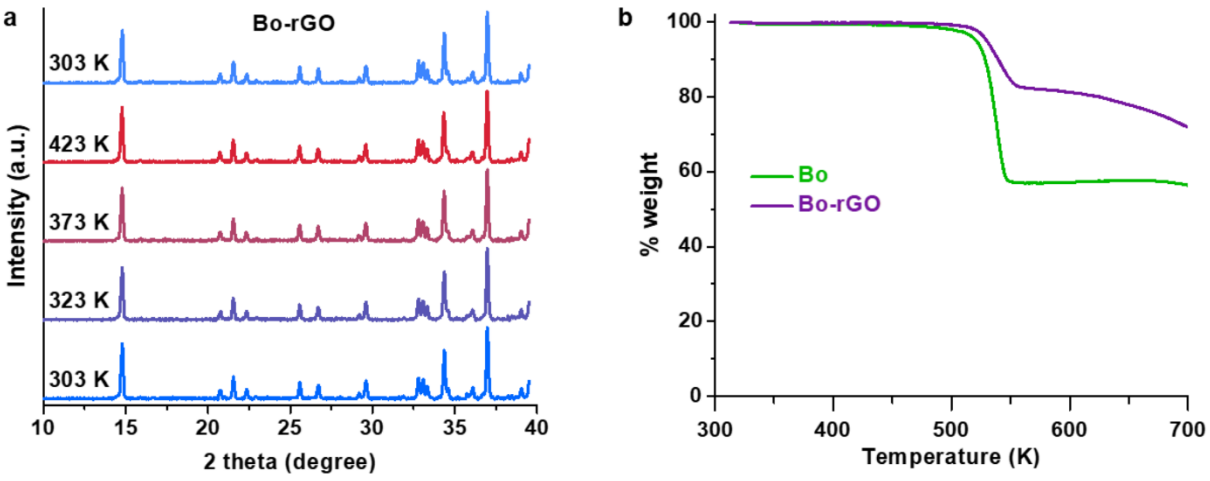

Appendix 5.1. *(a) Variable temperature PXRD patterns of Bo-rGO nanocomposite. (b) TGA profiles of pristine Bo and Bo-rGO nanocomposite.*

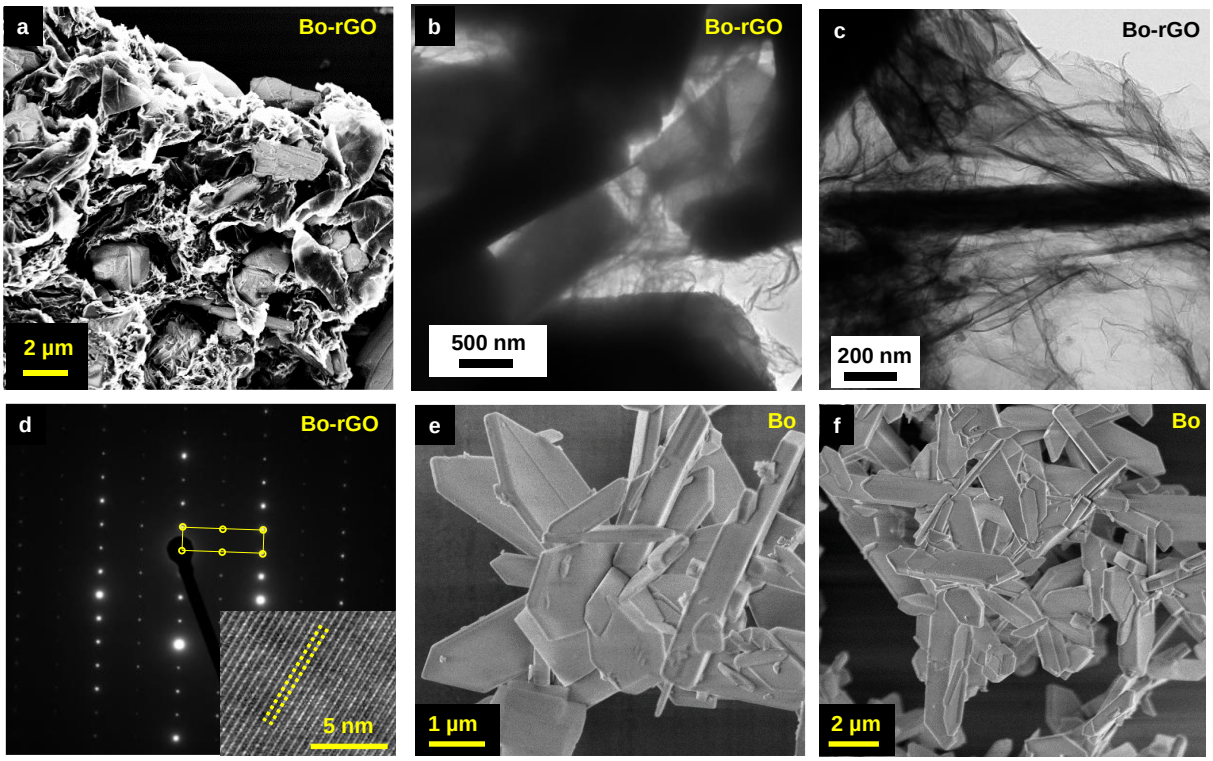

Appendix 5.2. *(a) FESEM image, (b,c) HRTEM image, (d) SAED pattern (inset: fringes) of Bo-rGO nanocomposite. (e,f) FESEM images of pristine Bo.*

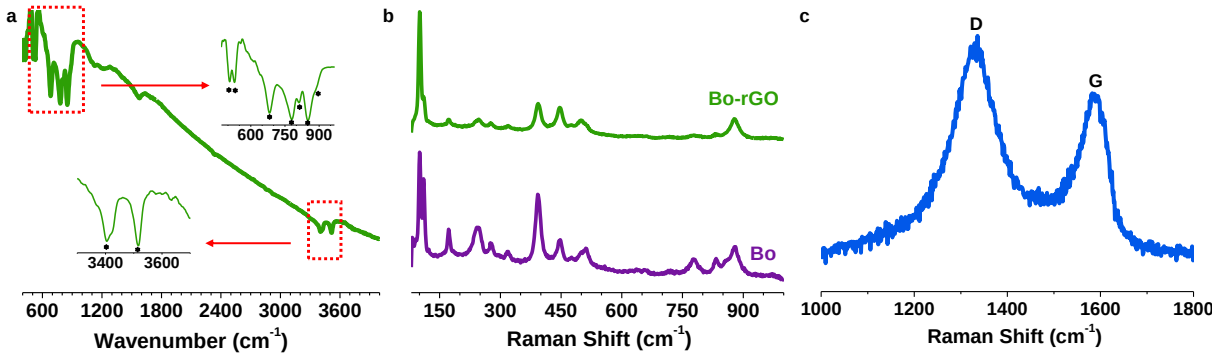

Appendix 5.3. *(a) FTIR spectrum of Bo-rGO nanocomposite (inset: zoomed-in view of specified spectral ranges), peaks corresponding to Bo are marked with asterisk. (b) Raman spectra of Bo-rGO nanocomposite and pristine Bo. (c) Raman spectrum of Bo-rGO nanocomposite possessing D (~1328 cm^{-1}) and G (~1586 cm^{-1}) bands corresponding to rGO sheets.*

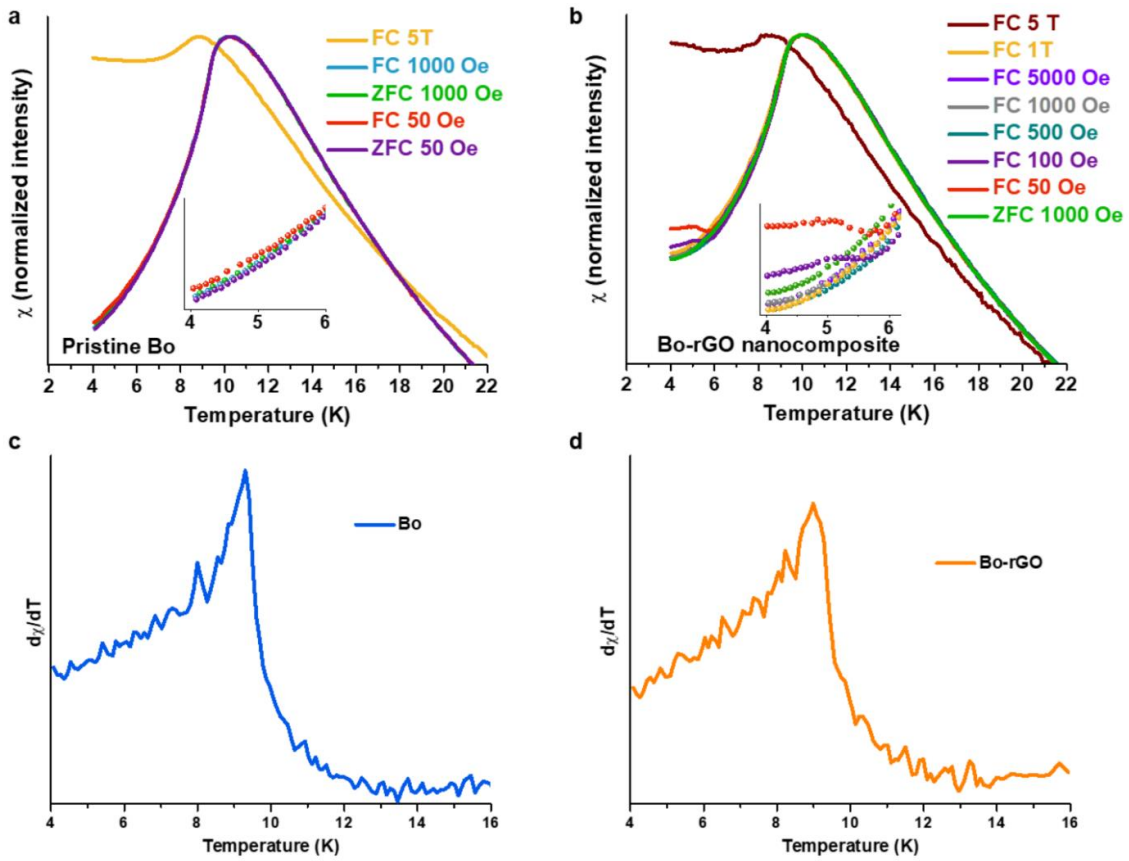

Appendix 5.4. *(a-b) Field dependent dc magnetic susceptibility (insets: zoomed-in view), (c-d) first derivative of dc magnetic susceptibility of pristine Bo and Bo-rGO nanocomposite.*

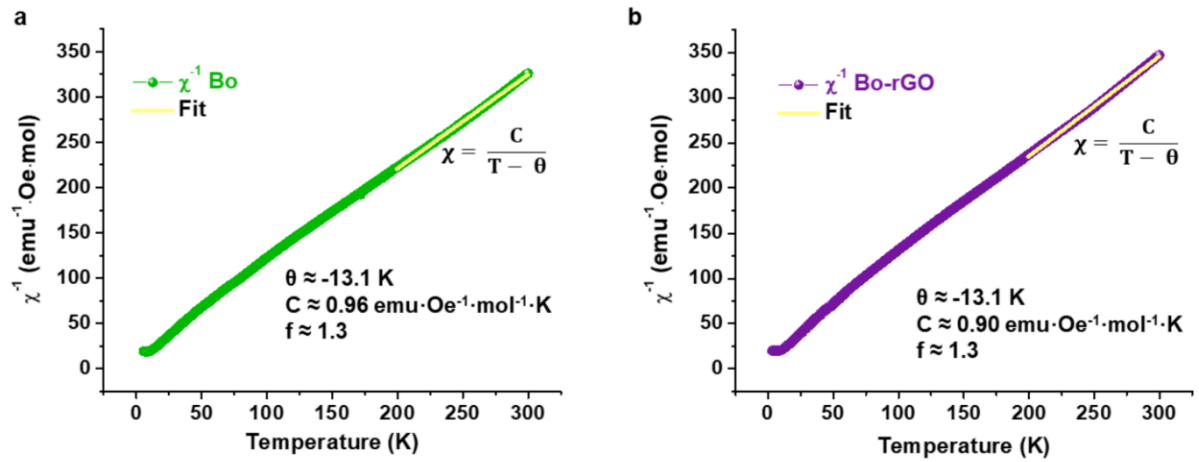

Appendix 5.5. *Inverse magnetic susceptibility (ZFC at 5 T normalized with respect to molar quantity of Bo) versus temperature fitted with Curie-Weiss equation from 200 K to 300 K (inset: Curie-Weiss equation and extracted parameters) for (a) pristine Bo and (b) Bo-rGO nanocomposite.*

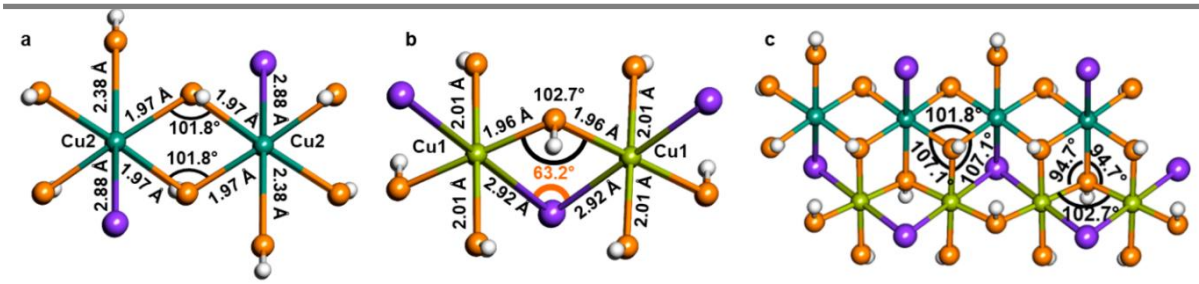

Appendix 5.6. *(a-c) Structural schemes of pristine Bo depicting bond lengths and bond angles at Cu1 and Cu2 sites.*

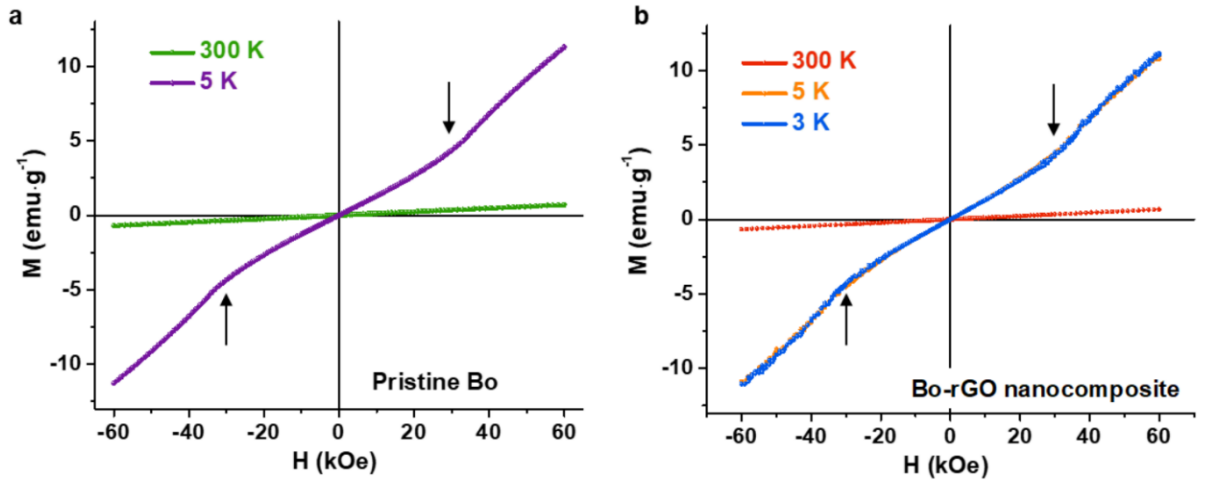

Appendix 5.7. *M-H plots at variable temperature for (a) pristine Bo and (b) Bo-rGO nanocomposite. Critical field (H_{Cr}) of ~30 kOe is indicated by black arrows.*[22-24]

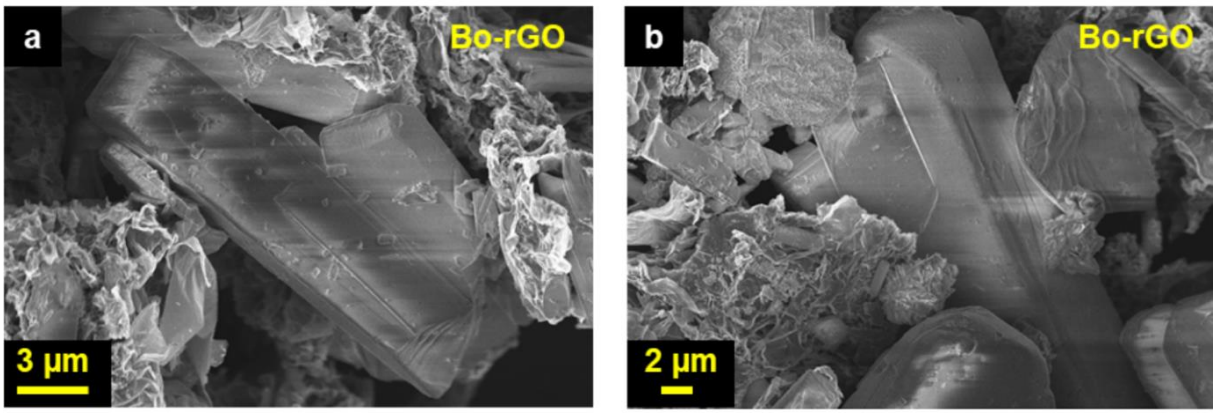

Appendix 5.8. *FESEM images of Bo-rGO depicting higher stacking along c-axis.*

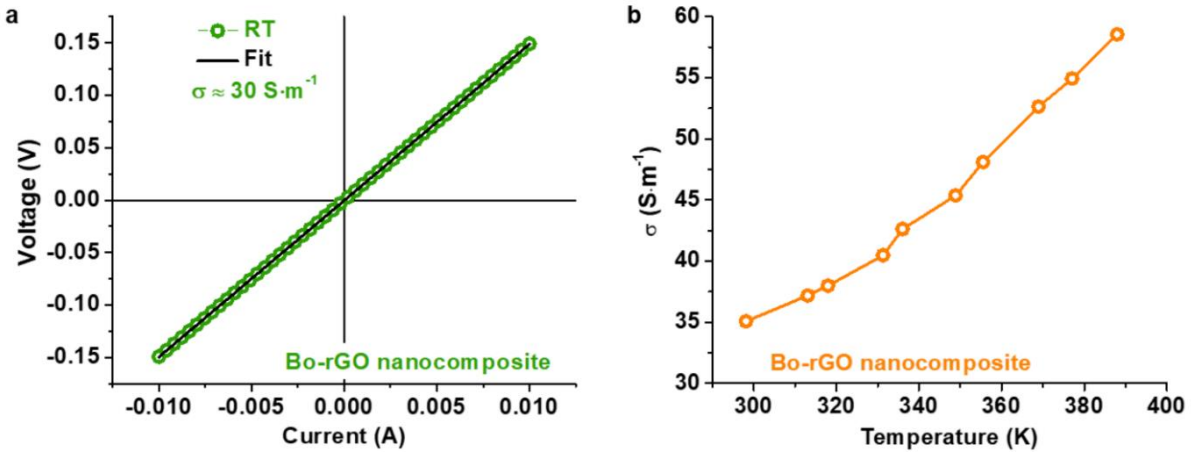

Appendix 5.9. *(a) Current-voltage (I-V) characteristic at 300 K and, (b) dc electrical conductivity as a function of temperature for Bo-rGO nanocomposite.*

5.6 References

(1) Burch, K. S.; Mandrus, D.; Park, J. G., Magnetism in two-dimensional van der Waals materials. *Nature* **2018**, *563*, 47.

(2) Cuccoli, A.; Roscilde, T.; Vaia, R.; Verrucchi, P., Detection of XY Behavior in Weakly Anisotropic Quantum Antiferromagnets on the Square Lattice. *Phys. Rev. Lett.* **2003**, *90*, 167205.

(3) Gibertini, M.; Koperski, M.; Morpurgo, A. F.; Novoselov, K. S., Magnetic 2D materials and heterostructures. *Nat. Nanotechnol.* **2019**, *14*, 408.

(4) Huang, B.; Clark, G.; Navarro-Moratalla, E.; Klein, D. R.; Cheng, R.; Seyler, K. L.; Zhong, D.; Schmidgall, E.; McGuire, M. A.; Cobden, D. H., Layer-dependent ferromagnetism in a van der Waals crystal down to the monolayer limit. *Nature* **2017**, *546*, 270.

(5) Gong, C.; Li, L.; Li, Z.; Ji, H.; Stern, A.; Xia, Y.; Cao, T.; Bao, W.; Wang, C.; Wang, Y.; Qiu, Z. Q.; Cava, R. J.; Louie, S. G.; Xia, J.; Zhang, X., Discovery of intrinsic ferromagnetism in two-dimensional van der Waals crystals. *Nature* **2017**, *546*, 265.

(6) Gong, C.; Zhang, X., Two-dimensional magnetic crystals and emergent heterostructure devices. *Science* **2019**, *363*, eaav4450.

(7) Berezinsky, V., Destruction of long range order in one-dimensional and two-dimensional systems having a continuous symmetry group. I. Classical systems. *Zh. Eksp. Teor. Fiz.* **1970**, *32*, 493.

(8) Kosterlitz, J. M.; Thouless, D. J., Ordering, metastability and phase transitions in two-dimensional systems. *J. Phys. C* **1973**, *6*, 1181.

(9) Joy, P. A.; Vasudevan, S., Magnetism in the layered transition-metal thiophosphates MPS_3 (M=Mn, Fe, and Ni). *Phys. Rev. B* **1992**, *46*, 5425.

(10) Yasuda, C.; Todo, S.; Hukushima, K.; Alet, F.; Keller, M.; Troyer, M.; Takayama, H., Neel Temperature of Quasi-Low-Dimensional Heisenberg Antiferromagnets. *Phys. Rev. Lett.* **2005**, *94*, 217201.

(11) Kim, K.; Lim, S. Y.; Lee, J.-U.; Lee, S.; Kim, T. Y.; Park, K.; Jeon, G. S.; Park, C. H.; Park, J.-G.; Cheong, H., Suppression of magnetic ordering in XXZ-type antiferromagnetic monolayer $NiPS_3$. *Nat. Commun.* **2019**, *10*, 345.

(12) Kohama, Y.; Jaime, M.; Ayala-Valenzuela, O. E.; McDonald, R. D.; Mun, E. D.; Corbey, J. F.; Manson, J. L., Field-induced XY and Ising ground states in a quasi-two-dimensional S=1/2 Heisenberg antiferromagnet. *Phys. Rev. B* **2011**, *84*, 184402.

(13) Cuccoli, A.; Roscilde, T.; Vaia, R.; Verrucchi, P., Field-induced XY behavior in the S=1/2 antiferromagnet on the square lattice. *Phys. Rev. B* **2003**, *68*, 060402.

(14) Landau, D. P.; Binder, K., Phase diagrams and critical behavior of a two-dimensional anisotropic Heisenberg antiferromagnet. *Phys. Rev. B* **1981**, *24*, 1391.

(15) Ito, S.; Kurita, N.; Tanaka, H.; Ohira-Kawamura, S.; Nakajima, K.; Itoh, S.; Kuwahara, K.; Kakurai, K., Structure of the magnetic excitations in the spin-1/2 triangular-lattice Heisenberg antiferromagnet $Ba_3CoSb_2O_9$. *Nat. Commun.* **2017**, *8*, 235.

(16) Nakayama, G.; Hara, S.; Sato, H.; Narumi, Y.; Nojiri, H., Synthesis and magnetic properties of a new series of triangular-lattice magnets, $Na_2BaMV_2O_8$ (M= Ni, Co, and Mn). *J. Phys.: Condens. Matter* **2013**, *25*, 116003.

(17) Shores, M. P.; Nytko, E. A.; Bartlett, B. M.; Nocera, D. G., A Structurally Perfect S = 1/2 Kagomé Antiferromagnet. *J. Am. Chem. Soc.* **2005**, *127*, 13462.

(18) Plumier, R.; Legrand, E., Structure magnétique de K_2NiF_4. *J. Phys. Radium* **1962**, *23*, 474.

(19) Mahata, P.; Natarajan, S.; Panissod, P.; Drillon, M., Quasi-2D XY Magnetic Properties and Slow Relaxation in a Body Centered Metal Organic Network of [Co_4] Clusters. *J. Am. Chem. Soc.* **2009**, *131*, 10140.

(20) Krivovichev, S. V.; Hawthorne, F. C.; Williams, P. A., Structural complexity and crystallization: the Ostwald sequence of phases in the $Cu_2(OH)_3Cl$ system (botallackite–atacamite–clinoatacamite). *Struct. Chem.* **2017**, *28*, 153.

(21) Aebi, F., Die Krystallstruktur des basischen Kupferbromids $CuBr_2$, $3Cu(OH)_2$. *Helv. Chim. Acta* **1948**, *31*, 369.

(22) Zheng, X. G.; Yamashita, T.; Hagihala, M.; Fujihala, M.; Kawae, T., Magnetic transitions in botallackite-structure $Cu_2(OH)_3Br$ and $Cu_2(OH)_3I$. *Physica B* **2009**, *404*, 680.

(23) Zheng, X. G.; Mori, T.; Nishiyama, K.; Higemoto, W.; Yamada, H.; Nishikubo, K.; Xu, C. N., Antiferromagnetic transitions in polymorphous minerals of the natural cuprates atacamite and botallackite Cu_2ClOH_3. *Phys. Rev. B* **2005**, *71*, 174404.

(24) Zhao, Z. Y.; Che, H. L.; Chen, R.; Wang, J. F.; Sun, X. F.; He, Z. Z., Magnetism study on a triangular lattice antiferromagnet $Cu_2(OH)_3Br$. *J. Phys.: Condens. Matter* **2019**, *31*, 275801.

(25) Jha, P. K.; Singh, S. K.; Kumar, V.; Rana, S.; Kurungot, S.; Ballav, N., High-Level Supercapacitive Performance of Chemically Reduced Graphene Oxide. *Chem* **2017**, *3*, 846.

(26) Kraus, W.; Nolze, G., POWDER CELL– a program for the representation and manipulation of crystal structures and calculation of the resulting X-ray powder patterns. *J. Appl. Cryst.* **1996,** *29*, 301.

(27) Pollard, A. M.; Thomas, R. G.; Williams, P. A., Synthesis and stabilities of the basic copper(II) chlorides atacamite, paratacamite and botallackite. *Mineral. Mag.* **1989**, *53*, 557.

(28) Liu, X.-D.; Hagihala, M.; Zheng, X.-G.; Guo, Q.-X., Vibrational spectroscopic properties of botallackite-structure basic copper halides. *Vib. Spectrosc.* **2011**, *56*, 177.

(29) Ferrari, A. C.; Robertson, J., Interpretation of Raman spectra of disordered and amorphous carbon. *Phys. Rev. B* **2000**, *61*, 14095.

(30) Gupta, K.; Jha, P. K.; Dadwal, A.; Debnath, A. K.; Jaiswal, I.; Rana, S.; Joy, P. A.; Ballav, N., Embedding S = 1/2 Kagome-like Lattice in Reduced Graphene Oxide. *J. Phys. Chem. Lett.* **2019**, *10*, 2663.

(31) Goodenough, J. B., *Magnetism and chemical bond*. Interscience Publ.: 1963; Vol. 1.

(32) Vernay, F.; Penc, K.; Fazekas, P.; Mila, F., Orbital degeneracy as a source of frustration in $LiNiO_2$. *Physical Review B* **2004**, *70*, 014428.

(33) Gupta, K.; Dadwal, A.; Rana, S.; Jha, P. K.; Jain, A.; Yusuf, S. M.; Joy, P. A.; Ballav, N., Metamagnetism in Nanosheets of Co^{II}-MOF with T_N at 26 K and a Giant Hysteretic Effect at 5 K. *Inorg. Chem.* **2018**, *57*, 15044.

(34) Pavarini, E.; Koch, E.; Lichtenstein, A. I., Mechanism for Orbital Ordering in $KCuF_3$. *Phys. Rev. Lett.* **2008**, *101*, 266405.

(35) Zheng, X.-G.; Yamauchi, I.; Kitajima, S.; Fujihala, M.; Maki, M.; Lee, S.; Hagihala, M.; Torii, S.; Kamiyama, T.; Kawae, T., Two-dimensional triangular-lattice Cu(OH)Cl, belloite, as a magnetodielectric system. *Phys. Rev. Mater.* **2018**, *2*, 104401.

(36) Tokura, Y.; Nagaosa, N., Orbital Physics in Transition-Metal Oxides. *Science* **2000**, *288*, 462.

(37) Reitsma, A. J.; Feiner, L. F.; Oleś, A. M., Orbital and spin physics in $LiNiO_2$ and $NaNiO_2$. *New J. Phys.* **2005**, *7*, 121.

(38) Yoshida, H.; Yamaura, J.-i.; Isobe, M.; Okamoto, Y.; Nilsen, G. J.; Hiroi, Z., Orbital switching in a frustrated magnet. *Nat. Commun.* **2012**, *3*, 860.

(39) de Brion, S.; Núñez-Regueiro, M. D.; Chouteau, G., Orbital and Spin Order in the Triangular S=1/2 Layered Compound $(Li,Na)NiO_2$. In *Frontiers in Magnetic Materials*, Narlikar, A. V., Ed. Springer Berlin Heidelberg: Berlin, Heidelberg, 2005; 247.

(40) Bronstein, L. M.; Huang, X.; Retrum, J.; Schmucker, A.; Pink, M.; Stein, B. D.; Dragnea, B., Influence of Iron Oleate Complex Structure on Iron Oxide Nanoparticle Formation. *Chem. Mater.* **2007**, *19*, 3624.

(41) Tanskanen, A.; Karppinen, M., Iron-Terephthalate Coordination Network Thin Films Through In-Situ Atomic/Molecular Layer Deposition. *Sci. Rep.* **2018**, *8*, 8976.

Embedding S = 1/2 Kagome-like Lattice in Reduced Graphene Oxide

Author: Kriti Gupta, Plawan Kumar Jha, Arun Dadwal, et al

Publication: Journal of Physical Chemistry Letters

Publisher: American Chemical Society

Date: Jun 1, 2019

PERMISSION/LICENSE IS GRANTED FOR YOUR ORDER AT NO CHARGE

This type of permission/license, instead of the standard Terms & Conditions, is sent to you because no fee is being charged for your order. Please note the following:

- Permission is granted for your request in both print and electronic formats, and translations.
- If figures and/or tables were requested, they may be adapted or used in part.
- Please print this page for your records and send a copy of it to your publisher/graduate school.
- Appropriate credit for the requested material should be given as follows: "Reprinted (adapted) with permission from (COMPLETE REFERENCE CITATION). Copyright (YEAR) American Chemical Society." Insert appropriate information in place of the capitalized words.
- One-time permission is granted only for the use specified in your request. No additional uses are granted (such as derivative works or other editions). For any other uses, please submit a new request.

BACK CLOSE WINDOW

Integrating Structurally Perfect S = 1/2 Kagome-Lattice with Reduced Graphene Oxide

Author: Kriti Gupta, Arun Dadwal, Pranay Ninawe, et al

Publication: The Journal of Physical Chemistry C

Publisher: American Chemical Society

Date: Sep 1, 2020

PERMISSION/LICENSE IS GRANTED FOR YOUR ORDER AT NO CHARGE

This type of permission/license, instead of the standard Terms & Conditions, is sent to you because no fee is being charged for your order. Please note the following:

- Permission is granted for your request in both print and electronic formats, and translations.
- If figures and/or tables were requested, they may be adapted or used in part.
- Please print this page for your records and send a copy of it to your publisher/graduate school.
- Appropriate credit for the requested material should be given as follows: "Reprinted (adapted) with permission from (COMPLETE REFERENCE CITATION). Copyright (YEAR) American Chemical Society." Insert appropriate information in place of the capitalized words.
- One-time permission is granted only for the use specified in your request. No additional uses are granted (such as derivative works or other editions). For any other uses, please submit a new request.

BACK CLOSE WINDOW

Exploring Magnetic XY Behavior in a Quasi-2D Anisotropic Triangular Lattice of Cu(II) by Functionalized Graphene

Author: Kriti Gupta, Arun Dadwal, Plawan Kumar Jha, et al
Publication: Inorganic Chemistry
Publisher: American Chemical Society
Date: May 1, 2020

PERMISSION/LICENSE IS GRANTED FOR YOUR ORDER AT NO CHARGE

This type of permission/license, instead of the standard Terms & Conditions, is sent to you because no fee is being charged for your order. Please note the following:

- Permission is granted for your request in both print and electronic formats, and translations.
- If figures and/or tables were requested, they may be adapted or used in part.
- Please print this page for your records and send a copy of it to your publisher/graduate school.
- Appropriate credit for the requested material should be given as follows: "Reprinted (adapted) with permission from (COMPLETE REFERENCE CITATION). Copyright (YEAR) American Chemical Society." Insert appropriate information in place of the capitalized words.
- One-time permission is granted only for the use specified in your request. No additional uses are granted (such as derivative works or other editions). For any other uses, please submit a new request.

BACK CLOSE WINDOW